Titre: Title:	Composite Aircraft Engine Fire Walls : a Small-Scale Experimental Testbed to study Thermomechanical Degradation under Fire
Auteur: Author:	Tanja Pelzmann
Date:	2022
Type:	Mémoire ou thèse / Dissertation or Thesis
Référence: Citation:	Pelzmann, T. (2022). Composite Aircraft Engine Fire Walls : a Small-Scale Experimental Testbed to study Thermomechanical Degradation under Fire [Thèse de doctorat, Polytechnique Montréal]. PolyPublie. https://publications.polymtl.ca/10345/

URL de PolyPublie: PolyPublie URL:	https://publications.polymtl.ca/10345/
Directeurs de recherche: Advisors:	Étienne Robert, & Martin Lévesque
Programme: Program:	PhD.

POLYTECHNIQUE MONTRÉAL
affiliée à l'Université de Montréal

Composite Aircraft Engine Firewalls: a small-scale experimental testbed to study thermomechanical degradation under fire

TANJA PELZMANN
Département de génie mécanique

Thèse présentée en vue de l'obtention du diplôme de *Philosophiæ Doctor*
Génie mécanique

Mai 2022

POLYTECHNIQUE MONTRÉAL
affiliée à l'Université de Montréal

Cette thèse intitulée :

Composite Aircraft Engine Firewalls: a small-scale experimental testbed to study thermomechanical degradation under fire

présentée par **Tanja PELZMANN**
en vue de l'obtention du diplôme de *Philosophiæ Doctor*
a été dûment acceptée par le jury d'examen constitué de :

Jérôme VÉTEL, président
Étienne ROBERT, membre et directeur de recherche
Martin LÉVESQUE, membre et codirecteur de recherche
Alexis COPPALLE, membre
Patrice SEERS, membre externe

DEDICATION

'*Why,' said the Dodo, 'the best way to explain it is to do it.'*

-Lewis Carroll, Alice in Wonderland

ACKNOWLEDGEMENTS

First and foremost, I would like to express my heartfelt thanks to my supervisors Étienne Robert and Martin Lévesque with whom I had the opportunity to work. Étienne, thank you for just the right amount of guidance and trust, to let me explore my own ideas and to remind me from time to time that "lagom är bäst" (*Just the right amount is best*). Martin, your comments helped me not only to improve my work, but more so the way I present it to others.

Most of the material in this thesis is the result of intensive experimental efforts translating to countless hours of designing, building, testing, failing and restarting all over again. None of this would have been possible and for sure not enjoyable, without the wonderful colleagues and friends I have made at the LEMUR laboratory, in particular Pablo Chávez-Gómez, Christian Boanta and Jean Langot. I would like to recognize the help and expertise provided by the technical staff and thank especially Bénédict Besner and Philippe Massé for their assistance. I am also sincerely grateful to Simon Hind from NRC, to Jason Hamp and Barry Barnett from Pratt & Whitney Canada Corp. and to Tom Mallon and Mary Dowey from Resonate Testing Inc. for their continued interest and for letting me benefit from their vast experience in the field of fire testing.

I thank my friends and family for their support and encouragement and would like to conclude with very special thanks to Martin Schwinzerl, Martin Luckabauer and Jacques Lengaigne for infinite patience, kindness and food in adversity. Five years is far too long.

RÉSUMÉ

Cette thèse traite du comportement de dégradation des matériaux composites époxy renforcés de fibres de carbone exposés à une flamme. Ces composants légers sont utilisés comme des revêtements acoustiques pare-feu ou des nacelles dans les moteurs d'avion turbofan. Ils forment les limites de ce qu'on appelle les zones de feu, à l'interface entre le flux d'air primaire ou secondaire et les sections accessoires. En cas d'incendie indésirable, ces composants doivent agir contre la combustion et empêcher la propagation des flammes, laissant ainsi à l'équipage suffisamment de temps pour détecter le problème et poser l'avion en toute sécurité. Dans le cadre du vaste processus de certification, ces composants doivent subir des essais de résistance au feu pour démontrer qu'ils peuvent résister à une attaque de flamme pendant une durée prescrite tout en conservant leurs propriétés mécaniques. Les normes de certification fournissent des lignes directrices claires pour la mise en place et la procédure des essais, mais les résultats obtenus à l'aide des installations conventionnelles manquent d'une information essentielle : ils ne fournissent pas une mesure des propriétés matérielles des composants testés et de leur évolution dans le temps, mais seulement un simple verdict de réussite/échec. Cette lacune des tests de certification actuels motive le développement d'installations d'essai à petite échelle, comme celle présentée ici, recréant les conditions prescrites dans les normes de certification, mais à un coût moindre et dans des environnements où la dégradation des matériaux peut être évaluée en détail. Les résultats recueillis lors de ces expériences sont destinés à soutenir le développement de modèles numériques et à guider les choix de nouveaux systèmes de matériaux adaptés aux applications aérospatiales à haute température.

Un état de l'art détaillé des essais de résistance au feu est d'abord présenté : normes applicables, conditions d'essai et équipement à grande échelle. Un essai de résistance au feu est défini par trois caractéristiques principales : le type de source de chaleur et son flux thermique nominal, l'orientation et la taille de l'éprouvette et les critères de défaillance évalués. Dans le cas des essais au feu, un spécimen monté verticalement est exposé à une flamme calibrée provenant d'un brûleur à mazout et différents critères de défaillance, tels que la combustion continue de l'échantillon ou la pénétration du feu, sont évalués. Bien que le montage d'essai à grande échelle soit commenté à plusieurs reprises dans la thèse, l'objectif principal est l'étude de l'interaction flamme-échantillon à échelle réduite. L'étude de cette interaction exige d'abord le développement d'une infrastructure scientifique capable de recréer des conditions similaires à celles de la certification dans un environnement bien contrôlé et ensuite la mise en œuvre d'outils de diagnostic appropriés pour évaluer les paramètres qui sont essentiels pour décrire la dégradation thermique des matériaux. La thèse contribue à ces deux sujets, par le développement d'une infrastructure et de méthodes ainsi que par une étude de cas sur la résistance au feu des composites en fibre de carbone.

Les méthodes expérimentales présentées comprennent la conception et la mise en œuvre d'une nouvelle installation à petite échelle. Point de vue novateur dans les essais au feu à l'échelle du banc, cette installation comprend un brûleur au kérosène qui peut atteindre les valeurs de flux thermique et de température de flamme exigées par les normes de certification, mais à une puissance de brûleur considérablement réduite. En outre, des torches à gaz largement utilisées dans les essais scientifiques ont été implementées pour recréer les expériences de pointe de la littérature. Tous les brûleurs ont été calibrés pour atteindre la densité du flux thermique et les températures de flamme spécifiées dans les normes de certification sur une gamme de conditions de fonctionnement, permettant l'étude de l'effet du type de combustible et du rapport d'équivalence de flamme. Les résultats obtenus sont comparés à travers différentes échelles de test pour assurer la cohérence.

La thèse se penche sur les méthodes expérimentales (thermographie infrarouge, jauges à couche mince et calorimétrie) et les défis associés pour mesurer la densité du flux thermique et la température de la flamme ou l'émissivité et les températures de l'échantillon. L'une des principales sources d'erreur lors de la mesure de la température de surface d'un matériau se dégradant rapidement à l'aide de la thermographie infrarouge conventionnelle est la variation de l'émissivité. Pour surmonter cette difficulté, nous proposons une technique basée sur la pyrométrie bicolore qui ne nécessite pas la connaissance a priori de l'émissivité de l'échantillon. La thèse fournit une introduction au sujet et discute en détail le modèle de transfert radiatif et la sélection du matériel nécessaire pour réduire les contributions d'erreur globale. Au lieu de mesurer le signal sur une large gamme spectrale, le rapport des signaux acquis à travers deux filtres passe-bande étroits est utilisé sous l'hypothèse principale que la scène est restée inchangée. Cela nécessite toutefois que la fréquence d'acquisition de la caméra et la sélection des filtres optiques soient adaptées à l'expérience. Nous proposons également une méthodologie de post-traitement et une série d'expériences de calibration. Une étude comparative avec différents composites et métaux montre que notre approche réduit significativement l'erreur de mesure.

Finalement, l'effet de la chimie de la flamme sur le comportement de dégradation des spécimens de fibre de carbone est étudié en les exposant à des flammes de kérosène et de gaz. Certains résultats ont confirmé la littérature déjà disponible, mais d'autres ont été mis en lumière par les recherches rapportées ici. Il est par exemple connu que les tests utilisant une flamme de gaz propane conduisent en général à une masse résiduelle ou une résistance à la traction résiduelle plus élevée après l'exposition au feu. Cependant, les torches à gaz sont un outil essentiel pour la communauté scientifique dans les expériences de combustion, et nous démontrons qu'une flamme de gaz peut être adaptée pour induire un dommage thermique similaire à celui d'une flamme de kérosène calibrée. La principale contribution de ce travail est donc son approche globale de la mise à l'échelle des essais au feu tout en fournissant une infrastructure scientifique pouvant être utilisée pour des études plus fondamentales de la combustion à l'avenir.

ABSTRACT

This thesis deals with the material degradation behaviour of carbon-fibre reinforced epoxy composite materials exposed to a flame. These lightweight components are considered as firewall acoustic liners or fan cases in turbofan aircraft engines. They form the boundaries of so-called fire zones, being the interface between primary or secondary air flow and accessory sections. In the case of an unwanted fire, the components shall act as a firewall and prevent flame propagation, thus providing the crew with enough time to detect the problem and safely land the aircraft. As part of the extensive certification process, these components must undergo fire resistance testing to demonstrate that they can withstand a flame attack for a prescribed time while maintaining their mechanical properties. Certification standards provide clear guidelines for the testing set-up and procedure, but the results obtained using conventional facilities lack a critical information: they do not provide a measure of the material properties of the components tested and their evolution over time, but rather only a simple pass/fail verdict. This shortcoming of the current certification tests motivates the development of small-scale testing facilities, such as the one presented here, recreating the conditions prescribed in the certification standards but at a lower cost and in settings where the material degradation can be assessed in detail. The results gathered in these experiments are intended to support numerical model development and guide choices for new material systems suitable for high temperature aerospace applications.

A detailed state-of-the art in fire resistance testing is first provided: applicable standards, test conditions and large-scale equipment. A fire test is defined by three main characteristics: the type of heat source and its nominal heat flux, the orientation and size of the specimen and the failure criteria assessed. In the case of firewall testing, a vertically mounted specimen is exposed to a calibrated flame from an oil burner and different failure criteria, as for instance continuous burning of the sample or fire penetration, are assessed. Although the large-scale test setup is commented in the thesis on several occasions, the main objective is on the study of the flame-sample interaction at reduced scale. The study of this interaction demands at first the development of scientific infrastructure capable of recreating certification-like conditions in a well-controlled environment and secondly the implementation of suitable diagnostic tools to assess parameters which are key to describe the material thermal degradation. The thesis contributes to both topics, by the development of infrastructure and methods as well as through a case study on the fire resistance of carbon fibre composites.

The experimental methods presented includes the design and implementation of a novel small-scale facility that allows to test specimen at the coupon level. A novel point of view in bench-scale

fire testing, this setup features a kerosene burner that can achieve the desired heat flux and flame temperature values demanded by the certification standards, but at significantly reduced burner power. In addition, gas torches used extensively in scientific bench-scale testing have implemented as a reference and to recreate state-of-the art experiments from literature. All burners have been calibrated to achieve the heat flux density and flame temperatures specified in the certification standards over a range of operating conditions, allowing the investigation of the effect of fuel type and flame equivalence ratio. The calibration methods to achieve the nominal values that define a standard flame are discussed in detail. The results obtained are compared across different test scales to ensure consistency.

The thesis delves into the experimental methods (infrared thermography, thin-film gauges and calorimetry) and associated challenges to measure heat flux density and temperature of the flame or emissivity and temperatures of the sample. One of the main sources of error when measuring the surface temperature of rapidly degrading material using conventional infrared thermography is the change in emissivity. To overcome this difficulty, we propose a technique based on two-colour pyrometry which does not necessitate the *a priori* knowledge of the specimen emissivity. The thesis provides an introduction in the topic and discusses in detail the radiative transfer model and hardware selection necessary to reduce the overall error contributions. Instead of measuring the signal over a wide spectral range, the ratio of the signals acquired through two narrow band-pass filters is used under the main assumption that the scene remained unchanged. This requires however, that the acquisition frequency of the camera and optical filter selection is tailored to the experiment. We also propose a post-processing methodology and a set of calibration experiments using a high-temperature black body. A comparative study with different composites and metals shows that the post-processing significantly reduces the measurement error.

Finally, the effect of flame chemistry on the degradation behaviour of carbon fibre specimens is investigated by exposing them to kerosene and gas flames. Some of the findings confirmed already available literature, but others come to light as a result of the research reported here. It is for instance known that tests using a propane gas flame lead in general to higher residual mass or residual tensile strength following fire exposure. However, gas torches are an essential tool for the scientific fire community, and we demonstrate that a gas flame can be tailored to induce a thermal damage similar to that of a calibrated kerosene flame. The major contribution from this work is thus its comprehensive approach towards scaling fire testing while providing scientific infrastructure that can used for more fundamental combustion studies in the future.

TABLE OF CONTENTS

LIST OF TABLES

LIST OF FIGURES

LIST OF SYMBOLS AND ACRONYMS

Latin

c_p	Heat capacity at constant pressure [J/K]
d	Flame diameter [mm]
D_{tube}	Tube diameter [m]
h	Planck constant
h_c	Convective heat transfer coefficient [W/(m^{2}K)]
H	Standoff distance between burner and specimen [mm]
H/d	Dimensionless separation distance [-]
$IBR_{cam}(T)$	Camera in-band radiance [W/(m^{2}sr)]
k	Turbulence kinetic energy [J/kg]
k_f	Thermal conductivity of foulant [W/(mK)]
$\dot{m}$	Mass flow rate of water [kg/s]
L	Total spectral radiance [W/(m^{2}srcm^{-1})]
m_f	Amount of soot deposited per unit area [kg/m^2]
q	Thermal power [W]
$\dot{Q}$	Heat flux density [kW/m^2]
r	Radial distance from stagnation point [mm]
$r(T)$	IBR signal ratio [-]
rc	Radiance correction [-]
Re	Reynolds number [-]
R_f	Fouling factor [m^{2}K/W]
S	Stagnation point [-]
T	Temperature [°C]
v	Velocity [m/s]
$\dot{V}$	Water volume flow rate [m^3/s]
x_f	Thickness of soot layer [m]
y	Vertical displacement [mm]

Greek

α	Absorptivity [-]
Γ	Soot deposition and removal rate [m^{2}K/W]

Δ	Difference between two quantities [a. u.]
ε	Emissivity [-]
λ	Wavelength [μm]
μ	Dynamic viscosity [kg/(ms)]
π	Circle constant [-]
ρ	Density [kg/m^3]
ρ	Reflectance [-]
σ	Wavenumber [cm^{-1}]
σ_{low}	Lower bandpass filter stop band [cm^{-1}]
σ_{high}	Higher bandpass filter stop band [cm^{-1}]
τ	Transmittance [-]
Φ	Equivalence ratio [-]
ω	Specific rate of dissipation [1/s]

Subscripts

atm	Atmosphere
B	Boltzmann
BB	Black body
bkg	Background
c	Clean (in the context of soot deposition)
c	Convective (in the context of heat transfer)
cam	Camera
e	Emitted
f	Fouled
fl	Flame
ft	Filter
LS	Large-scale
p	(At constant) pressure
r	Radiative
σ	Wavenumber
s	Sample
SS	Small-scale
t	Transported
WL	Wetted length

Acronyms

1C	Single-color
2C	Two-color
AC	Advisory Circular
AEC	Automatic exposure control
ASTM	American Society for Testing and Materials
BTU	British thermal unit
C	Char
CAA	Civil aviation authority
CF	Carbon fibre
CFD	Computational fluid dynamics
CFR	Code of Federal Regulations (in the United States)
CFRP	Carbon fibre reinforced polymer
COTS	Commercially available off-the-shelf
CRIAQ	Consortium de recherche et d'innovation en aérospatiale au Québec
DSC	Differential scanning calorimetry
DSLR	Digital single-lens reflex camera
EASA	European Union Aviation Safety Agency
FAA	Federal Aviation Administration
FOV	Field of view
FPA	Focal plane area
FRP	Fibre-reinforced plastic
FTIR	Fourier transform infrared spectroscopy
FW	Filter wheel
G	Gas
GF	Glass fibre
H	Hydrogen (chem.)
HDR	Hemispherical Directional reflectometer
HRR	Heat release rate
HUR	Heat-up rate
I^*	Intermediate
IA	Illuminated area
IBR	In-band radiance
ICAO	International Civil Aviation Organization
IR	Infrared

IRT	Infrared thermography
ISO	International Organization for Standardization
SST	Shear stress transport
LVTD	Linear variable differential transformer
MS	Multi-spectral
N/A	Not applicable
N/C	Normally closed
N/O	Normally open
NCAMP	ational Center for Advanced Materials Performance
ND	Neutral density
NEdIBR	Noise equivalent differential IBR
NETD	Noise equivalent temperature difference
NIST	National Institute of Standards and Technology
O	Oxygen (chem.)
OD	Optical density, decadic absorbance
OH	Hydroxyl (chem.)
OOA	Out-of-autoclave
OSU	Ohio State University
P	Polymer
PFA	Perfluoralkoxy (Telfon®)
PLA	Polylactic acid
PMC	Polymer matrix composite
PRV	Pressure relief valve
R	Radical
ROI	Region of interest
RT	Radiometric temperature
RTD	Resistance temperature detectors
SARP	Standards and Recommended Practices
SD	Standard deviation
SEM	Scanning electron microscopy
SS	Stainless steel
TC	Thermocouples
TCCA	Transport Canada Civil Aviation
TES	Temperature-emissivity separation
TFG	Thin-film gauge
TGA	Thermo-gravimetric analysis

TR	Temperature range
TTI	Time-to-ignition
UTS	Ultimate tensile strength
X	Halogen or phosphorus radical (chem.)
XFA	Xenon flash thermal constant analyzer

CHAPTER 1 INTRODUCTION

The objective of this work is to increase the understanding of the thermal degradation of aerospace polymer-matrix composite (PMCs) materials in the context of in-flight/post-crash fire hazards, through the use of small-scale tests. A key aspect of the work presented is thus the development of experimental infrastructure capable of generating the range of testing conditions relevant for such scenarios. The scope is restricted to materials intended to serve as firewalls, i.e. composite materials that separate engine fire zones from other compartments and must prevent the propagation of fire. The main scientific contributions of the work stem from the comprehensive approach implemented, combining time-resolved assessment of the material degradation processes, including the evaluation of mechanical properties, with meticulous flame calibration and the implementation of advanced diagnostic tools. Specifically, this approach allowed one of the first investigations of the effects arising from the chemistry of the flame on the thermal degradation of the composite specimens. The small-scale test rig developed is used to evaluate the fire resistance of the most extensively used PMC material system in the aerospace sector: carbon-fibre reinforced epoxy.

1.1 Composites in aerospace application

From the very beginning of the age of flight, emphasis in aircraft development has always been on both proper material selection and sophisticated aeronautical design. Aircraft weight is at the heart of these design constraints. The invention of the gas turbine dramatically increased aircraft power and range, clearing the way for civil aviation as we know it today. Engineers around the world have since continued to increase the power-to-weight ratio of airplanes, through the enhancement of engine efficiency and the implementation of new materials to decrease weight.

The advent of advanced polymer-matrix composite materials (synonymously used in the following for fibre reinforced polymers), and their increasing use in the aerospace industry contribute significantly to weight reductions. A modern commercial aircraft, as for instance the Boeing 787 series, include over 50% by weight (80% by volume) of composite materials [1], as illustrated in Fig. 1.1. These innovations are, however, always implemented with safety considerations in mind, as opposed to the early days where the Wright brothers reportedly shook hands as if it could be for the last time before their history-making first flight [2]. Since then, the safety of flight has evolved alongside the manifold improvements in aircraft design. The demand for light-weight yet strong and versatile materials for aircraft components has traditionally been met by high-strength aluminum alloys, but their resistance to fatigue and corrosion is limited. Composite materials can be tailored to provide a wide range of otherwise contradicting properties, such as high stiffness

and light weight, which makes them particularly interesting for demanding aerospace applications. Aside from stringent structural and mechanical requirements, fire safety concerns are a key part of the material design and selection strategy. This is obviously a key concern for the use of PMCs in aerospace, as the polymer matrix is typically combustible.

Although one can find many different composite materials in aircraft structures, limiting ourselves to fibre reinforced polymers (FRP), the two most common are glass fibre reinforced phenolic resins and carbon-fibre epoxy composites. Phenolic composites are the go-to standard in aircraft interiors and account for up to 90 % of cabin furniture. They are typically used as single skin laminates or as face sheets, sandwiching Nomex honeycomb cores. The extensive use of phenolic resins with glass fibre reinforcement is due to their low weight, low flammability and good fire resistance. Carbon-fibre reinforced epoxy composites, on the other hand, are standard for many components and structures outside the pressurized cabin. They are also used as thin laminates or sandwich structures using predominately Nomex and aluminum honeycomb cores. They are used for cowlings, wing fins, fuselage structures and doors. Lightweight and offering an interesting combination of mechanical properties, the biggest drawback of carbon/epoxy composites is their low flammability limit and their rapid thermal degradation. Flame-retardant additives or the use of alternative polymer resins in the matrix are common fireproofing strategies but are often less desirable from a mechanical and economic standpoint.

The use of advanced composite materials tailored to perform in structurally demanding and high-temperature environments is clearly not yet fully exploited. Even when looking only at aerospace applications, the experimental investigation of composites under flame attack remains a broad subject, in line with the extensive use of these materials inside, outside and within the fuselage (cf. Fig. 1.1). The combustion of composite materials is complex, with competing physical and chemical processes in the solid and gaseous phase that eventually lead to the alteration of mechanical properties. The rate of this degeneration is exceedingly difficult to predict but important to assess for fire safety. An important step in the design and development of tailored materials fulfilling the long list of requirements is a better understanding of their degradation behavior. An improved understanding allows to advance existing numerical models and vice versa.

1.2 Fire hazard in aerospace applications

Among the safety risks to mitigate when designing aircraft, fire safety considerations take an important role and affect all areas of design and planning. Already at comparably low temperatures between 100 °C – 200 °C, thin composite laminates start to soften and deform. This directly affects their structural integrity and can lead to buckling, distortion and ultimately to the failure of load-bearing structures. At moderate temperatures in the range from 300 °C to 400 °C, the polymer

Figure 1.1 Usage of materials in the Boeing 787. Air-frame and primary structures are comprised half of carbon fibre reinforced plastic and other composites. Reprinted with permission from [3]. Copyright 2016 The Boeing Company.

matrix thermally begins to degrade, with pyrolysis reaction producing flammable and potentially toxic volatile species. The lower flammability limit is the minimum concentration of a combustible gas needed to form a flammable mixture and is a temperature dependent value. If an oxidant is present, such as air, this outgassing can ignite and release a large amount of heat, soot and smoke. Furthermore, polymer matrix materials with low flammability limits increase the risk of flame spread which may quickly compromise the overall safety of the aircraft.

The design of modern aircraft addresses the risk of a potential fire by three main strategies: separation, isolation and control. To prevent the emergence of fire, its prerequisites, i.e. fuel, ignition source, and oxygen, are kept *separated* as much as possible. In case a fire occurs, it is *isolated* from spreading to other parts and *controlled* to minimize its intensity. These three principles are addressed by applying several active and passive fire protection strategies. Active systems will detect, sense and extinguish fires whereas passive measures include among others separation by routing, usage of non-combustible materials or compartmentalization. The work presented here focuses on the latter, more specifically on the evaluation of materials intended to implement compartmentalization.

Figure 1.2 shows schematically the different divisions of an aircraft engine which are classified in zones. When containing potential ignition sources or the risk of flammable fluid leakage, zones are labelled as *designated fire zones*. One prominent passive fire protection strategy consists in separating a fire zone from adjacent zones by a firewall. A typical firewall location within the engine pod is for example the area surrounding the central engine fire zone where fuel lines are routed (Fig. 1.2). For an in-flight fire scenario, time is the most critical parameter and the aircraft is designed to provide the crew with 15 min to safely land the aircraft and evacuate the passengers, before the cabin becomes completely uninhabitable by smoke and toxic fumes. During a post-crash scenario, the firewall must avert flame spread and burn-through towards the strut and outer nacelle

areas, from which the fire could spread towards fuel tanks and passengers.

Due to the extent of fire zones outside the fuselage, firewalls cover large areas and their weight contribution becomes significant. Aircraft and engine manufacturers thus seek to replace the traditional metal components used for firewalls by composite material systems. The development of composites suitable for such application proves to be challenging as the materials' susceptibility to fire is a major factor in limiting their usage in such demanding aircraft applications. This task requires the quantification of the response of a material system following exposure to fire, and therefore to quantify the characteristics of the fire itself. The severity of a flame can be described by its heat release rate (HRR) and its temperature. The HRR is a quantitative measure of the overall energy released, it is therefore a global thermal power [W], whereas the temperature is a scalar associated with a position in the flame. Both metrics have limitations when it comes to characterizing a fire hazard, with the heat flux density [W/m^2] often used to quantify the heat received by a surface from different flame types [5]. It is common practice in fire research to evaluate the fire resistance of materials and components by exposing them to heat flux densities derived from empirical data and expected to be representative for a given threat (Tab. 1.1). A discussion on the thermal degradation of aerospace-grade composite materials must thus also touch upon the applicable standards and implied test conditions.

Table 1.1 Typical values of heat flux density for different fire hazards. Data taken from [6].

Hazard	Heat flux density [kW/m^2]
Small smouldering fire:	2–10
Trash can fire:	10–50
Cabin fire:	50–100
Post-flashover cabin fire:	>100
Jet fuel fire:	150-200

1.3 Component certification and regulations

Commercial airplanes used for the transport of people and goods are subjected to extensive safety regulations, including several covering the topic of flammability. The responsibility to establish and enforce regulations is held by the national civil aviation authorities (CAA), as for example Transport Canada Civil Aviation (TCCA) or the Federal Aviation Administration (FAA) in the United States. CAAs are further grouped in transnational umbrella organizations as for example the European Aviation Safety Agency (EASA). Additionally, the International Civil Aviation Organization (ICAO), with its 191 member states, link FAA, EASA, and other CAAs. The ICAO releases Standards and Recommended Practices (SARPs) that are not legally binding but are used as baseline

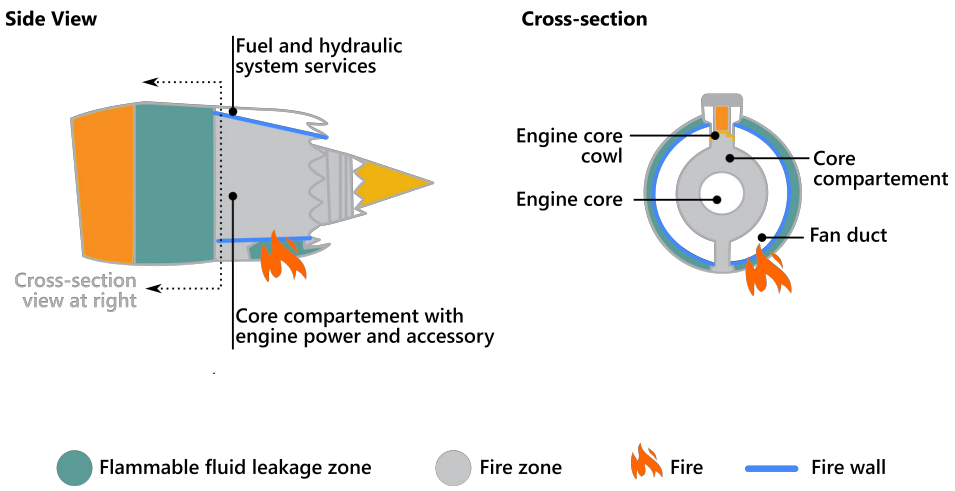

Figure 1.2 Compartmentalization in an auxiliary power unit (left side) and in a typical engine pod. Firewalls isolate the fire from the rest of the airplane and are highlighted in blue. Picture adapted from [4], © Boeing.

by national CAAs. The regulations prepared by national CAAs, such as the EASA and the FAA are legally enforceable within their respective jurisdictions. It is worth noting that FAA regulations are commonly adopted by all CAAs and are thus used essentially worldwide [7]. This is further supported by the ongoing efforts of the EASA and the FAA to harmonize their rules [8], motivating the focus of the current project mainly on FAA regulations.

The FAA fire test requirements are divided in two major categories depending on whether a component is intended for installation inside or outside the fuselage. The present thesis is focused on the latter, as the firewall considered are used in acoustic liners or fan cases for turbofan aircraft engines. They form the boundaries of fire zones, i.e. the interface between primary or secondary air flow and accessory sections of the engine, as indicated in Figure 1.2. In the case of an accidental fire, for instance in the fuel handling systems, these components shall act as a firewall and prevent flame propagation, thus providing the crew with enough time to detect the problem and safely land the aircraft. As part of the extensive certification process, these components have to undergo fire resistance testing to demonstrate that they can withstand a flame attack for a prescribed time while maintaining their mechanical properties. The specific requirements for a firewall will vary depending on the installation location and those of concern for this project are *fire resistant* or *fireproof*, i.e. to exhibit no burn-through for 5 or 15 min, respectively when exposed to a so-called standard flame. This flame is calibrated to yield a heat flux density of $(116 \pm 10)\,\mathrm{kW\,m^{-2}}$ and temperature of $(1100 \pm 80)\,^{\circ}\mathrm{C}$ at the stagnation point [9]. An overview of the broad range of tests and regulations as well as a more detailed discussion of the definitions of fire resistance and fire proofness are provided in Ch. 2.

1.4 Bench-scale tests

The certification tests described in the previous section are intended to provide a simple pass/fail verdict that can readily be established using simple instrumentation and observation. As is often the case in the aerospace industry, practice is to err on the side of caution and be very conservative, relying on well established albeit sometimes crude experimental techniques. The use of simplifying assumptions is thus typically one-sided; for instance, neglecting important influencing factors such as the accumulation of soot during heat flux measurements that result in conditions during a test being often harsher than the nominal requirement of the certification standard. This lack of information on the effective conditions the materials are subjected to and the limited measurements carried out on the specimens during and following exposure to flames make actual certification tests largely unsuitable to go beyond the pass/fail dichotomy and provide understanding of failure mechanisms.

This understanding is, however, essential to enable the design of novel lightweight and fire resistant composite material systems. The scientific research work carried out to gather this understanding often relies on one of two main approaches, either study thermal degradation in simplified settings such as cone calorimeters that cannot be extrapolated to certification-like conditions or attempt to recreate the already simple certification flames at the bench-scale, relying only on flame temperature and heat flux density as control parameters. These approaches neglect the complex interplay between the pilot flame providing the thermal stress, the specimen and the diagnostic tools used to gather information on the degradation process. Overcoming the limitations of these simplified approaches requires well thought-out bench-scale tests in which advanced diagnostic tools can be implemented, to measure the flame characteristics and the evolution of the material properties in the specimen precisely, and with high spatial and temporal resolution. Such experiments at the coupon level can be carried out at a cost orders of magnitude lower than full-scale certification tests, allowing quick screening of potential material systems and parametric studies to be implemented to shed light on the influence of key control parameters, such as heat flux density, temperature, flame type, etc.

From a purely scientific perspective, the problem at hand can be boiled down to the exposure of a combustible solid material to a flame, a topic which can be tackled from many different angles, covered by a vast amount of literature produced over the last century across many different disciplines. Early work focused on the development of a theoretical description of the heat transfer induced by a flame-wall interaction. The heat transfer mechanisms involved are convection, radiation, and thermochemical heat release. In the particular case of a normally impinging flame, a negative pressure gradient drives the flow of the reacting gaseous mixture and sustains the growth of laminar boundary layer with increasing radial distance from the stagnation point. Rosner [10,11]

and Gray [12] developed a semi-analytical approach to adequately predict rates of convective heat transfer from gas flames to a low temperature wall considering diffusion and recombination of reactive species in the boundary layers. Anderson and Stresino [13] showed that the predicted convective heat transfer considering thermochemical processes is in good agreement with experiments for a low temperature methane flame and copper targets. Kilham and Purvis [14] could show that the agreement between experimental and theoretical values for high temperature gas flames will depend on the mixing induced turbulence and the relative distance of the primary reaction cone and the surface. Baukal [15] experimentally studied the different heat transfer mechanisms involved with the help of gas flames and concluded that contributions from non-luminous radiation and from thermochemical heat release can be neglected and that convective heat transfer should be considered the dominant mechanism. For flames from liquid fuels and more complex hydrocarbons, the flame radiation cannot be neglected and may even become the dominant heat transfer mechanism, for instance for large flames or pools of fire [16].

With the integration of composite materials into aircraft structures, accidents involving fire brought new challenges and the behavior of this new class of materials under flame attack received increased attention in the research community. Dao and Asaro [17–19] have attempted to study the failure behavior of glass fibre composites under compressive load and one-sided heat flux based on the temperature profile of the specimen front and back face and to derive from it a similar design criteria approach as used for aluminium alloys. Johnston et al. [20] presented a simplified screening tests with a gas torch and post-fire evaluation of mechanical properties. They could demonstrate that small-scale tests are a suitable method to rapidly screen flame-penetration resistance and concluded that by adapting the flame impingement area to the specimen size, the relative damage extent could be better evaluated. More recently, overviews of analytic and computational approaches may be seen for example in Browne [21], Hörold [22] and Lautenberger [23]. They all require material properties as input to numerically predict the thermal degradation of composite materials with surface temperature and emissivity playing a key role for modelling ignition and flame propagation.

One of the biggest challenges in large-scale certification testing is currently the availability of allowed burners, as the hardware specified in the documents is outdated. In small-scale testing, the challenge lies in the absence of harmonized hardware and settings, complicating the comparison of results between test scales. Gas torches are simple and available off-the-shelf for thermal powers covering several orders of magnitude. They are therefore a popular solution in many existing bench-scale setups. Without additional modifications, control of important combustion parameters is limited and make results difficult to compare across different setups. Furthermore, the flame characteristics of a gas flame differ substantially from oil-fuelled burners that are now mandated in large-scale certification tests. Another critical aspect is the measurement of key material properties in the harsh experimental conditions with suitable temporal and spatial resolution. One of these key

properties is the temperature at the surface of the burning material, to which many others are tied. Measurements based on sensors in physical contact with specimen provide only local assessment of the temperature and needs careful probe design to withstand the elevated temperatures. Calibration and correction are also needed to account for radiative losses and catalytic effects. Alternatively, contact-less optical methods only require a direct line-of-sight to provide a measurement, but applications in reactive atmospheres remain complicated to account for contributions from the impinging flame or background.

With regulation bodies currently working on the harmonization of existing standards, specifically to narrow down the list of burners allowed for certification testing in the future, it is crucial to develop bench-scale experimental infrastructure capable of creating the range of testing conditions relevant for different burner types and to generate data sets needed to support the understanding of the mechanisms at play. The cornerstone of this approach is the implementation of measurement techniques to quantify incident heat flux density or surface temperature evolution, considering appropriate correction and calibration techniques to account for the harsh test conditions. The study of the flame-induced thermal degradation of carbon-fibre composites at the bench scale thus requires the development of a versatile well-controlled infrastructure and the implementation of suitable diagnostic techniques.

1.5 Research objectives

The work presented here was carried out in the context of a research project funded by the Consortium de Recherche et d'Innovation en Aérospatiale au Québec (CRIAQ), with Pratt & Whitney Canada as the main Industrial partner and in collaboration with Université Laval. At Polytechnique Montréal, two other PhD students were also involved full-time in the project, one tasked with the development of a numerical model and another developing new fireproofing strategies. The scope of the work presented in this manuscript is limited to the response to fire of composites used as firewalls for passive fire protection of aircraft jet engine nacelles. More specifically, a single skin carbon-fibre composite specimen exposed to a flame is considered, addressing the following research objectives:

Develop and calibrate a bench-scale flame capable of creating the conditions prescribed in certification tests. An important first step is the design of an infrastructure to recreate not only conditions representative of large-scale tests but also to go beyond them. The development of a small-scale kerosene burner and a detailed characterization of its flame is at the heart of this work. The flame characterization also requires a comparison between the methods and devices prescribed by certification bodies and state-of-the art instruments available in reactive flows research laboratories.

Measure critical parameters to characterize material degradation in-situ. The use of infrared thermography (IRT) in the fire test rig can provide in-situ measurement of surface temperature and emissivity with high spatial and temporal accuracy. This technique has however seldom been implemented under reactive atmospheres where the surface properties (microstructure, emissivity) change rapidly, requiring the adaptation of an advanced signal treatment approach (two-color pyrometry). The quantitative measurement of these critical parameters could enable multi-physics numerical models to more accurately account for the radiative contribution in the heat transfer between the specimen and the flame, therefore more precisely estimating material removal rate as a function of time.

Assess the effect of flame chemistry on thermal degradation. Beyond the heat flux density and flame temperature, the composition of the reactive atmosphere in contact with the composite material under investigation will affect the degradation rate and the evolution of its mechanical properties. This can be for instance the result of the presence of different radicals and oxidative species in the pilot flame exhaust gases, as well as from varying amounts of soot and unburnt species impinging on the specimen surface, changing the nature of the heat flux received. Of particular interest is the effect of changing the type of fuel used in the pilot flame, motivated by the now mandatory use of kerosene flames in certification tests where propane flames used to be widely employed. Focus is not solely on the thermo-chemical degradation, but also on its close interrelation to mechanical properties and the inception of structural failure.

The originality of the present work stems from the fact that it combines the development of a versatile small-scale infrastructure including a kerosene burner, with a IR thermography post-processing technique that accounts for various error sources when measuring the surface temperature of burning materials. The test and measurements method are then applied at the coupon-level to investigate the effect of flame chemistry on material decomposition with never before achieved temporal and spatial resolution. These results put the material degradation into perspective with the fire source itself and compare the residual properties from specimens exposed to well-characterized gas and oil-flames.

1.6 Outline of the thesis

The topic of this thesis - the fire testing of composite structures - touches upon many different fields but might be of particular interest to two groups of people: those working in the field of fire resistance testing and those aiming to monitor material properties during combustion. Accordingly, the document presents relevant background for each topic in a concise and complete manner.

Chapter 2 first presents and defines important vocabulary regarding the combustion of solids and

provides the necessary basic concepts and definitions. The basics of flammability testing are then introduced, relating measurable quantities to the fire properties of materials. An overview of the broad range of tests and regulations as well as a more detailed discussion of the definitions of fire resistance and fire proofness is provided. Since the thermo-mechanical degradation of composite materials is the main interest of this work, their behavior when exposed to a flame is reviewed, followed by a short introduction to fireproofing strategies. A technical summary of flammability test procedures for aircraft firewalls and the corresponding standards is given due to their paramount influence on the design choices and requirements for the small-scale test rig. Existing burner and test rigs ranging from large-scale to intermediate scale and small-scale setups are discussed. The current limitations of existing experimental facilities is then discussed, before concluding with an overview of the state of the art for diagnostics and experimental techniques in combustion research applied to the problem at hand.

The developed of the small-scale test rig and burners as well as the characterization methods are presented in chapter 3. The discussion on the characterization methods touches upon thermocouple measurement, heat flux measurements and infrared thermography. A total of two test rigs were developed, one that allows for static tests and one that can be readily implemented in a tensile machine for simultaneous testing of mechanical and thermal resistance.

The chapters 4 to 6 contain the main results and findings of this work, part of which have also been submitted to peer-reviewed journals. Chapter 4 discusses the scaling methodology and how small flames can be used to mimic large flames. Heat flux measurements and flame calibration for different types of flames and at different scales are discussed. Chapter 5 shifts the focus on the exposed specimens and highlights why surface temperature measurement using infrared-thermography still poses experimental challenges in the context of our tests. This study demonstrates that the emissivity of fibre reinforced plastics decreases as temperature increases. Methods and models relying on constant values assessed at room temperature may as a result significantly underestimate surface temperature and other properties dependent on emissivity. Benefiting from the findings in the previous two chapters, chapter 6 sheds a light on the effect of flame chemistry on the thermal degradation of carbon-fibre epoxy composites. The extensive experimental campaign implements gas torches commonly used in literature, along with reported operating conditions, and compares the material degradation behavior to specimens exposed to the small-scale kerosene burner and a diluted propane flame.

The general discussion in chapter 7 puts the results from the previous chapters into perspective and examines the limitations of our work. We conclude in chapter 8 with a summary of the performed research and present suggestions for future work arising from this work.

CHAPTER 2 LITERATURE REVIEW

2.1 Polymer combustion

2.1.1 Combustion of solids fuels

To discuss material fire resistance, it is interesting to review first what makes solid materials burn to begin with. A typical path for thermal decomposition and combustion is shown in Fig. 2.1 [24]. A combustible solid is one that is able to release combustible gas as it heats following receiving an external energy supply. The initial heating of the exposed material causes the surface temperature to rise. The rate of the temperature rise depends on the applied heat flux, the heat loss to the surrounding, the latent heat of any phase change involved and the thermo-physical properties of the solid [24, 25]. As temperature exceeds the initial thermal decomposition temperature (Fig. 2.2, t1), chemical reactions begin and volatile components are released. These mostly endothermic reactions constitute pyrolysis and in the case of polymers the species produced include carbon monoxides, hydrocarbons, oils and tar, among others [26]. The decomposition zone first develops close to the surface and then slowly propagates to the interior.

The combustible volatiles (pyrolyzates) diffuse in the surrounding air to form a fuel-oxidizer blend. If the minimum concentration of combustible gases needed to form a flammable mixture (Fig. 2.2, t2) is reached and an ignition (pilot) source is present, a flame forms and propagates towards the material surface. This minimum concentration is called the lower flammability limit and is temperature dependent. Another temperature dependent value is the rate of pyrolysate formation (slope of curve between t1 and t2 in Fig. 2.2) and it must be above the critical mass flow rate able to sustain the combustion process for the flame to anchor itself on the solid surface. This is usually considered as the moment of ignition (t3) and the corresponding temperature is referred to as the

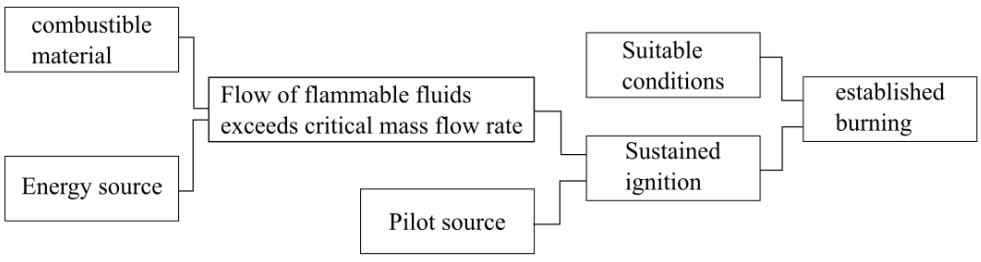

Figure 2.1 Schematic representation of piloted ignition for a combustible solid. Adapted from [24].

firepoint. Once a stable flame is established in the gas phase adjacent to the solid surface, strongly exothermic combustion reaction can provide the heat necessary to sustain the pyrolysis of the solid. The flame exchanges heat with its surrounding by radiation and convection. For small flames, the convective heat loss is significant and the flame might extinguish itself if the heat generated by the combustion cannot compensate for it. Under optimal conditions, if enough combustible volatiles are generated and the heat generated by the flame is higher than losses, the flame can start to spread over the surface, a process that can be viewed as a consecutive series of ignition events [7, 27]. After all volatiles have been consumed by the fire or released to the atmosphere, the remaining solid can be considered as char. It also starts to decompose above approximately 500 °C, a temperature significantly higher than for pyrolysis, through a process termed gasification [28]. Upon complete combustion of all organic material solid carbon, ash remains as powdery greyish residue made of the incombustible mineral and metallic content initially present in the solid. To sustain the combustion of a carbon-based solid, the heat released by the oxidation of gaseous effluent, minus losses to the environment, therefore needs to exceed the energy consumed by the pyrolysis and gasification reactions.

Combustion and fire are inescapably associated with temperature. Aside from intuition, this parameter indeed provides the appropriate means to discuss the series of physical and chemical events involved when a material burns. The previous discussion focused on piloted ignition where the actual combustion is triggered by an external spark or flame. In absence of such a pilot source, a flammable gas mixture can still be brought to self-ignition solely by heating up the system. The time lag between the instant a certain temperature is established and the moment where the gas-fuel mix ignites is the time to ignition (TTI). As a general trend, TTI decreases as temperature increases or incident heat flux increase. For instance, a carbon/fibre epoxy composite laminate exposed to a one-sided heat flux of $30\,\mathrm{kW/m^2}$ ignites after more than 300 s whereas the TTI drops to about 50 s when the heat flux is doubled [29]. The lower limit at which auto-ignition occurs if the exposure time approaches infinity is called auto-ignition temperature. As shown in Fig. 2.2, the lower temperature limit and the auto-ignition temperature are the respective upper and lower boundaries in-between which a combustible gas can be ignited by a pilot flame [30]. At lower temperatures, the sample cannot be brought to ignition and at temperatures above it will self-ignite [31].

2.1.2 The chemistry of polymer combustion

The combustion of solid polymers will be discussed here, with the physical and chemical processes present shown schematically in Fig. 2.3. Following the previous phenomenological discussion on the combustion of solids in general, in the following the thermochemistry and chemical kinetics of polymers combustion will be presented for the condensed phase, the mesophase and the gas phase.

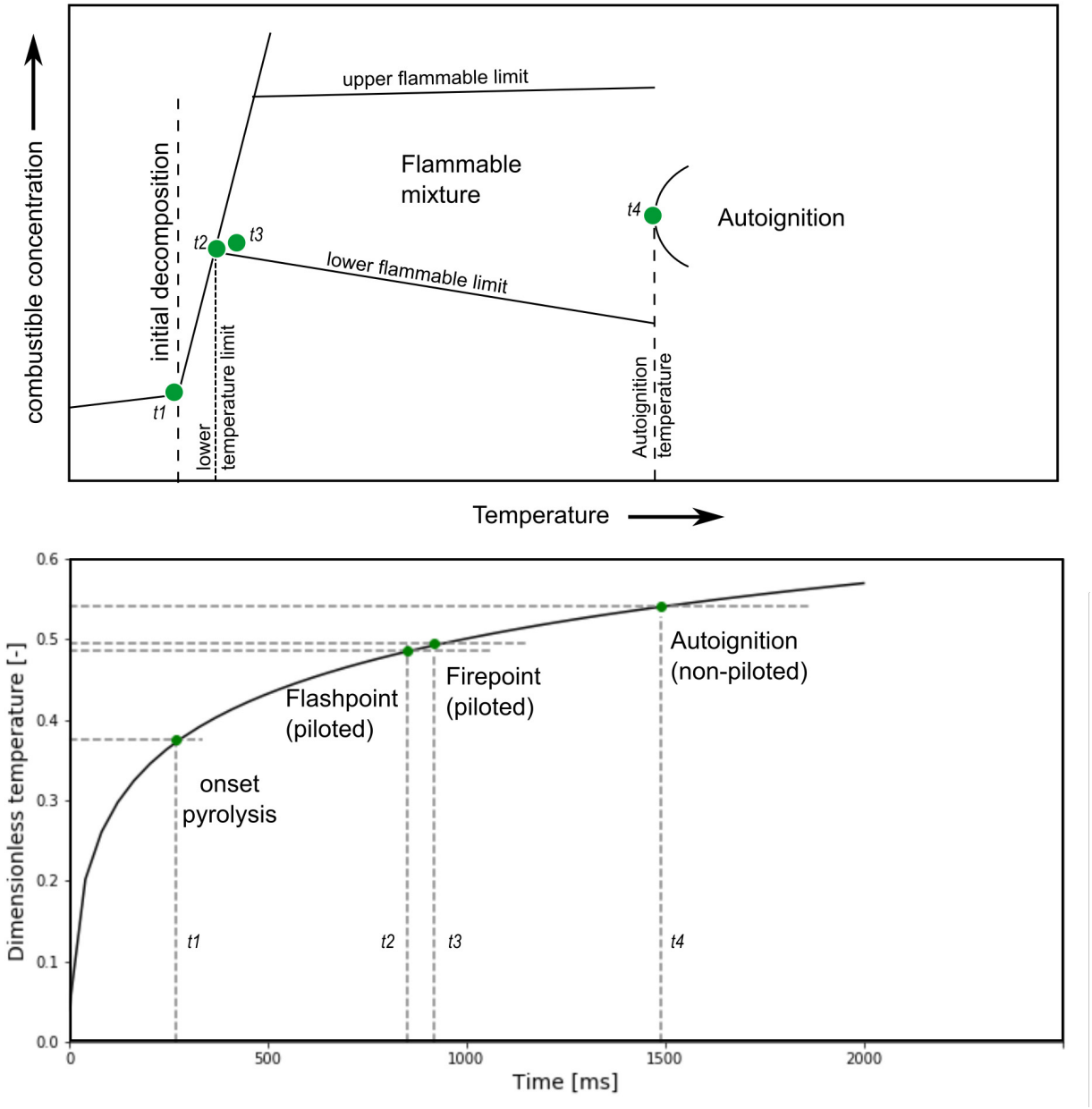

Figure 2.2 Schematic representation showing the effect of the surface temperature of a thermally thick solid exposed to a one-sided heat flux on the times to pyrolysis onset, piloted ignition and auto-ignition. The evolution of temperature over time is linked with the evolution of combustibles with temperature. Upper part of the figure adapted from [31].

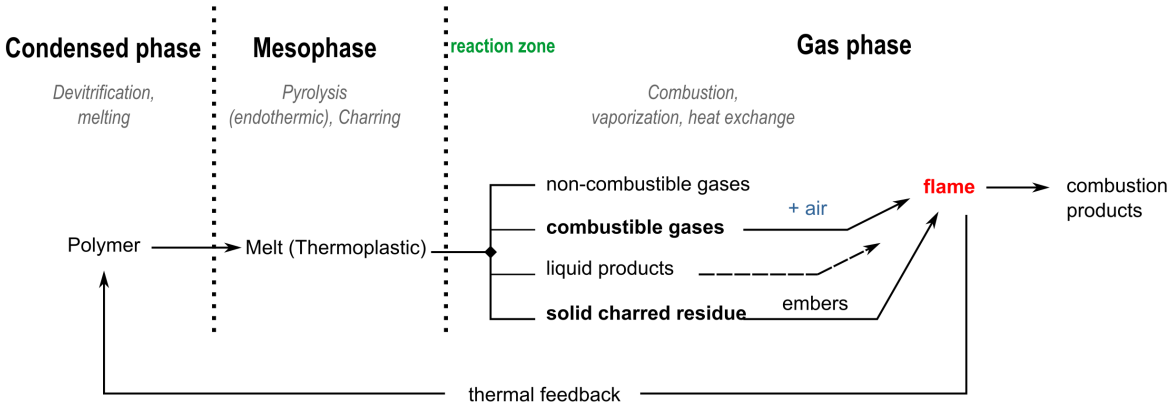

Figure 2.3 Physical and chemical processes involved when a solid polymer is burning.

Mesophase and condensed phase reactions

The mesophase designates the zone close to the surface where chemical processes linked to thermal degradation and pyrolysis take place (Fig. 2.3) and includes reaction products in different forms. The reactions in the mesophase and condensed phase directly translate to a progressive mass loss as shown in Fig. 2.4, for the example of a glass fibre composites exposed to a constant one-sided heat flux. In the first few seconds (I), the mass remains unchanged until the surface temperature has risen high enough to initiate primary decomposition. In this stage (II), the generation of volatiles is dominant and the mass loss rate is elevated. Depending on the formulation of the polymer, a first char layer may form. This layer will grow in thickness with continued flame exposure and intensity and thus insulate and protect the underlying material. The transition between stage II and III is a question of material thickness. As the resin is progressively consumed by the flame, the composites becomes a thermally thin material, which in turn accelerates the thermal degradation further. Consequently, the massloss rate in stage III is higher than in stage II.

The char formation ceases when all unreacted material is transformed or when the thickness of the char layer efficiently prevents heat or mass transfer between the underlying virgin material and the gaseous environment. As the temperature further increases, the lower decomposition limit of this char layer is eventually reached and causes it to gasify as well. In therms of chemical kinetics, a first order thermal degradation scheme provides a good basis to describe the system [32–34]:

$$\text{Polymer (P)} \xrightarrow{k_d} \text{Intermediate (I}^*\text{)}$$
$$\text{I}^* \xrightarrow{k_g} \text{Gas (G)}$$
$$\text{I}^* \xrightarrow{k_c} \text{Char (C)}$$

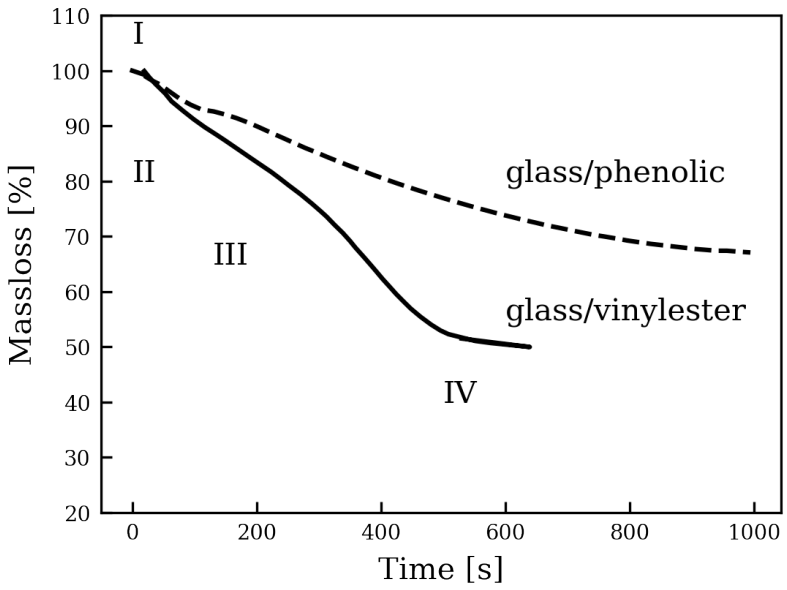

Figure 2.4 Typical massloss curves for glass-fiber composites with different resins and exposed to a constant heat flux of $50\,\mathrm{kW/m^2}$. Adapted from [5].

Chain branching reactions, initiated by intermediate radical species, will control the char formation rate. A commonly applied measurement technique to study the char formation yield is thermogravimetric analysis (TGA). Chemical degradation processes are also interesting with regard to the intramolecular rearrangements. Polymers are by definition long chains of oligomers or monomers units. Thermally or chemically activated degradation results in bond dissociation and this scission sets radicals free. At the end of stage III, the resin is completely depleted, part of the char is burnt as well and the unprotected fibres start to oxidize (IV). The mass loss curve slowly comes to a halt with the final residual mass being determined by the remaining fabric and char. The mass loss rate as well as the overall mass loss is not only driven by the experimental conditions but also by the char yield of the organic constituents. Resin formulations with higher yield result in the formation of a thicker insulating char layer, providing better insulation for the material located deeper below the surface. Examples of such char-forming matrices for composites include phenolic resins or many thermoplastics. Alternatively, thermosetting polymers such epoxy resins create only small amounts of char as they are thermally degraded and have thus much higher mass loss rates when exposed to the same heat flux.

Gas phase reactions

The outgassing of thermally degrading polymers is mainly composed of light hydrocarbons and will burn in a very similar way as other gaseous fuel mixtures such as syngas. Gas phase reactions

are thus of particular interest when studying the flammability and fire resistance of polymer based composite materials. A chemical reaction can be triggered either by thermal or chemical activation. The former increases the energy transferred to a molecule upon collision, and the latter results in the generation of intermediate products - radicals - that promote other chemical reactions. From the large number of chemical reactions occurring in the gas phase of a burning polymer, referred to collectively as the reaction mechanism, only a few of them are found to dominate the combustion process [35]. These are characterized by their large effect resulting from the small concentrations of highly reactive radicals that they involve, initiating, branching or terminating sets of chain reactions [36]. For the combustion of polymers and hydrocarbons in general, seven such chain reactions involve radicals of fuel (R), hydroxyl (OH), hydrogen (H), oxygen (O), and halogen or phosphorus (X) [35]:

$$\begin{aligned}
RH &\xrightarrow{k_1} R^{\bullet} + {}^{\bullet}H && \text{Chain initiation}\\
{}^{\bullet}H + O_2 &\xrightarrow{k_2} {}^{\bullet}OH + {}^{\bullet}O && \text{Chain branching}\\
{}^{\bullet}OH + CO &\xrightarrow{k_3} CO_2 + {}^{\bullet}H && \text{Chain carrying}\\
{}^{\bullet}OH + H_2 &\xrightarrow{k_4} H_2O + {}^{\bullet}H && \text{Chain carrying}\\
{}^{\bullet}H + O_2 &\xrightarrow{k_5} {}^{\bullet}HO_2 && \text{Chain termination}\\
{}^{\bullet}H + HX &\xrightarrow{k_6} H_2 + {}^{\bullet}X && \text{Chain inhibition}\\
{}^{\bullet}OH + HX &\xrightarrow{k_7} H_2O + {}^{\bullet}X && \text{Chain inhibition}
\end{aligned}$$

A superscript bullet indicates an active radical (intermediate product). Examples of inhibition reaction refer to the endothermic reaction of flame retardant resin additives such as halogens or phosphorus. The net molecular process for a generic fuel reacting with the surrounding atmosphere may thus be written as [35]:

$$C_cH_hO_mN_nX_x + (c + \tfrac{(h\text{-}x\text{-}2m)}{4})\, O_2 \longrightarrow cCO_2 + \tfrac{(h\text{-}x)}{2}\, H_2O + \tfrac{n}{2}\, N_2 + xHX$$

For balancing the equation, the combustion is assumed complete, meaning that all reactants are converted to water and carbon dioxide. In reality, combustion is in general incomplete, producing NO_x, unburned hydrocarbons, soot, and mineral acid gases. The actual composition of the products will depend on the resin and additives used for the composite matrix.

2.2 Fundamentals of flammability testing

Regardless of the particular aim of a fire test, the configurations typically consist of a 'standard' heat source to which a sample is subjected in a predefined orientation and for a determined amount of time. For the tests under consideration [9, 37, 38], a calibrated oil burner is used to ignite the

material. In fire tests that evaluate the ignition behavior of samples, the heat source is then a heating coil or lamp which are usually removed or shut down as soon as flames appear [39–41]. The discussion of the combustion is then limited to the self-sustaining combustion of the solid. However, for the fire tests of interest here, the heat source, i.e. the pilot flame, is not removed. This configuration is more complex and one needs to consider the interaction between the continuously fuelled fire of the burner, and the surface fire of the exposed material that might eventually quench when all combustible species are consumed.

2.2.1 Terminology

Fire: Can designate three different concepts in the English language. It may refer to the general concept of combustion, that is the exothermic reaction of a substance with an oxidizing agent [42], associated with emission of light. Fire may further be used to describe a controlled self-sustaining combustion that is set to provide 'useful' effects, e.g. in a gas stove, but it may also describe the opposite, an uncontrolled - often hazardous - not deliberately arranged fire. The visible part of a fire is called a flame.

Combustible solids: In the context of the combustion of solids, tests focus on either the desired or the undesired burning of a substance. In the former case, the solid is referred to as fuel whereas in the latter case, the solid may be any kind of combustible material. Experiments on solid fuels often study the performance of the combustion process, i.e. the thermal power released per unit mass of fuel consumed, and the applicability for a given use-case. The experimental apparatus to do so is a reactor. In contrast, the fire testing of combustible solids, for instance for use in construction or transportation, are usually performed to show regulatory compliance to fire safety codes. The corresponding tests are named flammability and fire tests.

Flammability vs. combustibility: The meanings of these terms depends on the context, both refer to either the likelihood that a material will ignite or the impact of a resulting fire hazard. By strict definition, combustibility refers to the ability of a material to burn and to sustain this process [43], without specifically addressing the concept of ignition, whereas flammability is associated with the initiation of combustion. So to answer if a particular material is flammable and to which extent, one needs to translate the definition to properties that can be directly or indirectly measured. The propensity to inflame may thus be defined as "*the ease with which a material is ignited (*ignitability*), the associated intensity of burn and heat release (*mass burning rate, heat release rate*), its tendency to spread fire (*flame spread rate*), and the rate at which it generates smoke and toxic combustion products during the gasification and burning*" [7]. To be very explicit, condensed phases of materials will burn when, and only when, they generate combustible gases upon calefaction [1]. For

[1] Calefaction refers to the state of being warmed or heated

the majority of combustible solids, the generation of combustible gases originates from chemical decomposition induced by heat (thermal degradation). With this definition, it becomes evident that combustion and ignition are in fact dependent on phenomena occuring in the gas phase.

Fire vs. flammability tests: The fire research community has not agreed on a universal definition of flammability tests and how they differ from fire tests [35]. In many cases flammability tests refers to less harsh conditions and smaller sample sizes, with emphasis given to the study of the ignition behavior of a material. The term fire test is then applied for larger scales [2], intended to examine flame hazards. Since the experimental study of the present work is somewhat tangent to both cases, the terms are used interchangeably throughout this document.

2.2.2 Flammability tests for aircraft

One of the objectives of this work is to perform small-scale tests from which the behavior of samples in large-scale tests can be better understood and generate data that can be used to validate numerical models. The large-scale tests are certifications requirements that are commonly either performed by the aircraft component manufacturer in their facilities or in dedicated external fire laboratories. Any fire test configuration for a given component requires advance approval by the FAA to be considered as official certification. This large-scale assessment thus marks an essential milestone in demonstrating compliance with airworthiness standards, as required to eventually obtain a *type certificate* [3]. The large-scale tests planned in this project are to be performed under certification-like conditions to evaluate new materials and fire proofing strategies. The design of the small-scale rig shall thus be able to recreate these test conditions for the results to be of significance.

The complete list of regulations and airworthiness tests is presented in detail in the FAA Fire Test Handbook [45] and the CFR code. The test requirements linked to particular component are usually binding and specified on its technical drawing. Fire test procedures and standards involve two important definitions: fire proof and fire resistant. These definitions are by no means universal and will depend on the context, component, and applicable standard. Even if narrowed down to fire tests for firewalls in aircraft structure, the definitions slightly vary. It should be further noted that FAA documents use imperial units for the most part whereas international standards or European Standards use SI-units. To establish a common basis, the corresponding SI-units are provided in brackets.

fire resistant According to FAA AC20-135 and with respect to air ducts and fire zones[4], a com-

[2] The notion of "large" is not very specific as for instance whole buildings may be set on fire in the context of safety tests in construction.

[3] A type certificate is the formal FAA approval of new airplane [44].

[4] This definitions also applies for other components (e.g. fluid carrying lines, wiring, etc.), that are outside of the

ponent is fire resistant when it maintains its intended functions under heat and other conditions likely to occur at its particular location in the aircraft while withstanding a flame of (2000 ± 150) °F ((1093 ± 66) °C) for 5 minutes minimum [37]. ISO2685:1998(E) grades components, equipment, and structures located in fire zones as fire resistant if they withstand the application of heat by a standard flame for 5 minutes. A standard flame is furthermore defined as a flame with a temperature of (1100 ± 80) °C and a heat flux density received by a standard calorimeter apparatus[5] [9].

fireproof FAA AC20-135 grades a component fireproof if it withstands the aforementioned conditions for 115 min as well as or better than steel. ISO2685:1998(E) extends its definition of fire resistance to fireproof by the requirement that the component has to withstand the above mentioned conditions for 15 min [9].

2.2.3 Relevant standards for flammability tests on firewalls

Advisory Circular AC20-135 This document forms the core of the certification tests performed in cooperation between aircraft component manufacturers and the FAA. The problem statement and most of the considerations for the design of the burners as well as of the test rig used for the results presented here are inferred from this document (please cf. Ref. [37]) and described in Ch. 3. It defines the pilot flame temperature and how to measure it. Several thermocouples are installed within 0.25 in (6.35 mm) of the position where the sample will be located and their measurements are averaged. The heat flux density shall be $> 9.3\mathrm{BTU/ft^2{-}sec}$ ($105.6\,\mathrm{kW/m^2}$) and is measured using a calorimeter with an imposed geometry, termed the 'BTU heat transfer device'. A list of acceptable burners is provided in the referenced power plant engineering report No. 3A [46]. The main test configuration is shown systematically in Fig. 2.5.

From the definitions of fire resistance and fire proofness, structural static and dynamic loading shall be simulated as a function of the indented use and installation location. With respect to the intended use as firewall components and considering protective parasitic layers or coatings, additional test conditions should be considered:

- "Cool side" (backside) pressure including airflow and pressure, as during critical power operating conditions (500 ft/s (152 m/s) for 5 minutes as well as under windmilling conditions (70 ft/s (21 m/s) for 10 min.
- Critical differential pressure across fan exhaust ducts, which usually equals the take-off conditions at sea level.

scope of the work presented here and thus omitted in this definition.

[5] This apparatus is equivalent to the BTU heat transfer device described in Sec. 2.3 of $(116 \pm 10)\,\mathrm{kW/m^2}$.

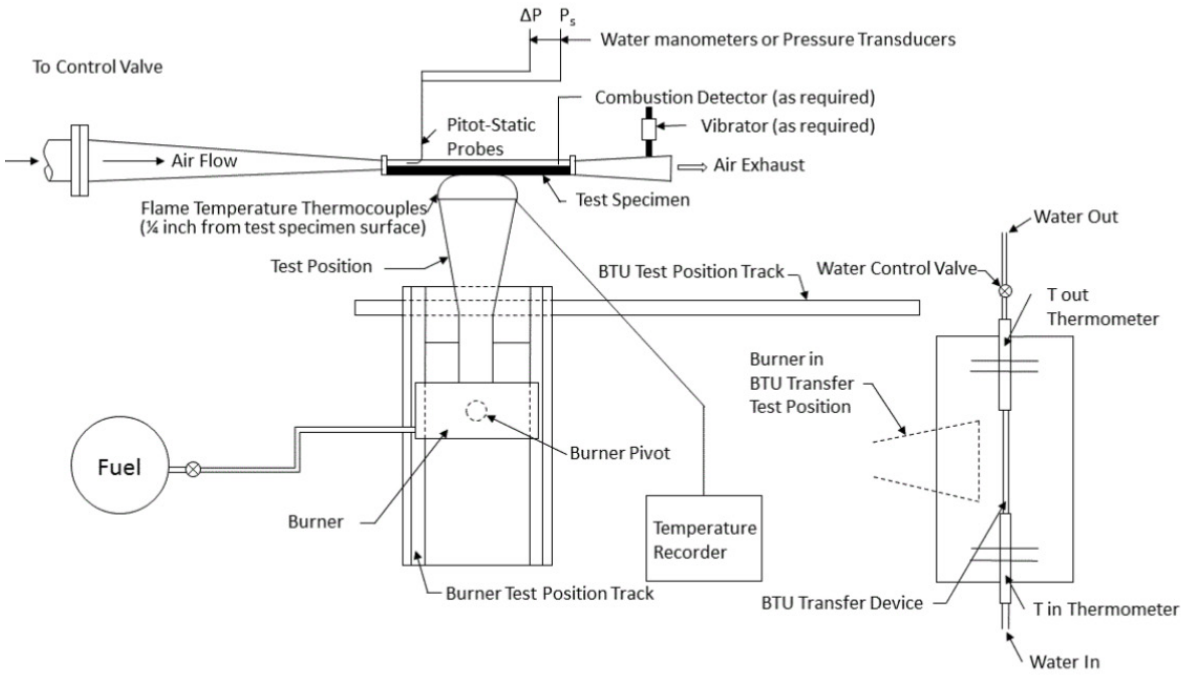

Figure 2.5 Test configuration, viewed from the top, for the evaluation of fireproof and fire-resistant firewalls. The calorimeter used for heat transfer measurements is positioned at the sample location during calibration. Image taken from [37] under public domain.

- All specimen with sprayed, painted-on or bonded-on protective coating intended to insulate the base material from fire conditions shall be vibrated in addition to be pressurized.

It has been shown that unprotected acoustic honeycomb specimens which fail this test usually ruptures due to loss of strength under pressure during the first few minutes, allowing air flow into the fire zone [37]. The main failing criteria according to AC20-135 are listed as: continuous burning of the sample, spread of flame pattern over the entire specimen, ignition of the backside, fire penetration, excessive out-gassing equivalent to ignition of the cool side, surface flare-up that is not self-extinguishing and self-reignition upon burner removal.

FAA Power plant engineering report No. 3 A This document (cf. Ref. [46]) is essentially an amendment to AC20-135 and specifies in more detail the experimental configurations for different components in the fire zones, with the help of photographs and schematics. It provides a description and technical drawings for building the BTU heat transfer device. This document also lists the allowed burner models and limits them to a few commercial-of-the-shelf (COTS) products. Since the test are usually performed in-house at the component manufacturer, acceptable modifications of these burners to obtained the required values specified by AC20-135 are discussed.

ISO2685:1998(E) ISO2685 (cf. Ref. [9]) is the international standard mandated outside the US for the fire safety certification of fire walls. It inherits in principle the majority of the procedures and requirements provided in AC20-135. Although reference is provided to AC20-135 and its amendments, the type of burner can be freely chosen by the operator as long as the flame characteristics generate a temperature of at least $(1100 \pm 80)\,°C$ and a heat flux density measured by the BTU transfer device of at least $(116 \pm 10)\,kW/m^2$. In contrast to AC20-135, the calibration of the burner is not deemed part of the test procedure. Moreover, ISO2685 states relative conditions between the sample surface area A and flame cross section B in the form of, $A \leq B$. Alternative equipment for the heat flux measurements is acceptable, but has to be calibrated with the BTU heat transfer device. For firewalls, the test conditions are extended by the requirements defined in Annex E: The firewalls shall be vibrated at an amplitude of 0.4 mm at a non-resonant frequency closest to 50 Hz [9].

2.3 Experimental techniques in flammability testing

The study of degradation mechanisms present in a sample that burns relies on the measurement of key physical quantities such as temperature, heat flux, mass loss or time-to-ignition. A compact summary of the relevant measurement techniques that are commonly used in fire tests and that are also implemented in the test rig built for the work presented here is given in the following. Because of its broad range of applications, these topics are extensively treated in the literature and thus this section is limited to framing the basic measurement principles. A brief discussion of potential challenges for applications in fire tests is given and the burners that are used to as pilot flame in large-scale tests are presented at the end of this section.

2.3.1 Temperature measurements

By far the most widely used sensors to measure temperature are thermocouples. A thermocouple can be seen as an electrical circuit, made up of two wires of different metals, that are joint at one end. A temperature difference between the junction point and the end of an individual wire will create a thermoelectric force (Seebeck effect), that is characteristic for the metal. Thermocouples fall into three groups: platinum-based (Type B, R, S), nickel-based (K, N) or constantan-based (Type E, J, T). Together they cover a temperature range from approximately −240 °C to 1720 °C [47]. For the most part in flammability tests, Type K thermocouples (Chromel-Alumel) are a common choice. They are recommended for oxidizing and inert atmospheres for temperature up to 1260 °C with an accuracy of ±5 °C at elevated temperatures. For temperatures up to 1768 °C encountered in flames, type R and S, both based on platinum, are used [48].

Challenges of temperature measurements in flames

When using thermocouples (TC), a difficulty to obtain an accurate temperature reading arises because the objective is to measure the temperature of a gas or solid surface but in fact the measure obtained is that of the hot junction of the thermocouple. These two temperatures are never the same, although the difference can sometimes be very small and can be minimized. The heat balance at the thermocouple junction includes contributions from the heat transfer to or from the junction by conduction through the wires, from the heat exchange by convection with the surrounding gas and from the heat input by radiation from the flame, hot surfaces or hot combustion gases. Additionally, contributions from catalytic exothermic reactions or radical recombination at the surface of the thermocouple and heat loss due to radiation must often be considered. The effects are schematically summarized in Fig. 2.6 and an excellent review of TC intended for flame measurements is given by Shaddix [49]. Commonly applied mitigation strategies for the dominant aforementioned effects are:

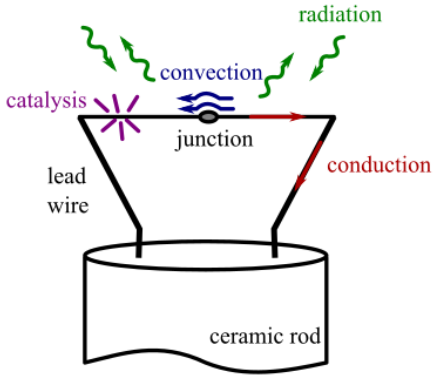

Figure 2.6 Typical thermocouple probe design for use in combustion system measurements. Image adapted from [49].

Conductive heating: The wires are run along an expected isotherm close to the junction. As platinum-based thermocouples suitable for high-temperature applications (type R and S) are expensive, this is commonly achieved by welding the TC to (thicker) lead wires as shown in Fig. 2.6. Alternatively the TC themselves can also be bent to into a triangular shape. This technique has been the main approach employed in the present work.

Catalytic heating and contamination: The TC wires and junction are coated to shield them from radicals and to prevent catalytic reactions. This is critically important for platinum-based thermocouples, for which flame temperature measurements can be overestimated by several hundred degrees when using uncoated probes [50, 51]. Deposition of a thin glass layer (silicon dioxide) was first proposed by Kaskan [52]. This approach was further developed by Kent [53], Burton [54] and Madson and Theby [55].

Net radiative heat transfer to the junction: Errors due to radiation may have a significant impact on the readings obtained. Jones has indicated that the errors for gas flame temperature

data in some cases may exceeded one hundred degrees [56–58]. Different strategies are developed to minimize this effect [59, 60] and NIST [6] recommends to use aspirated thermocouples at high aspiration velocities and double shielding to reduce radiation errors [7, 50, 51]. Additionally, simple radiation correction models can be used to post-treat data if the probe geometry is known [15]. For the thermocouples used in this work, this is the preferred approach as aspirated probes can perturb the flame [61] and more specifically, they are explicitly precluded for large-scale tests [37].

Convective heat exchange: For a given thermocouple size, the rate of convective heat transfer is primarily a function of the gas velocity at the junction. Depending on the location of the thermocouple, it may experience gas flows up to a few meters per second in the buoyant flows of flames or fire plumes [7]. The convection coefficient can be calculated from correlations, of which several are available [50, 51, 59, 62]. The values obtained are then used to correct the measurement for the effective (average) temperature. However, this is only relevant for transient measurement, when the time constant of the temperature change is very small and in the order of the exposure time of the thermocouple in the hot flow of gas. For the results presented here, the measurements can be considered at steady state.

Another type of temperature sensors used in flammability testing are resistance temperature detectors (RTD), that make use of the property that all metals respond with an increase in electrical resistance when heated [63]. Because of its chemical and thermal stability, RTD are commonly made of platinum alloys.

2.3.2 Heat flux measurement

The fire testing of firewalls requires the use of a custom calorimeter, the so-called BTU heat transfer device[7] [9, 37, 46]. It is based on a copper tube, as shown in Fig. 2.7, through which water flows at constant temperature and velocity. The concept of this apparatus is heat flow calorimetry: the heat transfer from the flame to a well-defined section of the copper tube is determined from the raise in temperature measured in the water flowing through that section. According to AC20-13 [37] and the power plant engineering report 3A [46], the target value is 9.3 $\mathrm{BTU/ft^2-sec}$ (105.6 $\mathrm{kW/m^2}$) or 4500 BTU/hr (1.3 kW)[8]. The water temperature is required to be within 10 °C to 21 °C (50 °F to 70 °F) and supplied at a constant flow rate of 3.8 L/h = 228 L/min (500 lb/h = 1 gal/min). The

[6] National Institute of Standards and Technology (NIST)

[7] The denomination of this device is neither uniform within the standards nor across related documents. Other common names are: continuous flow calorimeter, B.T.U. heat transfer device, burner standardization apparatus, as well as variants of these terms.

[8] British thermal unit. 1000 BTU/h is approximately 273 W.

average difference in temperature in [°F] of the inlet and outlet water multiplied by the flow rate equals the rate of BTU increase of the water running through the device. This value indicates the severity of the portion of the flame in which the center tube is immersed. The energy balance on the water can be expressed as:

$$\dot{Q} = A(T - T_0) \quad \rightarrow \quad \dot{Q} = \frac{\dot{q}_v \rho c_p}{c_{\mathrm{SI}} L}(T - T_0) \tag{2.1}$$

with Q, the heat transfer to the calorimeter, A a constant of the apparatus, T the temperature at the exit of the measurement section and T_0 the temperature of water at the entrance of the copper tube. The apparatus constant A depends on the geometry, the conductivity of the materials through which the heat passes, and their surface condition. For a given setup, the apparatus constant is formed by $\dot{q}_v$, the water volume flow rate through the copper tube, ρ, the density and c_p, the specific heat of water and the length L of the tube exposed to the flame. An additional factor, c_{SI}, in the denominator might be used to convert from the imperial unit system, as used in all FAA regulations, to the SI unit system. The calibration procedure foresees a warm-up period of 3 min before the large-scale burner is pointed on the BTU heat transfer device. The temperature is required to be recorded only every 30 s over a period of 3 min. The corresponding ISO2685 maintains the same procedure but specifies that the BTU device shall not be exposed to the flame during the warm-up period. It is worth noting that the FAA advisory circular also allows for COTS calorimeter rated for 0 $\mathrm{BTU/ft^2-sec}$ to 15 $\mathrm{BTU/ft^2-sec}$ (0 $\mathrm{kW/cm^2}$ to 17 $\mathrm{kW/cm^2}$), accurate to ±3 %.

Challenges of heat flux measurements in flames

Although the BTU heat transfer device is easy to built and at first look easy to use, its apparent simplicity is impaired by two factors that significantly decrease the measurement accuracy. First, the length exposed to and 'fully engulfed' by the flame [46] leaves room for interpretation. Eq. (2.1) assumes that the tube experiences a homogeneous heat flux around its circumference and L is the corresponding length of this engulfed surface. The flame diameters reported in the standard documents [9, 37, 46], but also in research [64–66] are smaller then the length of the tube and vary as a function of the burner operating parameters. As a consequence, measurements are hard to repeat and depend on the tube length assumed to be engulfed in the flame. Secondly, as the burners are not operated for optimal combustion but rather to resemble a fire hazard, their flames are sooty and the developing soot layer during calibration leads to decreasing values for the heat flux density even if the burner output remains constant.

Outside fire resistance certification testing, the instrumentation to measure heat flux in fire tests is mostly based on Gardon or Schmidt-Boelter gauges [7]. Both devices commonly feature a cylin-

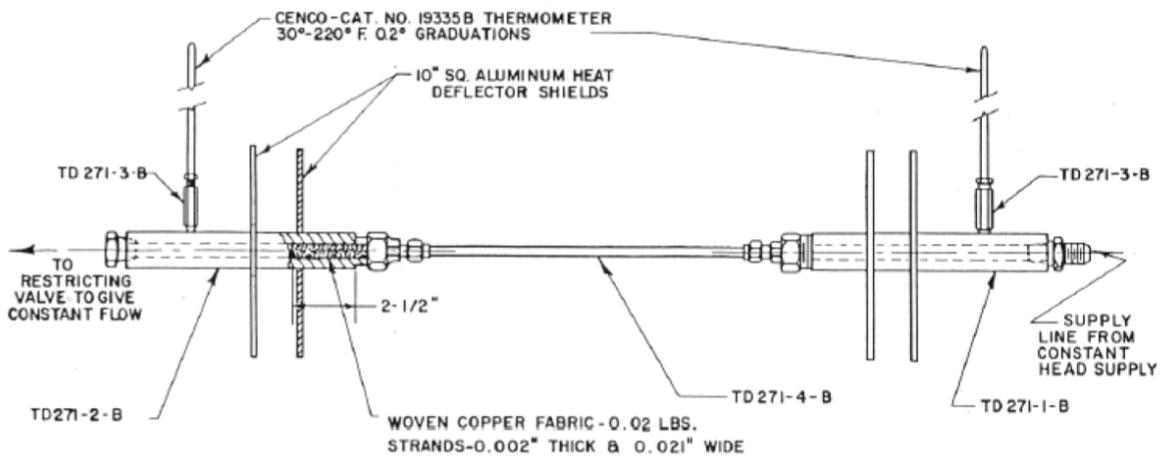

Figure 2.7 Technical drawing for a calorimeter (BTU heat transfer device) as suggested by the FAA, from [37] under public domain.

drically shaped cooled body and a black coated sensor that faces the heat source. In the case of a Gardon gauge, a differential thermocouple is connected to the thin sensor foil and the cooled metal body. The incoming heat flux yields a proportional electromotive force (emf) that is measured. In the case of a Schmidt-Boelter gauge, the sensor is connected through a multi-junction thermopile to a surface underneath. The emf in this case is proportional to the heat transferred normal to the surface [67]. Blanchat [68] compares both sensor to alternative gauges for high temperature environment which do not require water cooling. Subjected to heat flux pulse tests, the agreement at the highest heat flux level was within approximately 5 percent between the sensor and increased to 22 % when the the heat flux was step-wise increased. The decrease in agreement is directly linked to higher variance for one of the alternative gauges. Pitts et al. [69] presents a detailed round-robin study for these gauges in the context of fire testing performed at five different test facilities. Despite different calibration protocols, the agreement is deemed satisfactory and the differences between results were attributed to the differences in gauge sensitivity towards convective heat transfer contributions. Because of the extremely harsh experimental conditions, these sensor require regular calibration, with Gifford [70] and Purpura [71] presenting methods suitable for sensor verification.

2.3.3 Large-scale burner

The fire tests listed in Sec. 2.2.3 require a heat source, i.e. a flame, to ignite the sample. The device that generates this pilot flame is a burner; it brings fuel and oxidizer into contact and initiates the combustion. The oxidizer and the fuel can be supplied separately and mixed only at the burner exit, or they can be mixed before exiting (premixed burner) by a directly integrated or external

mixing unit. The oxidizer can be either cold air (as in most cases), preheated air, pure oxygen or air enriched with oxygen. Compared to liquid-fuelled burners, a propane burner is easier to control, less complex in terms of design, but also less representative of the fire hazard in the airplane compared to a kerosene flame. However, in the context of research and with the aim to study chemical and physical processes on a more fundamental level, a propane burner is of great interest. A propane burner is thus an ideal complement to study the thermal degradation of the samples without the complexity and unknowns introduced by an oil burner.

Since a change to the applicable standard in 2018 [37], gas burners are no longer permitted for certification testing and instead oil (kerosene) burners have to be used. Despite the variety of available designs, tailored to specific fuel and applications, most oil burner concepts can be reduced to the main components shown in Fig. 2.8. To obtain a combustible fuel-oxidizer mixture, the liquid fuel has to be atomized. The nozzle designs determines the droplet size, distribution and pattern of the exiting oil spray. The air is supplied separately and a turbulator (stator) positioned before the burner exit plane introduces turbulent and rotational motion so that the air stream enters the fuel mist. A good mixture between the reactants of different phases is harder to achieve than for only gaseous species. As a result, unburnt fuel droplets can exit the burner, reducing combustion efficiency. This is a concern if one wishes to improve the burner efficiency, but in the context of firewall testing an inefficient liquid-fuelled burner better represents the fire hazard configuration, where a fuel-carrying line is assumed to leak and ignite. One could expect that in such a scenario the resulting flame is unclean and has little in common with an efficient burner flame, with scattered unburnt droplets creating an even more demanding situation for the firewall.

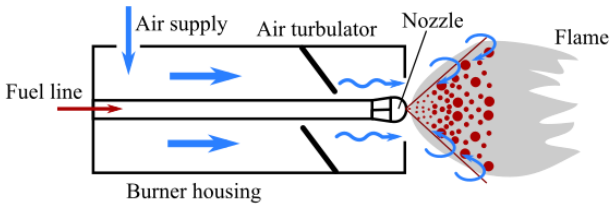

Figure 2.8 Oil burner operation and basic components: fuel and oxidizer supply, turbulator and nozzle determine the flame chemistry and shape.

AC20-135 as well as ISO2685 provide only suggestions for the burners and the list borrows partly from an evaluation of burner characteristics dating from the nineteen seventies [72]. Although AC20-135 has been revised in 2018 and mentions that "miscellaneous kerosene-based burners" have been approved by FAA, the fire testing community still strongly adheres to the original list of applicable oil burners that has not been updated since 1990, with some of the compliant burners now being out of production [73]. With the release of a new fire safety requirement for acoustic/thermal insulation in 2003, it was discovered that one the predominantly used burner, the Park DPL3400 burner, was not produced anymore. Additionally, the Park burners in circulation vary in design despite

identical model numbers [73]. The FAA is addressing the issue and started developing a suitable burner that borrows from the PARK DPL3400 and is made of readily available components. This burner is developed within the NextGen Program of the FAA and thus commonly referred to as the NextGen burner. The FAA task group in charge of this effort has aimed from the beginning to develop a burner that can be used for several fire tests outside the fuselage and is hence also expected to be included in a coming update of the Advisory Circular AC20-135. A detailed experimental study of the NextGen burner is provided by Kao [64,74]. The original Park burner and the NextGen burner are shown in Fig. 2.9. It is important to note the the Nextgen burner tube is essentially the same as for the Park burner. What is significantly different is that it does not draw air from the environment but instead the air is supplied from a compressor.

2.4 State of the art for fundamental investigation at reduced scale

The development of new composite material systems often imposes constrains accounting for fire safety, in addition to application-specific requirements. As a consequence a lot of non-standardized tests and ad-hoc experiments are well documented to investigate their properties under heat and flame, to support the development process upstream of component certification. Although the focus of this work lies with aviation and aerospace applications, the fire behavior of composite panels is of high interest for other safety-critical applications, for instance in marine engineering [75] or hydrogen storage [76]. The experimental configurations used range from simple heat or flame exposure to combined thermal and mechanical load to post-exposure investigation of residual properties.

Small-scale tests used to expose composite materials to heat or flame falling outside the range of standardized tests described above can be roughly divided based on the chosen test equipment. The first group relies on existing standard test apparatus, for instance the cone calorimeter described in ASTM E-906 [77], the oxygen consumption calorimeter defined in ASTM E 1354 [40] or the Ohio State University (OSU) Rate of Heat Release Apparatus [78, 79]. In a cone calorimeter, sample coupons are exposed to radiant heat flux up to $100\,\mathrm{kW/m^2}$ until they self-ignite, with piloted ignition also possible. This instrument is widely used to assess polymeric material fire properties based on the measurement of heat release rates [80–83], as for example for thermoplastics [84] or for glass and carbon fibre reinforced composites [85–87]. Detailed investigations on the interaction between heat flux and fibre orientation [86] on the degradation of composites and more specifically on the fibre oxidation [88] has also been performed with cone calorimetry [89]. The sample sizes are usually smaller than 200 mm on their longest side. It is important to note that although radiant heat sources do not result in the same degradation mechanisms as flames, many of the numerical models for flame exposure are based on a transient thermal model, a concept initially validated

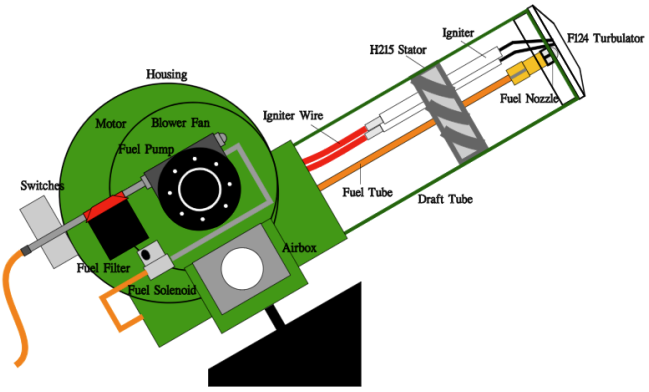

(a)

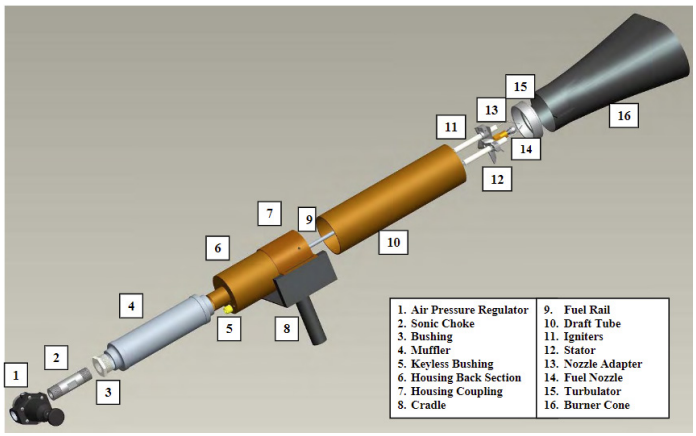

(b)

Figure 2.9 (a) Park DPL 3400 burner assembly and (b) exploded view of the NextGen burner, from [73] under Public Domain.

using a radiant heat source [90], with an nth order approximation for the rate of decomposition, the Henderson equation [91].

Standardized thermal loads are commonly also applied by exposure to either IMO A.754(18) or UL 1709 flames [19]. These standardized and commercially available small-scale test beds and test procedures are widely used in research and industry. The IMO A.754 is a test configuration for fire testing of fastening and insulating materials for marine applications; the UL 1709 describes a test method for measuring the resistance of protective materials to rapid-temperature-rise fires. Scientific research using such standard flames and commercial test beds benefits from the simplification of comparing results with other fire research groups. Gas torches are another common and simple tool to use as pilot during fire testing. In the field of composite materials for naval and off-shore applications, tests typically expose the entire sample to harsh fire conditions in a furnace heated

with a methane burner [92, 93]. In the majority of cases some kind of propane burner is used in small-scale fire testing. Halm [94] and Birman [95] test composite materials intended for hydrogen vessel construction with a very simple experimental configuration and use the data also for model validation.

Mouritz, Browne, Feih from the RMIT University in Australia and Gibson and Browne from the University of Newcastle UK, have created a well-linked research network that is centred around the fire properties of polymer-based composites [81, 96–99]. An important output of this collaboration are experimental equipment and techniques for small-scale fire tests. Their use of a COTS propane torch intended for forging and plumbing has contributed to the widespread introduction of this particular cup-shaped burner for similar research. More specifically, the very same gas burner model has been implemented in the small-scale bench from Tranchard [100], Hörold [22] and more recently by Chazelle and Schuhler [101] and Tabaka [102], all aimed at investigating the fire properties of composite materials.

Rather than attempting to measure the mechanical properties of burning composites in-situ, the residual structural integrity is commonly assessed through post-fire analysis. The evolution over time of the properties is then obtained by mechanically testing samples that have been quenched at given test conditions to conserve their state. Experimental data is widely available for tensile and compressive strenght after fire-exposure [83, 87, 93, 103–108]. The topic has also been review in a general manner by Mouritz and Gibson [91, 99] and specifically for marine applications [97, 109–111]. Tests under combined load and heat have also been reported, where the heat exposure is usually limited to one of the sample surfaces, for instance by a cartridge heater included in a metal support which prevents buckling [80, 112]. Simultaneous testing under tension using a radiant heat source has been published by Swanson and Wolfrum [113] to analyze trends in the time to failure of CFRP (carbon fibre reinforced plastics). Their findings confirm that high simultaneous mechanical and thermal load reduce the time to failure, but also identified a critical loading scenario at which the material life could be extended solely by reducing the mechanical load. Luo et al. [114] used a numerical approach to describe the delamination and time-to-failure of polymer sandwich panels exposed to one sided heat flux. Results are in good agreement with experimental data made available by Feih [115] on compressive loaded sandwich specimen.

To the best of the author's knowledge, only three small-scale test benches for fire testing have reported the usage of a kerosene burner. Sánchez-Carballido [116] and Melendez [117] both use the same COTS diesel burner equipped with a 80° spray nozzle to achieve certification-like conditions. However they neither report how or if the flame was calibrated nor values for the heat flux density or flame temperature. A second fire testing setup using a small-scale oil burner was presented by Schuhler [118], indicating only the supplier (Cuenod), but not the model. Their burner was also

modified with an 80° nozzle, which is likely inspired by the Monarch 5.5 gph 80° PL F-80 nozzle used in the large-scale Parker burner and the Sonic (NextGen) burner. All large-scale oil burners are equipped with a cone as prescribed by the FAA Aircraft Materials Fire Test Handbook, chapter 24 [45]. The Cuenod burner used by Schuhler has thus been modified with a flame tube (50 mm in diameter) to restrain the flame diameter and damp the turbulence. The heat flux range of this burner is 80 kW to 180 kW. The third kerosene setup was initially developed for the work presented here by Béland [119]. The original burner hardware design and particularly the control interface have been significantly improved since then and are detailed in Ch. 3.

Very few experimental investigations have attempted to fully recreate the conditions of the AC20-135 and ISO2685 certification standards in terms of a rigorous assessment through advanced diagnostics of the many factors influencing both heat flux density and flame temperature. The only two found in the literature are the experimental test bed from Tranchard [100] that includes in-situ mass loss assessment, infrared (IR) pyrometry and gas analysis via FTIR[9]. By default a propane torch is used, but their rig is compatible with the FAA NexGenburner [74]. The setup from Schuhler [118] also provides a continuous residual mass profile and complements thermocouple measurements with IR thermography. Other testing considerations addressing mechanical tests through vibration or load are not implemented.

2.5 Infrared thermography as tool in fire testing

Pyrometry is a contact-less method to measure the surface temperature of a solid sample, based on the electromagnetic radiation emitted by heated matter. Since the spectral range of this radiation lies in the infrared (IR), it is called IR pyrometry, a technique that can either be implemented point-wise or through the use of IR cameras (thermography). In conventional IR thermography, assuming that the emissivity of the surface is known as well as the viewing distance and angle to the target surface, Stefan-Boltzmann's law can be used to calculate the average temperature of the target area [63, 120]. However, in practical applications of IR thermography, careful calibration and image post-processing are essential to obtain quantitative results with reasonnable and known errors on temperature values.

Many of the small-scale fire test rigs discussed above have been complemented with IR thermography measurements. Tranchard [100] presents IR mappings from the rear face of exposed samples but the images have only qualitative character as no values are reported. Schuhler uses an IR camera with a sensor sensitive in the range from 7.5 µm to 13 µm equipped with a (non-specified) filter that is stated to be suitable for measurements from 100 °C to 500 °C in [118] and from 100 °C to 600 °C

[9] Fourier-transform infrared spectroscopy (FTIR) is a spectroscopy method to obtain emission and absorption spectra of a phase by Fourier transformation. A wide spectral range is covered simultaneously at high spectral resolution.

in [121]. Seggewiss [122] uses IR imaging in a similar manner, with emissivity values measured from pristine samples prior to testing. Both Tranchard and Schuhler assume a constant emissivity value obtained from the literature to evaluate their IR data, based on similar approaches applied for model development [23, 90, 123]. However, measurements from Neuer [124, 125] clearly demonstrate that the emissivity of carbon/fibre composites varies with temperature and wavelength and thus needs to be considered for pyrometric measurements. Guilhem [126] proposes that the emissivity accuracy for single color thermography should be always better than 10 %.

Several research groups have attempted to improve the accuracy of IR thermography of thermally degrading composite materials. Acem [127] uses IR imaging to investigate the surface temperature of carbon fibre composites during cone calorimetry tests, under a heat flux ranging from 20 kW/m^2 to 65 kW/m^2. Reflective contributions from the calorimeter heating coil are addressed during post-processing and the increase in thermal radiation is linked to a temperature rise. A filter is used to block contributions from flame arising when the sample ignites and the changing emissivity is measured in parallel via FTIR. Mendelez and Sanchez [116, 117, 128] address the challenge of IR measurements on the sample side that is subjected to the flame and suggest a post processing approach that reduces the pilot flame contribution. The unknown emissivity of the sample is obtained by placing paint marks of known emissivity on the sample and comparing it against the unknown emissivity in the neighbouring area that is assumed to be at the same temperature.

In the test configurations discussed above, the knowledge of the sample emissivity remains the biggest challenge when using conventional IR thermography for accurate temperature measurements. A material's emissivity does not only have spectral and temperature dependencies but is also greatly affected by the surface properties themselves. Seggewiss [122] identified a difference of 12.7 % in the total emissivity of composite samples that have been prepared with rough and smooth fabric plies. Adibekyan [129] presented data on the change in emissivity for glass and carbon fibre reinforced plastics in the spectral range from 1 µm to 16.7 µm. Jones et al. [130] reported an extensive compilation of emissivity data at high temperatures for various materials. These investigations clearly reveal that as composite material undergoes fast changes in temperature, and consequently as the spectral content of their radiative emission changes, surface morphology and emissivity also changes. This demonstrates that the use of a fixed emissivity value, especially if it is obtained on pristine samples at room temperature, greatly reduces the accuracy of conventional IR thermography for composites degrading under fire exposure.

A solution to this problem exists through the implementation of a more complex technique based on electromagnetic radiation: two-color thermography. It allows the measurement of the surface temperature without knowledge of its emissivity. To this end it is necessary to measure the same scene through two different and narrow band-pass filters. The main assumptions is that the emis-

sivity can be considered constant in the spectral range of the two filters. The object temperature is then obtained from the ratio of the two signal measured. An excellent general introduction to the topic is provided by Möllman and Vollmer [131], whereas the application towards fire testing is too specific to be covered. Reggeti [132] proposes an experimental camera and filter setup to minimize error due to optical path differences and parallax for flame measurements. However, the measurements are performed using the color channels from a consumer grade optical camera and externally mounted optical density filters to reduce the radiance signal. In a detailed review by Savino [133] on the two-color technique from a practical standpoint, he underlines that in the case of external filters additional signal contributions from the surrounding need to be considered in the radiation transfer model. Although the two-color technique comes with its own challenges, the measurement principle is a very promising way to measure the surface temperature of thermally degrading materials with good accuracy.

2.6 Critical assessment of the state of the art

The assessment of the fire properties of composite materials is of general interest in many fields of research and technology. A large part of fire research is however limited to direct industrial application and the demand of compliance with regulations. In the aerospace sector, the corresponding *ad-hoc* fire tests were designed with the goal to ensure easy implementation by aircraft component manufacturers, which usually performs these tests on their own premises in cooperation with the FAA. The very reduced set of parameters controlled and measured in such tests is a consequence of this aim as well. Focusing on certification fire tests for composite materials in aircraft firewalls (cf. Sec. 2.4), the limited information obtained from these tests is in stark contrast with the large amount of time and effort that is consumed.

Furthermore, some of the assumptions that the test procedures are based on may not be justified or may not account for important effects. For instance, the heat flux measurement is at the heart of these fire tests, yet the instrumentation used is rudimentary, explaining why this topic is prone to confusions and misinterpretations [134]. The water calorimeter, also known as the BTU heat transfer device, is the key tool to calibrate the burner [46]. From Eq. (2.1) it is apparent that any uncertainty in the knowledge of the apparatus constant lead to errors in the heat transfer measured.

This apparatus constant is very sensitive to the surface condition of the calorimeter as the certification tests are performed with a kerosene burner, soot is accumulating on the copper tube, altering the capacity of the tube to transfer heat to the water. Although the issue is briefly mentioned as remark in the test procedure, the mitigation actions are limited to an initial cleaning before each test run [46]. The heat flux transferred to the sample is the dominant factor that triggers thermal degradation. An erroneous understanding of this variable significantly affects all efforts to relate physical

and chemical processes with the structural integrity of the sample. It is somewhat surprising that the discussion of the heat flux measurement is unfortunately often very spares when experimental data from scientific fire experiments is presented. This is remarkable because the general topic of heat flux measurement is researched quite actively [78, 135, 136].

The inherent rigidity of test standards also prevents adapting the test procedure to different burner types. The regulations in place currently still propose a list of outdated oil burners. The kerosene burner has a significantly different combustion behavior as a gas burner with respect to flame chemistry, flame stability and heat transfer.

By contrast to the current practice in certification testing, there is an active research community who investigates fire properties on a fundamental level [91, 112, 137]. In this field, detailed knowledge of the experimental conditions is rightfully recognized as essential to the understanding of the mechanisms at play. However, it is still very common, as has been shown in Sec. 2.4, to replace the flame as a fire hazard from flammable liquid leaks with a radiant heat source [113] or a less aggressive propane burner [91, 100–102]. And even when a propane burner is used, the diagnostics usually do not involve advanced techniques but temperature and heat flux measurements [114, 115]. The heat flux distribution is also often assumed to be constant over the test period and homogeneous in its distribution, but validation of this hypothesis is often omitted. It has been demonstrated that the heat transfer to a surface is strongly variable in space with and without flame impingement [138–141], and this factor is neglected in many experiments. Two small-scale test setups use commercially available oil-burners, but the claim that these burners are 'small-scale' could be argued as their output power is similar to large scale burners (approx. 85 kW) [73, 142]. This issue is addressed in this work through objective #1, with the results being presented in Ch. 4.

> *Objective #1*
> A true small-scale oil burner is calibrated to obtain the nominal conditions required for fire testing according to AC 20-135 [37] and ISO 2685 [9] with an overall thermal power reduced by two thirds when compared to a large-scale burner. The final flame volume and diameter are reduced accordingly, allowing minimize specimen area to a fifth of the area used in certification tests, paving the way for screening tests on a coupon level. The flame calibration is based on temperature and heat flux measurements, with the raw data being corrected to reduce error contributions.

IR imaging has been used in small-scale fire tests on composites [100, 118, 122] to complement spatially-limited probes with 2D temperature maps, but the test rigs described above rely on implementations of conventional IR thermography, which requires prior knowledge of the sample emissivity. Although contributions from the pilot flame [128] and background reflections [127] are addressed in some works, the common approach is to assume that the emissivity of the un-

burnt sample can be used over the entire spectral and temperature range during fire exposure. This research need is addressed in this thesis through objective #2, with the results presented in Ch. 5.

> *Objective #2*
> Sample backside temperature and emissivity measurements during the thermal degradation of a composite sample provide valuable insides and allow not only to link the incident heat flux to time-to-ignition or the onset of pyrolysis but even more, represent key material parameters that can contribute to improve numerical predictive models.

The availability of the research tools developed through the first two objectives of this work enables the investigation of a key research need in the fire research community, namely the effect of the flame characteristics on the degradation rate of the mechanical properties of composites exposed to flames. The study of combined load-fire testing is restricted to a few groups worldwide, with studies of compressive load prevailing. Modelling of the structural response to fire of composites is more challenging because the softening and failure of both the fibres and the resin have to be taken into account [91]. Less literature is available for experimental study on the thermal degradation of tensile properties of composite materials than for compressive properties [80, 143]. While the available experimental equipment has certainly evolved over time, all test configurations rely on several assumptions and on a limited set of measured values that are continuously recorded over the test period. The merit of these assumptions and the limitations of the experimental data is seldom discussed, for instance on a potential interplay between sample size and flame size [144].

The combination of advanced diagnostics and standard methods to obtain time- and spatially-resolved information of surface temperature, emissivity evolution, and residual mass paves the way for addressing the interplay between physical and chemical processes during flame attacks on composites. The availability of such experimental datasets could also enable the validation of advanced numerical models, that already provide some predictive capabilities and are in continuous development. Currently available data are either not freely available, not well documented, rely only on radiative heat sources [90] or gas burner [100, 122, 145]. Finally, Objective #3 devotes our efforts to this unmet research need, with the results presented and discussed in Ch. 6.

> *Objective #3*
> With the majority of scientific bench-scale tests relying on propane torches, it is crucial to compare the specimen degradation against a small-kerosene flame. Effects such as flame momentum, presence of reactive species, flame chemistry, flow dynamics do all influence the severity and extent of thermal damage and need to acknowledged. Using the outcome of the previous two objectives, the specimen residual properties can be investigated for gas and oil flames with nominal same heat flux density and flame temperature.

The general objective of this work is to contribute to an improved understanding of the fire degradation behaviour of CFRP. The work was divided in sub-objectives to address current shortcomings in the design and experimental methodology of conventional fire resistance testing. Although the outcomes of objectives #1 and #2 contribute to the general goal, both are rooted in different research domains and hence can be treated to a certain degree independently. Objective #3 builds on these results, but really dives into the material degradation. It was thus decided to organize the thesis as a collection of three autonomous publications (*thèse par articles*) which have been submitted to peer reviewed journals.

CHAPTER 3 EXPERIMENTAL METHODOLOGY

The objectives tackled in this work required the development and fabrication of unique experimental facilities that enabled composite coupons to be exposed to precisely controlled flame attacks, while allowing detailed measurements of the thermal degradation process. The requirements for these hardware developments are as follows :

- The heat sources implemented should be representative of flame attacks conditions as prescribed in certification tests, i.e. gas and kerosene burners.
- The experiments should be conducted at the bench-scale, to enable the implementation of advanced diagnostics, and should allow for fire to be impinged on samples under tensile load.
- Advanced diagnostic tools should be implemented in the test section to monitor key parameters characterizing the material degradation rate, such as the surface temperature and the mass loss.

This chapter covers the experimental developments that could not be included in the research articles presented in the following three chapters for the sake of concision.

3.1 Reactive heat sources for small-scale fire testing

The conception of the experimental infrastructure involved inputs from the industrial partners and the NRC fire laboratory, to define the main dimensional and mechanical requirements from their vast experience in fire testing. It was decided early to consider two tailored heat sources. A propane burner allows to study the thermal degradation of the samples using simple experimental means and to reproduce tests from other research groups. The reduced experimental complexity is also beneficial for numerical model validation. In parallel, a kerosene burner was designed and built at Université Laval to be more representative of the fire hazards considered in certification standards and encountered in real emergency scenarios [146]. This "Mark I" burner was then substantially modified to enhance burner control, flame stability and safety of operation (Mark II). The compatibility of mounting solutions and accessory equipment between burners ensured that both can be installed interchangeably in the test rig. It is important to note, that since the sample and test rig are bench-scale versions of the actual certification tests, both burners are down-scaled accordingly. These experimental burners are thus not intended to be used in large-scale tests. Details on the

scaling methodology for the original design of the burner are presented by Béland [146] and for the calibration equipment in Ch. 4. Although both burner concepts aim to achieve the key values from the standards in terms of temperature and heat flux, they are also designed to go below and beyond these values, therefore enabling research on the effect of these critical parameters.

3.1.1 Gas burner

An air-aspirated gas blow torch, typically used for forging and roofing applications, was chosen to generate the propane flames. The specifications of the two models acquired are listed in Tab. 3.1, for torches burning propane at 1 bar. This choice was motivated by the use of the same torches in other small-scale fire testing studies available in the literature [21, 100, 112], allowing comparison with the results of other research groups. Two torch models with different cone diameter were used with two copies of each model procured. Due to the fuel injection design of these torches, no flashback arrestors are required, simplifying their handling and implementation.

In early experiments, it appeared that the temperature of the torches metal cone influences the measured heat flux when operated for a typical test time of fifteen minutes. The results were consistent with the findings from Tranchard [100] and Kao [64]. A copper coil was thus welded to the cone outer surface of the Bullfinch 1270 torch to control its temperature, by circulating thermostat-controlled (Julabo, Corio CD) water in the coil (Fig. 3.1). The flow rate of the refrigerated circulator is automatically regulated to maintain a constant water temperature of 21 °C (approximately 16 L/min). The heat flux experienced by the sample from the gas torch depends mainly on the reactants (air and fuel) flow rate and temperature, as well as on the temperature of the cooling water flowing around the burner. The water temperature was set to room temperature (21 °C) to limit condensation within the burner. For the results included in this work, the heat flux value was calibrated following the procedure described in Ch. 6, essentially by adjusting the fuel flow rate (burner thermal power, using a Omega FMA5444 mass flow controller) and the distance between the burner and the sample. For our tests, two different flames were calibrated. The first used the parameters reported by Tranchard [100]: a fuel flow rate of 7 slpm and a 75 mm horizontal distance between the tip of the burner and the sample surface. In a second configuration, the distance to sample was increased to 185 mm, and the propane fuel was mixed with 10 % CO_2 (99.99 % purity), with the mixture supplied at 9 slpm. Both flames complied with the requirements in ISO2685 and AC20-135 in terms of flame temperature and heat flux. An in-depth analysis of these two flame configurations is presented in Ch. 6.

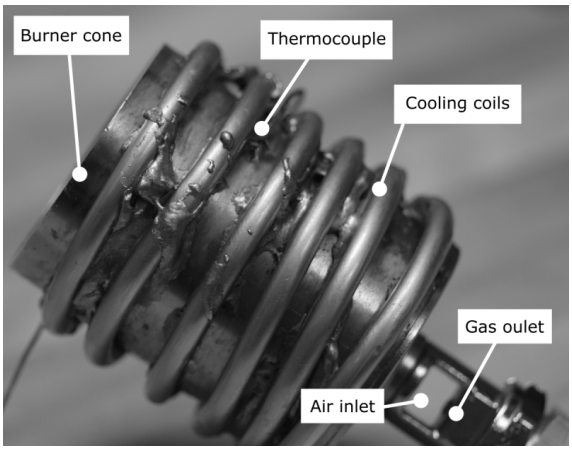

Figure 3.1 Photograph of the gas torch used to create propane flames, with cooling coil welded to its outer surface to improve stability.

3.1.2 Kerosene burner

The first iteration of the small-scale burner ("miniK") has been previously presented by Béland [146], together with a first set of calibration measurements and CFD simulations. This Mark I version, once transferred to our research group has been significantly improved and modified into what will be henceforth referred to as the "Mark II" version of the miniK to improve flame stability and operationnal safety. The general burner layout is shown in Fig. 3.2, as illustrated in the burner control software program.

The fuel is pumped from a reservoir resting on an analytical scale (VWR, P2 series F2-5KG) to the burner nozzle entrance controlled with an normally closed (N/C) solenoid valve. An additional circuit back to the reservoir prevents pressure buildup in case the pump is running while the inlet solenoid valve remains closed. During burner operation, this circuit is closed to preserve the main inlet pressure to the nozzle feed, with a pressure release valve (PRV) implemented as safety precaution. The fuel that is not atomized, i.e. excess fuel, also flows back to the reservoir. The fuel consumption rate is calculated using the mass of the fuel reservoir measured by the scale, corresponding to the difference between the out-flowing and returning flow rates. Air is supplied

Table 3.1 Bullfinch gas blow torch specifications. The power and gas consumption are rated for burning propane at 1 bar. Both torch models comply with EN 9012:2011.

Burner No.	Power [kW]	Flowrate [g/h]	Burner dim. [mm]	Flame dim. [mm]
1260	19.6	1420	110 x 48	L 350 x W 62
1270	32.5	2340	120 x 63	L 420 x W 74

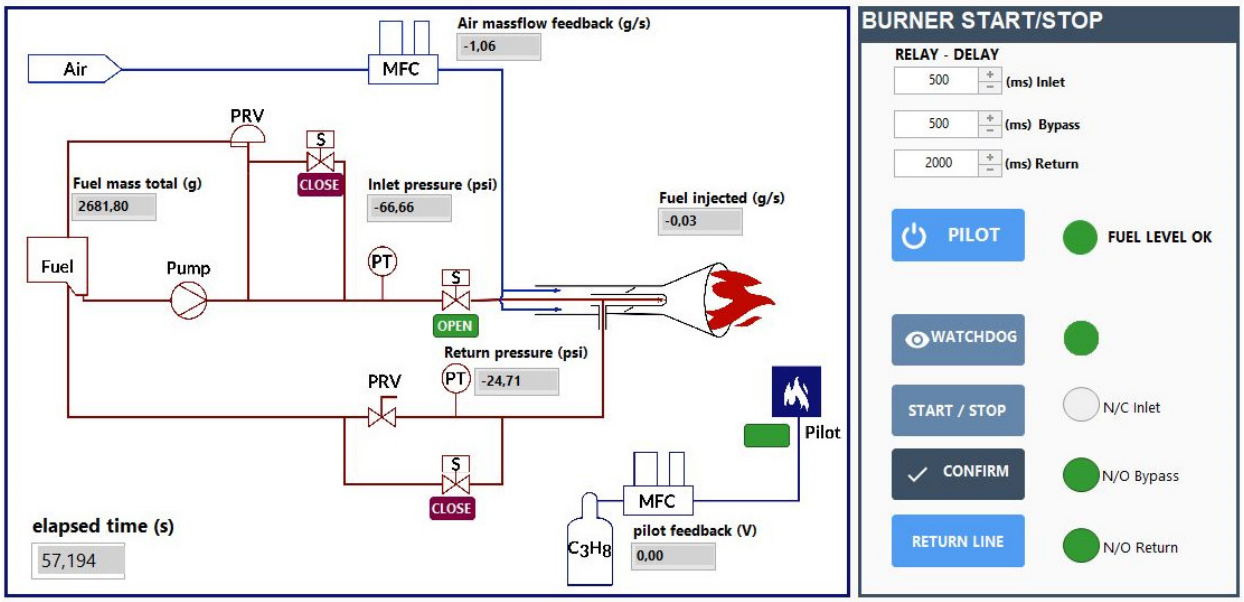

Figure 3.2 Schematic representation of the miniK kerosene burner hardware layout, as illustrated in the control software, showing the interface during start up. The indicators in the left correspond to the valve state.

from the laboratory compressed air system and controlled with a mass flow controller (Omega, FMA5444). This ensures that the air is at room temperature (21 °C) and dehumidified, which allows for a better repeatability and independence of the ambient conditions, contrary to the situation encountered for the Park or Carlin burners. The fuel is ignited with a propane pilot burner generating a flame sheet (Fig. 3.3), ensuring that no unburned fuel droplets can escape into the testing chamber prior to ignition.

One major challenge in the development of a scaled-down version of a liquid-fuel pilot burner capable of delivering the same heat flux density as the Sonic (NextGen) or Park burners, is the low fuel flow rates required. To put things into perspective, the nozzle used in large-scale testing facilities is typically a Monarch nozzle rated for 5.5 GPH with an opening angle of 80°. Based on the scaling calculations from Béland [146], less than approximately 1.5 GPH is needed for the scale of experiment planned in our work. Operating a pressure-driven nozzle outside of its specifications to obtain lower flow rates will also alter the spray pattern and decrease the atomization efficiency. Bypass nozzles have thus been selected to achieve low flow rates while maintaining an input pressure of 20.7 bar (300 psi). Originally only a Delavan nozzle rated for 0.75 GPH with a spray angle of 60° was selected but later additional bypass nozzles from Monarch rated at 1.5 GPH with different opening angles 30°, 45° and 60° were tested. The Monarch nozzle head is completely made of steel and is easy to clean. The Delavan nozzle has a small groove around the nozzle hole which promotes

soot deposition and clogging. All nozzle types have a hollow spray pattern similar to the nozzles used in large-scale testing. Although both nozzles have been used over the past years for several tests, the results presented in this thesis are limited to those obtained with the Delavan nozzle for consistency.

The atomized fuel is mixed with the supplied air that has been brought into rotating and turbulent motion by the static swirler. The design and layout of this swirler to obtain a flame of approximately 75 mm in diameter is detailed in [146] and uses 15 blades oriented at 25°. The swirler is 3D printed and can be easily changed to a different model to vary the mixing and thus flame characteristics. By selecting a nozzle and swirler combination, the burner power can be varied from 5 kW to 35 kW. Over this range of thermal powers for which a stable and relatively clean-burning flame can be achieved, a variety of operating parameters (input and output pressures, standoff distance to the sample, air flow rate, etc.) can result in the fire hazard characteristics prescribed by the certification standards, in terms of heat flux density and temperature. The implementation of a calibration procedure to characterize flame parameters for bench-scale fire exposure tests is one of the major contributions of the present work, provided in Ch. 4.

(a) (b)

Figure 3.3 (a) Small-scale kerosene burner during start-up, with the pilot gas flame used for ignition visible on the left of the burner outlet and (b) fully developed flame impinging on a sample. The small flamelets observed at the sample surface are the result of the burning sample.

3.2 Fire chambers

3.2.1 Exposure to fire

The experimental facilities were designed and built in a modular manner, to allow for preliminary tests to be carried out early in the project, before the full set of diagnostic tools could be implemented in the test section. The minimum configuration necessary to start material testing thus borrows heavily from the requirements prescribed in the certification standards, with the experimental facility featuring a sample holding fixture, a frame that prevents the burner flame from wraping around the sample, a pilot burner, a calorimeter to measure the heat flux and thermocouples to obtain the temperature. This basic configuration as certified by the certification standards is complemented here by the implementation of a full set of diagnostic tools. These are listed in Tab. 3.2, along with probe specifications and location of implementation.

An enclosure and fume hood were built around the test rig to control the combustion atmosphere and ventilation. The test chamber is approximately 1 m^3 in volume, with windows on 3 sides and a cutout to mount the burner on the fourth. The fume hood fitted to its top ensures sufficient ventilation to avoid the accumulation of potentially toxic products during combustion. The pressure and temperature in the vent are monitored with an orifice ring flow sensor (Nailor, D36VRL - Laboratory) and a type K thermocouple. The test chamber frame is built from T-slotted aluminum profiles which allows to easily adjust the test configurations as needed.

Exposure to fire under tensile loads

Although the static tests without external forces applied on the sample enabled by the experimental facility described in the previous section are an important tool to study the fire behavior of materials, they do not capture completely the conditions prescribed by the certification standards. In addition to preventing the transmission of a flame through an interface, firewalls must be able to fulfill their other functions during and after a fire attack, including sustaining mechanical loads. For the bypass ducts and fan cases considered in the present work, this means essentially sustaining the tensile loads resulting from the over-pressure encountered in the secondary flow during normal engine operation. For the laminates under consideration, a constant internal pressure load of 0.07 MPa (10 psi) was assumed from which the transverse hoop stress, the dominant loading, of approximately 21 MPa (3033 psi) was calculated [147].

A modified test chamber was thus designed and built that allows the installation of a burner in a tensile test machine, to enable samples to be exposed to flame attacks while under mechanical loads. The setup is shown in Fig. 3.4. The sample is shielded from both sides in a similar way as for the

Table 3.2 Data acquisition and instrumentation of the small-scale fire test rig.

Parameter	Equipment	Location
Data recorded for every test		
Ambient conditions (H,P,T)	Bosch BME280 env. sensor	Test chamber
Burner surface temperature	rugged TC, type K	Burner exit plate
Air inlet temperature	TC, type T	Burner air inlet
Fuel inlet temperature	TC, type T	Burner fuel inlet
Fuel outlet temperature	TC, type T	Burner fuel outlet
Fuel inlet pressure	Pressure transducer (Ashcroft G2)	Before inlet solenoid valve
Fuel outlet bypass pressure	Pressure transducer (Ashcroft G2)	Nozzle bypass outlet
Fuel consumption	Precision mass scale	Separate
Air injection	Mass flow controller (Omega FMA 5400))	Before air inlet
Exhaust temperature	TC, type K	Chamber exhaust connection
Sample backside temperature	TC, type K	Behind ceramic shields
Sample backside temperature	IR camera (Telops)	Outside chamber, backside view port
Time to ignition, self-ignition	GoPro, DSLR camera	Chamber window port
Data acquired during calibration		
Cooling water temperature	TC, type T	Gauge water inlet
Heat flux density	Hukseflux SBG01	Flame stagnation point
Flame temperature	TC, type R, motorizide rig	At sample position

static test rig and is held by extension rods to limit heat transfer to the tensile test machine grips. The top of the chamber is connected to four ventilation hoses, creating a symmetric upwards flow on both sides of the sample. The design allows the connection of the kerosene burner, however, the laboratory ventilation was not able to provide the evacuation flow rates necessary for operation. Ports on all sides allow to perform measurements with cameras and thermocouples during testing. Moreover, the ISO2685 mandates that components are subjected to a cooling back flow and vibration close to their resonance frequency during testing. A conventional leaf blower has been converted and adapted with tailored nozzles to mimick the conditions from large-scale testing. In addition, a mount and stinger were designed that allow to vibrate the sample during testing with an electrodynamic shaker. The experimental developments described in this section have been implemented and used for proof-of-concept tests, but the results presented in this work rely exclusively on the static test section presented in the previous section.

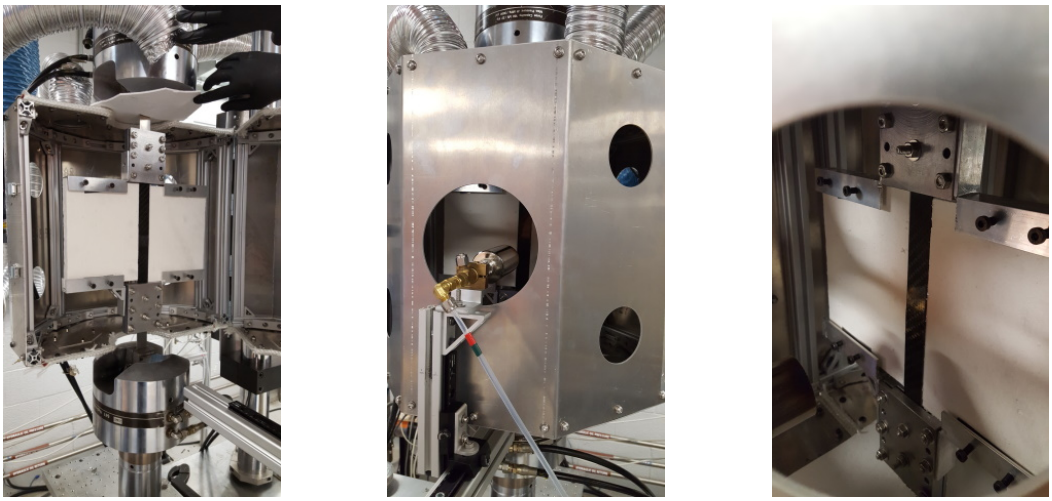

(a) (b) (c)

Figure 3.4 Tensile machine with integrated test chamber. (a) The sample is connected with extensions to the grips. (b) The burner is mounted outside the housing. (c) The sample is shielded from both sides.

3.3 Gas phase measurements

The so-called 'standard' flame defined in the applicable certification documents is defined only by two key properties: its heat flux (density) and flame temperature. As discussed above, these two parameters are not sufficient to characterize the aggressiveness of a flame attack, their measurement is key for flame calibration and must be carried out in a manner consistent with the techniques prescribed in the certification standards.

3.3.1 Heat flux density measurements - small-scale BTU heat transfer device

The advisory circular [37] and the ISO standard [9] propose a so-called BTU heat transfer device to measure the heat flux density, but also allow for alternative methods to be used as long as they are calibrated against this device. The BTU heat transfer device is in its principle a simple copper tube exposed to a flame perpendicular to the burner axis and cooled by a constant flow of water as shown in Fig. 3.5. The heat flux density is calculated from the thermal power transferred from the flame to the water.

The development of a small-scale burner thus also requires the fabrication of a suitable BTU heat transfer device for calibration. In the standard, the diameter of the tube exposed to the flame is 12 mm for a flame with a typical diameter of 230 mm to 305 mm. The flame diameter of the small-scale oil-burner is, depending on the operating parameters, approximately half this size. Using a similar tube diameter would thus cause different flame-tube interactions and potentially result in significant perturbations of the flame by the presence of the tube. To avoid such potential issues, a tube diameter half as big was selected (6.35 mm). Although the resulting small-scale BTU heat transfer device is strongly inspired by its large-scale counterpart, the hardware components have been scaled accordingly and the outdated equipment proposed in the standard (mercury thermometer, a bucket fixed to the wall) were replaced by modern equivalents. The heat flux density is calculated from the temperature difference measured with two resistance temperature detectors (RTD, Omega Engineering, PR-13E-3-100-1/4-4) with a reading frequency of 5 Hz. For comparison, measurements are only done every 30 s in the procedure outlined in AC 20-135 [37]. The cooling water flow rate is kept constant with a liquid mass flow controller (Alicat, LCR-10LPM-D) that is used in combination with a laboratory cooling water loop. The water is chemically treated to minimize sediment built-up in the tubing and is provided at a constant temperature of 20 °C. Data acquisition

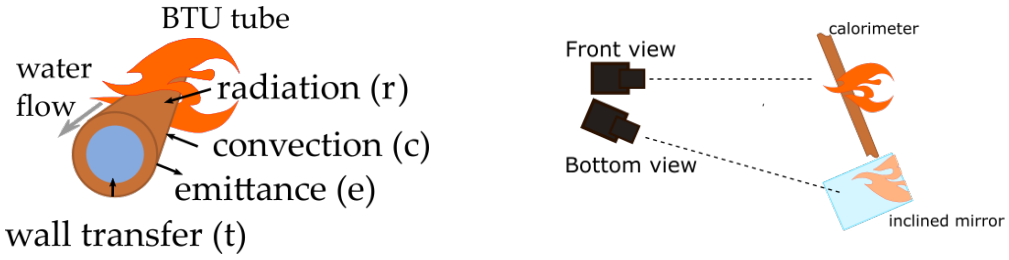

(a) (b)

Figure 3.5 (a) Heat transfer from the flame to the BTU heat transfer device. Letters in brackets are used as indices in Eq. (4.4). (b) Camera setup to estimate the flame diameter.

and device control are performed through a Labview© program. Just as in full-scale tests, the BTU heat transfer device tube is longer than the flame diameter and thus the "wetted length", i.e. the length of pipe engulfed by the flame, needs to be appropriately estimated. To facilitate this task, the setup shown in Fig. 3.5 using two cameras is proposed. An inclined mirror is placed underneath the BTU tube, one camera (Nikon D750) frontally facing the burner is positioned behind the tube and a second camera (Nikon 450D) films the mirror. Both cameras are synchronized and take an image every 2 seconds over a period of 40 s. Examples of pictures taken simultaneously from two perspectives are shown in Fig. 3.6. During post-processing, the projected dimensions of the flame along the two perpendicular optical axes are averaged using Fiji software [148] to obtain an estimate of the flame diameter at the position of the calorimeter tube.

3.3.2 Heat flux density measurements - hemispherical heat flux gauge

The heat flux density of the different flames were for the most part measured using a Hukseflux SBG01 sensor that combines the principles of a Gardon gauge and a Schmidt-Boelter gauge (Fig. 3.7). The sensor is water-cooled and has a black-coated foil (>0.95 emissivity) at its exposed surface that absorbs incoming radiation with a viewing angle of 180°. This device is thus particularly well suited for fire tests where radiation is an important heat transfer mechanism. The particular model (SBG01-200) is certified for measuring heat flux densities up to 200 kW/m^2. The gauge output in millivolts (U) was converted to kW/m^2 based on the manufacturer specifications. With a full scale output of 23.6 mV at 200 kW/m^2, the inverse responsivity of the sensor is 8.475 $kW/m^2/mV$.

The SBG01 has a standard body with a metal flange (Fig. 3.7) which allowed mounting the sensor on a flat plate holder to simplify installation. As the cooling is provided with flexible hoses attached on simple barbed fittings, it is important to prevent the flame from reaching the sensor back face. To this end, the sensor was embedded in a 25.4 mm thick low-density ceramic fibre board (Ceramaterials). Using such a backing plate has the additional advantage of creating a large area for flame impingement similar to the sample surface. Tap water was used for cooling the sensor body in an open loop configuration at a temperature of (10 ± 2) °C and a flow rate of 30 L/h.

To perform flame calibrations, the sensor is flush-mounted in the ceramic board described above and the assembly is positioned on a two-axis translation stage with y indicating vertical displacement and the horizontal displacement is given as radial distance r from the stagnation point. For most tests the sensor was aligned with the burner axis, to measure the heat flux density at the stagnation point. A detailed mapping of the gas flames has been performed by displacing the sensor vertically and horizontally in steps of 10 mm to cover a total area of 100 mm × 100 mm.

The design of this hemispherical heat flux gauge is tailored to environments with mixed radiative-

(a) Front (b) Bottom

Figure 3.6 (a) Front view showing the flame cross section perpendicular to its axis and (b) bottom view revealing the flame width at the tube location, imaged through the mirror. The flame shown corresponds to approx. 8 kW. Burner operating parameters: 3 g/s air and 0.19 g/s jet-fuel.

convective environment. Moreover, as Lam and Weckman [149] have pointed out, the measurements from water-cooled gauges may not indicate the true heat flux value received by a surface if this surface is not similarly cooled in the application of interest, which is not the case in fire resistance testing. According to the manufacturer calibration documentation, the originally stated extended uncertainty of ±3 % is further extended to 8 % for the measurement range between 100 kW/m^2 to 130 kW/m^2 by considering an uncertainty due to non-linearity of 3 % and convective contributions (2 %).

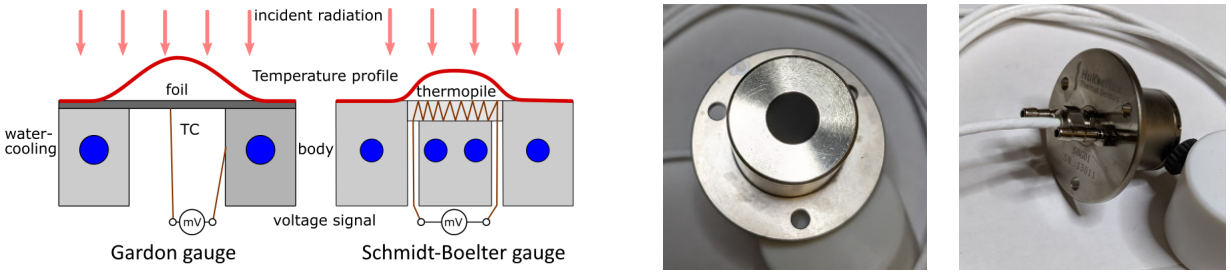

(a) (b) (c)

Figure 3.7 (a) Schematic representation of the Gardon and Schmidt-Boelter gauge desings. (b) The Hukseflux SBG01 gauges combines both principles and features a sensor with a black coating and (c) a water-cooled body.

3.3.3 Temperature measurements

Temperature measurements of the sample surface and of the adjacent gas phase are essential to understand the response of a material upon exposure to an external flame. For the results gathered

in this work, two different thermocouple-based probes were used. First, to measure flame temperatures following the procedure described in the certification standards a thermocouple rake was assembled. Following a scaling procedure similar to the one described for the BTU heat transfer device, the probe size was adapted to the scale of the burner used. Four sheathed type K thermocouples (Omega Engineering, SCAXL-125E-6), with exposed junction embedded in ceramic insulation, were mounted on a plate 15 mm from each other. This plate was fixed on a motorized stage to translate the thermocouples across the flame. The thermocouples were tested before and after fire exposure in a dry-well thermocouple calibrator (Fluke 9150).

To obtain a more reliable measure of the true flame temperature, more sensitive probes were built using small diameter type R thermocouples. To minimize conduction losses, the thermocouple wires were bent to obtain a triangular shape, with the segment containing the junction aligned with the isotherms expected in the flame. Furthermore, the thermocouples were coated with thin layer of high-temperature cement (Omega Engineering, Omegabond 600) to minimize catalytic effects. The ceramic powder was mixed with water following the manufacture instructions and the thermocouple was then dipped in the liquid ceramic. The cement required 24 h for drying before the thermcouple could be used for tests. The coating could withstand several fire tests and was renewed when visual inspection showed ablation. Fig. 3.8 shows such a thermocouple exposed to a methane flame as well as a close-up of the coating near the thermocouple junction. Despite this precautions, temperature measurements in flames remain a challenge and the raw data require post-processing to account for the different error contributions. The data analysis was performed according to the recommendations proposed by Baukal [15] and has been previously described in detail for the given setup by Béland [119].

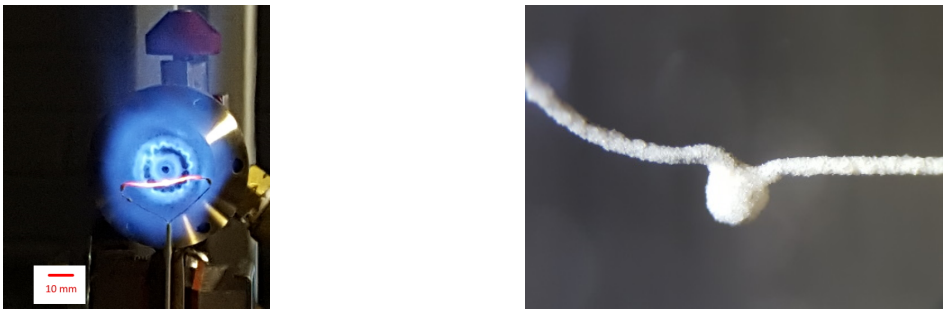

(a) (b)

Figure 3.8 (a) Triangular shaped temperature probe base on a type R thermocouple exposed to a gas flame. (b) Magnified view on the ceramic coating after the fire test.

3.4 Materials selection and sample preparation

3.4.1 Composite specimens

For the majority of the tests described in this thesis, carbon fibre (CF)-epoxy composite samples were used as baseline material representative of aerospace applications with high service temperature (up to 160 °C) outside the fuselage. Laminates were fabricated using an out-of-autoclave prepreg system (MTM45-1, Solvay), with mechanical properties found in the NCAMP database [150]. The fabric was composed of HTS40 standard modulus carbon fibres with 3K plain weave and 36 % resin content. The sample layup is $[0°, 45°, 0°, -45°]_S$ to obtain a quasi-isotropic, balanced and symmetric configuration. The thickness of the individual plies was approximately 0.201 mm and the cured panels measured on average 1.65 mm for 8 plies. Samples were cured following the manufacturer recommendations and in compliance with the NCAMP database [150].

The 25.4 mm × 305 mm coupons geometry was selected to enable a firm grip in the tensile test machine, away from the area exposed to the flame at the center of the coupons, both for post-fire mechanical properties assessment and for applying tensile loads during fire tests. Coupons were cut from large panels, typically 610 mm × 610 mm, using a water jet or a wet tile saw with a diamond blade. In addition to the 25.4 mm × 305 mm strips, other coupons geometries were used also produced for some tests where larger surface areas are needed to be exposed to the flame (100 mm × 100 mm and 305 mm × 305 mm). The samples were then cleaned and dried at room temperature prior to testing.

For a test campaign focusing on the emissivity change of the samples during thermal degradation, two phenolic-based prepreg systems were used. The first was a carbon/phenolic prepreg (CYCOM 2400-1M, Solvay) with T650 carbon fibres and an 8-Harness Satin (8HS) woven architecture. The second was a glass/phenolic (CYCOM 799H, Solvay) with a style 7781 fibre architecture. A balanced yet asymmetric $[0°, 45°, -45°, 0°]_T$ layup was used in both cases, yielding a typical thickness of 1.6 mm for carbon/phenolic and 1.0 mm for glass/phenolic samples. Both configurations were cured using the manufacturer's recommendations for autoclave curing.

3.4.2 Through-thickness temperature measurement

Instrumented samples have been manufactured to measure the temperature distribution during thermal degradation across the sample thickness for some test campaigns, as for instance tests to verify infrared thermography data with an example shown in Fig. 3.11. Some of these samples were specifically manufactured for tests as requested by our industrial partner, Pratt & Whitney Canada, but are not discussed in this thesis. To this end, very fine type K thermocouples (diameter 0.08 mm)

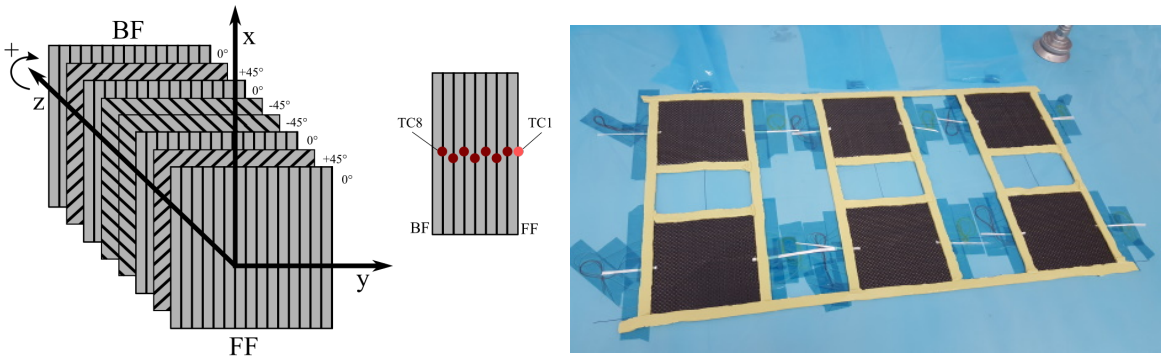

(a) (b)

Figure 3.9 (a) Composite layup and indication of TC placement between front face (FF) and back face (BF). (b) Small panels (100 × 100 mm) with integrated thermocouples framed by sealant tape.

coated with PFA have been embedded in-between plies and on both faces of composite laminates. The TC junctions were slightly staggered with respect to each other to minimize the local deformation of the fabric and local increases in the thickness of the laminate. A typical setup is shown in Fig. 3.9. The TC junction measured 0.1 mm in diameter. Due to their fragility, some of the thermocouples broke during the composite fabrication process, when the sealant tape was removed. The thermocouples were connected during the sample curing to test their accuracy, response time and stability over time. Fig. 3.10 shows as an example curves from a thermocouple on the first ply (TC1), compared against the furnace control thermocouple and a TC attached to plate on which the panel was resting during the curing cycle. The relative difference between an inner thermocouple and the outermost thermocouple (TC1) is stable over the entire curing cycle and on the order of 1 °C.

3.4.3 Metal samples

In addition to the composite samples, aluminum (Al 6061-T6) and stainless steel samples (SAE 304) were tested as well. Metal samples allowed to reduce the complexity in terms of heat conduction and surface degradation for tests focusing on IR camera flame calibration (cf. Ch. 5). The aluminum coupons were either 100 mm × 100 mm or 305 mm × 305 mm. Steel samples were only used as large panels measuring 305 mm × 305 mm. The thickness of all metal samples was 1.6 mm. The sample surface was as received and was not subjected to a particular treatment. Temperature measurement on the steel plate was performed using sturdy type K thermocouples (0.8 mm in thickness, AWG20) spot-welded to the sample backside at increasing radial distance (step size = 10 mm). Although thermocouples can be welded to the aluminum plates, the joints have a propen-

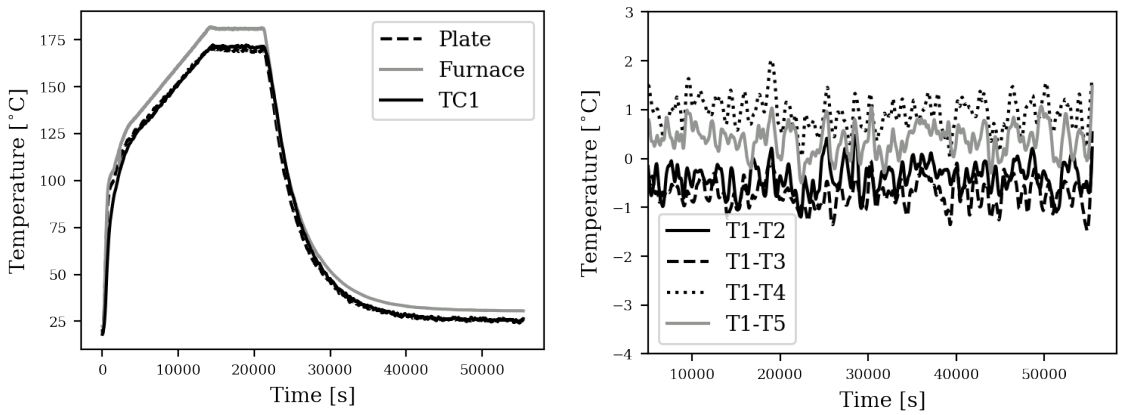

(a) (b)

Figure 3.10 Measured temperatures of CF epoxy samples with embedded thermocouples during the curing cycle. (a) The furnace temperature is compared against the temperature measured on the top of the sample and on the plate the sample rests on. (b) Temperature difference of thermocouples embedded through-out the thickness of the sample.

sity to brittleness. Instead, small dents, approximately 0.5 mm in depth, were punched into the aluminum plates at desired locations. The tip of sheated type K thermocouples was then placed in these dents and so held in place.

3.5 Two-color infrared thermography

The problem of accurately assessing the sample emissivity – necessary for conventional (single color) IR thermography – was circumvented by implementing a technique based on two-color pyrometry. The theoretical background as well as the rationale behind hardware selection, choice of acquisition parameters and post-processing approach is explained in detail in Ch. 5. The individual contributions to the overall error budget were identified and minimized. This is a significant improvement over previous implementations of infrared thermography in the context of surface temperature measurements in fire tests.

We selected a multispectral infrared camera (Telops FAST-M350) with a cooled sensor and integrated filter wheel. The camera was positioned perpendicular to the sample backside (Fig. 3.11) for which the acrylic windows of the test chamber were unmounted to guarantee an unobstructed line-of-sight. The two-color thermography technique is applied pixel-wise, which allows a temperature mapping to be obtained for the sample surface region in the field of view (FOV). Post-processing was performed using Matlab (vs. 2016) and python (vs. 3.8). In a subsequent step, the temperature mapping can be used to calculate also the sample emissivity. For validation purposes, our approach

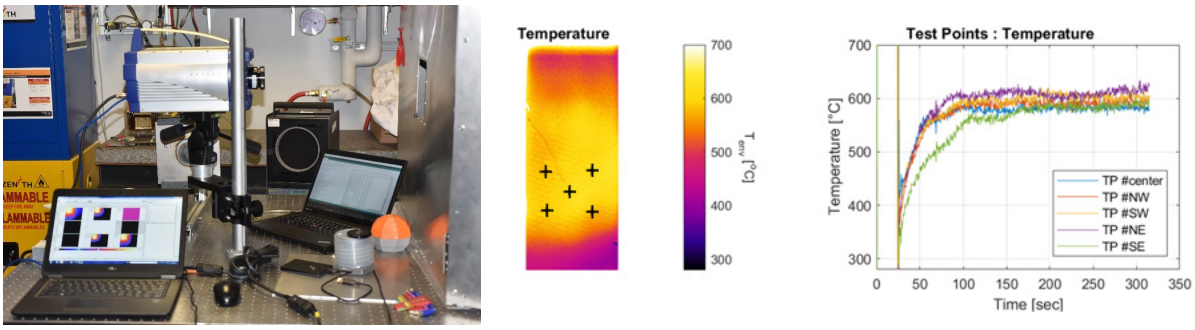

(a) (b)

Figure 3.11 (a) IR camera installed on the backside viewport of the test chamber. The black body used for calibration can be seen in the back. (b) Example of IR data and extraction of sample surface temperature on specific test points for a carbon-epoxy sample subjected to a flame.

to measure emissivity was compared against independent measurements obtained from a SOC-100 HDR Hemispherical Directional Reflectometer (Surface Optics Corporation) coupled with FTIR Spectrometer (Thermo Scientific^{TM} Nicolet^{TM} iS50).

Radiance calibration measurements were performed with a high-temperature black body (Fluke Calibration 4181). The device was set to 500 °C and tests were mainly used to verify the methodology with measurements from a surface of known emissivity and temperature. As indicated above, extracted temperature curves from IR camera data were also verified against data from TC installed during specimen prepartion (Fig. 3.11). The camera acquisition frame rate was varied between 25 Hz and 400 Hz to study its influence during the post-processing. The camera software featured an automatic exposure control (AEC) to ensure proper exposition during strongly varying conditions and fast recording rates.

3.6 Massloss

The mass change of the samples resulting from flame attack is assessed in the work presented here through cold measurements carried out on quenched samples following exposure of known duration. The samples are weighted with a milligram balance with internal adjustment (Sartorius, QUINTIX213-1S, ±1 mg) before and after the test. Attention was given to the sample manipulation during the transfer from the test rig to the scale as not to cause fragile char layers or residues to flake or fall off.

For time-resolved measurements, a continuous monitoring of the mass loss rate can be performed for large samples using load cells or linear variable differential transducers (LVDT). This continuous approach has been adopted for isotropical CF epoxy samples by Tranchard [100] (t=5 mm),

Schuhler [118](t=2.2 mm) and Chazelle [101](t=2 mm) and is compared against our punctual measurements (t=1.65 mm) in Fig. 3.12. The data points shown for our propane test combine results from two flames with nominally the same heat flux but different stoichiometry. Although a continuous assessment has the advantage that the data can be used to calculate massloss rates, the punctual measurements have no disadvantage compare to continuous measurements.

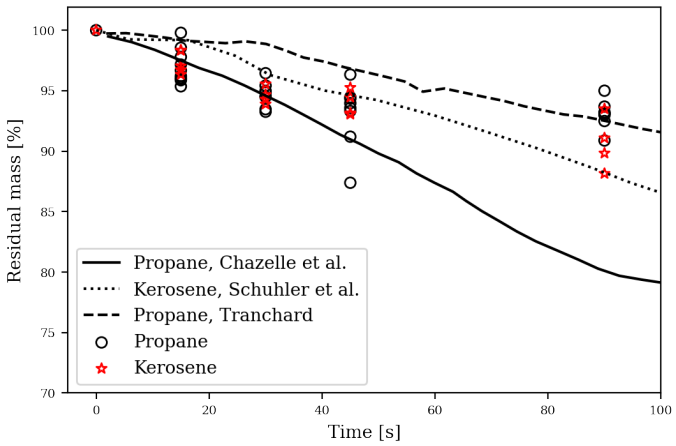

Figure 3.12 Residual mass loss profiles from carbon fibre epoxy samples exposed to calibrated gas and kerosene flames in different bench-scale setups. Data taken from [100, 101, 118].

3.7 Visual inspection and microscopy

The surface topography of pristine and burnt samples was characterized through digital microscopy (VHX-7000, Keyence), by combining multiple frames taken at various focus planes into a single image. As can be seen in Fig. 3.13, the sample condition following fire exposure features a marked three-dimensional structure, requiring the implementation of such a technique. The CF epoxy sample shown in Fig. 3.13 was subjected for only 15 s to a propane flame (116 kW/m^2) and tensile-tested post exposure. The torn fibres (centre-right) are still partially covered with charred resin whereas other regions are less thermally degraded (centre-left). In some cases, the documentation of sample degradation is limited to conventional cameras (Nikon D750). In the course of this project, more than 700 samples have been tested and in many cases, the visual analysis served a quick screening and a strictly qualitative comparison between the samples.

A part of the work presented here addresses the influence of flame chemistry on the sample degradation, including the evolution of the fibres microstructure. This requires a spatial resolution beyond what is possible using optical means, in the sub µm-range. For this purpose, the sample aera located around the flame stagnation point was cut into 25.4 mm × 25.4 mm squares for observation

using scanning electron microscopy (SEM, JSM7600F, JEOL). The acceleration voltage and other parameters have been selected according to the sample and feature of interest and shown in each SEM image with an overlay. The evaluation of fibre diameter of pores has been performed using Fiji/ImageJ software [148].

Figure 3.13 Backside of a CF epoxy sample strip exposed for 15 s to a calibrated propane flame and tensile-tested afterwards.

CHAPTER 4 ARTICLE 1 SCALING FLAME CALIBRATION FOR FIRE RESISTANCE TESTING

Tanja Pelzmann[a], Martin Lévesque[a], Étienne Robert[a]

[a] Polytechnique Montréal, 2500 Chem. de Polytechnique, Montréal (QC), H3T 1J4, Canada

This article was submitted to the *Fire Safety Journal* (May 3rd, 2022).

Abstract

The performance of firewalls for aerospace applications is tested in fire laboratories to evaluate new materials and fireproofing strategies, following test procedures set by certification agencies. For powerplant installation and propulsion system components, a standard flame provided by an approved and calibrated burner is used to burn a vertically mounted sample. The tests are typically expensive but performed with rigs and equipment not conducive to fundamental investigations on the thermal degradation mechanisms at play. This motivates the development of equivalent bench-scale tests where the fire exposure conditions can be carefully monitored and controlled. The standard flame is required to produce a heat flux density of 116 kW/m^2 and a flame temperature of 1100 °C. The former parameter is assessed with a so-called BTU heat transfer device, a water-cooled copper pipe exposed to the flame. There is therefore a need to scale this calorimetry device to different flame sizes, thus providing a calibration approach consistent with certification standard requirements for bench-top experiments. A detailed review and experimental study are performed to identify key parameters potentially altering the heat flux obtained using the device. The results presented are from experiments under certification conditions and from small-scale tests.

Keywords: Heat flux density; Fire Testing; Calorimeter; Similarity ; Scaling

4.1 Introduction

The flammability of structural aerospace materials is assessed through standardized test procedures such as those described in the FAA Advisory Circular AC 20-135 [37], AC 33.17-1A [38] or the ISO 2685 [9] standard, in which test panels are subjected to powerful external flames. One of the big challenges in improving material systems through such fire testing is that certification tests are relatively large scale and designed to be as simple as possible to implement. As a result,

they are still expensive to carry out, while having little discriminatory power to select between materials. Moreover, the certification standards do not prescribe the use of specific equipment, but rather mandate so-called standard flame conditions to which an oil burner needs to be calibrated. Specifications leave room for interpretation, allowing for margins in the test execution that promote inconsistency across different laboratories.

Considering the current requirement for the use of kerosene flames for the certification of aircraft firewalls, as specified in the relevant standards, efforts have been made to identify suitable replacements for the burners list provided in the initial version of these texts. The original Carlin burner model 200CRD, a popular choice in several fire testing laboratories, has been discontinued for more than 30 years. Its successor, the model 201CRD, can replace it relatively easily [151], requiring only modifications to the blower fan cage [65]. Furthermore, efforts have been made to harmonize equipment leading to the development of the Sonic burner [64, 73]. This burner was designed in particular to recreate the flame characteristics of a popular large-scale burner (Park DPL 3400), but with improved control over the operating conditions.

For the fire resistance testing of fire wall structures, the standard pilot flame according to AC 20135 and ISO 2685 must have a temperature of $(1100 \pm 80)\,°C$ and a heat flux density of $(116 \pm 10)\,kW/m^2$. The measurements of the flame conditions are minimal and limited to a thermocouple (TC) rake and a calorimeter to measure the heat flux density. In an accompanying document to the AC 20135, a dedicated BTU heat transfer device is proposed with the technical details specified in the Powerplant Report 3A [46]. The device is a simple water-cooled copper tube from whose sensible energy gain the thermal power of the burner is inferred. The thermal power can then be used to calculate the heat flux density. Although, the FAA regulations also theoretically allow for alternative calorimeters (suitable for a range up to $170\,kW/m^2$, accurate to $\pm 3\,\%$), the BTU heat transfer device is listed as main reference. For the flame temperature measurements, a rake is specified in the documents with seven bare junction (type K) thermocouples (TC) installed, spaced 25 mm and their beads placed 25 mm underneath the burner centre line. Tests for firewall materials are typically done on laminates and sheet material that exposed to a calibrated standard flame for five (fire resistant) or fifteen minutes for fire proofness. The evaluation of a given specimen passed test is based on failure criteria such as burn-through, backside ignition, flame spread or self-reignition upon removal of the pilot flame, to name the most prominent factors. Although, the tests use specimen sizes in the order of $610\,mm^2 \times 610\,mm^2$ and not full components, they remain still quite expensive, with protocols and harsh conditions further complicating the implementation of advanced diagnostics to assess the thermal degradation of the sample during the test. A large experimental challenge in the large-scale tests is the calibration of the burner not only to obtain a suitable flame based on spatially limited measurements, but ideally, to obtain a flame with mostly uniform characteristics. AC 20-135 [37] requires that the flame maintains the nominal conditions

over an area of 127 mm×127 mm when testing sheet materials and panels. ISO 2685 [9] breaks this up in three separate requirements: the heat flux density is defined as the one received by the BTU heat transfer device, the flame temperature for liquid fuel burners has to be within the acceptable limits for all seven thermocouples on the rake and the flame size at the burner exit plane must be at least half the panel area. To be able to associate the flame attack parameters imposed on a material to its thermal degradation, one would ideally want to submit a sample to uniform conditions, hence the need for small-scale experiments in which the pilot flames are carefully calibrated. However, the tools prescribed by the certification standards to measure flame temperature and parietal heat flux density come with severe limitations. The challenge here is therefore twofold, first scale down the calibration tools use in large-scale testing to ensure meaningful comparison with bench-scale experiments and second implement additional diagnostic means to capture precisely the conditions applied at the samples surface. A study presented by Brundage et al. [152] showed that the influence of the gas composition in proximity to the thermocouple bead and the oxidation state of the probe metals have an influence on readings. In the context of flame calibration for fire testing, where transition metal thermocouples are inserted directly into a radicals-rich flame atmosphere, catalytic effects can result in the reported temperature being several hundred degrees higher than the real gas temperature. Another important potential source of error in thermocouple-based measurements are radiation losses, this time resulting in an underestimation of the effective flame temperature. Roberts et al. [153] provided an estimation of radiation loss for sheathed TC that can be up to 10 %, and implemented a corrections requiring knowledge of probe material emissivity as well as of the thermal properties and velocity of the burnt gases. Hindasageri [154] proposed a numerical correction procedure for probes exposed to flames. Similar to the approach discussed by [152], the probe emissivity is an important value to calculate the heat transfer coefficients and the TC emissivity was measured through IR thermograpy. In his parametric study Hindasageri [154] shows that an increasing bead size increases the overall error and that TC with larger diameter also have larger errors.

However, the flame temperature definition in the standards relies only on raw data readings from the TC exposed to the flame, with no corrections or post-processing demanded. It is therefore unclear if the combined effect of catalytic heating effects and radiation losses on the thermocouple probes result in significant errors under the conditions of certification testing. A radiation correction of raw TC data from a large-scale propane burner by Talib and Neely [155, 156] indicates that the actual flame peak temperature is approximately 1900 °C, close to the expected value from equilibrium calculations, rather than the 1100 °C prescribed by the certification standard. It is unclear if such large differences are also encountered with kerosene burners.

The heat flux density is an indicator of the flame capacity to transfer its energy to a sample surface and is thus a key experimental parameter that needs to be precisely known and controlled. Although

the ISO 2685 standard allows for alternative methods in addition to the BTU heat transfer device for heat flux measurements, all measurement techniques must be calibrated against this standard apparatus. Although the BTU heat transfer device has important limitations in terms of precision, stability and relevance for heat flux measurements against a flat surface, its low cost, availability and ease of implementation made it the de-facto standard device for flame calibration in fire resistance testing.

With an increasing interest in researching fire resistance phenomena, several bench-scale setups have been developed recently [100–102, 121]. The research community is faced with several challenges related to calibration of these small-scale experiments, in addition to a general lack of uniformity in hardware selection for the pilot burner itself, complicating the comparison of results between groups and with large-scale tests. In this work, we specifically address the scaling of the BTU heat transfer device for heat flux density measurements and of thermocouple probes for flame temperature calibration. For the former, we propose a small-scaled version suitable for bench-scale setups. The heat flux densities thus measured are compared with measurements carried out using thin film gauges (TFG) and to large-scale calibration data gathered as per AC 20-135.

4.2 Material and methods

4.2.1 Large-scale burner

For the results presented here involving large-scale tests, two different burners will be used. The first is a modified Carlin 201CRD, situated in the Pratt & Whitney Canada fire testing laboratory, equipped with a Monarch 70 °PL (hollow cone) fuel nozzle, rated at 1.9 g/s (2.25 GPH) with the pressure being typically above the supplier rating of 620 kPa (90 psi). The second is the so-called Sonic burner, developped by the FAA based on the Park DPL 3400, operated by Resonate Testing Ltd in Northern Ireland. The flame characteristics of such large scale burners are largely influenced by the stator shape and orientation [157]. Fig. 4.1a shows the swirler or stator arrangement of the FAA sonic burner, compared with that of the Carlin burner where the stator is also called the "flame retention head" (Fig. 4.1b). This device anchors the flame close to the burner exit and reduces its length. Without the retention head, the mixing of fuel and air is less efficient and spatially delayed.

4.2.2 Small-scale burner

A small-scale kerosene burner has been developed [146] to recreate the flame characteristics of the FAA sonic burner [158]. It uses a pressure-atomizing by-pass nozzle to achieve variable but low flow rates with a consistent spray pattern (Delavan Vari-Flow 33769-2 with adapter 17147) at a rated supply pressure of either 689 kPa (100 psi) or 2068 kPa (300 psi). Preliminary tests showed

(a)

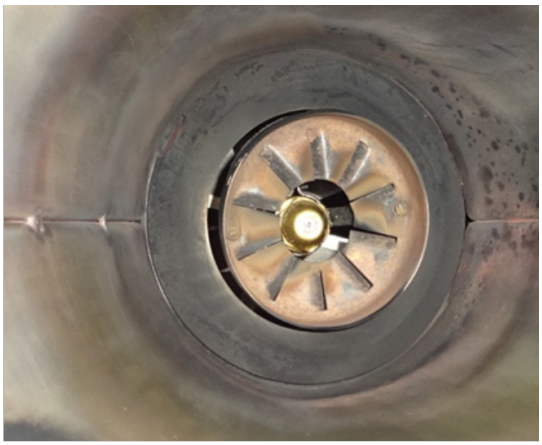

(b)

Figure 4.1 View inside the burner cone shoring the fuel injector and swirler arrangment. a) FAA sonic burner with a Monarch HS215 stator and a Monarch F-124 turbulator. b) Carlin burner with a stator (no part number available).

that higher inlet pressure levels are more suited to attain the flame volume and characteristics required. The nozzle spray pattern is, similar to the large scale burner, a hollow-cone of nominally 60° for the lower inlet pressure level (689 kPa (100 psi)). However, the spray angle increases as the flow rate decreases. The fuel is jet-A with a density of 808 kg/m^3 at room temperature.

One of the greater challenges in scaling the FAA sonic burner was to properly recreate its characteristics in terms of turbulence, mixing behavior and flame pattern. To this end, a stator has been designed and optimized using computational fluid dynamics (CFD) cold flow simulations [146] to induce rotational motion in the air stream. The air pattern thus created must be compatible with the nozzle spray pattern and angle. A turbulent region ensures adequate air entrainment around the fuel cone, resulting in a central zone with much lower air velocity. The swirler design implemented differs slightly from its large-scale counterpart, featuring 15 vanes oriented at 25°. The swirl number (SN, the ratio between the flux of angular and axial momentum) is estimated at 0.44 and is an indicator of the intensity of the rotating flow at the burner exit. Fig. 4.2 presents the results of the CFD simulation based on a $k - \omega$ SST (shear stress transport) model with the instantaneous air velocity streamlines through the stator shown in Fig. 4.2a. Due to the design of the burner housing close to the burner exit, the swirler is surrounded by a high thermal mass. This allowed the use of 3D printed poly lactic acid (PLA) to fabricate the swirler, allowing for the convenient adjustment of the flame characteristics and combustion behavior by changing the swirler geometry.

Fuel inlet pressure, bypass pressure and temperature as well as air temperature and ambient conditions are monitored throughout the tests. The air supply is set using a calibrated Omega FMA5400

flow controller. With a diameter of approximately 100 mm at a distance of 75 mm from the burner nozzle, the flame used for our small-scale experiments is roughly one third the size of a large-scale burner flame (Fig. 4.2b). Preliminary work on the scaling methodology, calibration and analysis of the burner performance have been published previously [119].

4.2.3 Heat flux density calibration

The large scale BTU heat transfer device used in this work to calibrate the large-scale burners is compliant with the definitions and requirements as specified in the certification documents [46] and shown in Fig. 4.3. The exposed tube has an outer diameter of 12.5 mm, a wall thickness of 0.8 mm and is 305 mm long. The thermocouple probes are connected through fittings to the water inlet and outlet of the centre tube. The device can be translated horizontally and vertically relative to the burner exit plane, to find and measure the maximum heat flux density at the position where test specimens are located.

The flow configuration for the flame impinging on a large-scale BTU heat transfer device is shown schematically as scenario I in Fig. 4.4a. Here the flame is much larger than the calorimeter tube and as a result is removes only a small portion of the total heat available. As the flame diameter in the small-scale burner is approximately one third of that produced by large-scale certification burner, using the same tube diameter as the proposed by ISO 2685 [9] would significantly change the jet impingement characteristics. In a situation such as Scenario II in Fig. 4.4a, flow separation and transient turbulent flow downstream of the tube can occur, resulting in flame-structure interactions that can affect heat transfer characteristics. Although a bigger tube relative to the flame size would be useful to approach the configuration of the certification test, a flat sample as shown schematically in scenario III in Fig. 4.4a, this would significantly change the heat transfer characteristics relative to the experimental tools specified in the certification standards. To avoid such issues, the calorimeter tube dimensions require scaling. A similarity analysis was performed to cover geometrical, thermal and fluid dynamic aspects. For the purely geometric aspects, orientation and flow direction are kept the same and all dimensions can be scaled linearly due to the circular cross-section.

The procedure to identify the tube diameter was as follows: First, an attempt was made to keep the ratio of temperature differences between the flame and the tube outer surface (T_1) to the difference between the tube outer and inner surfaces (T_2) constant between experimental scales.

$$\left[\frac{T_1 - T_2}{T_1 - T_{\text{flame}}}\right]_{\text{large-scale}} = \left[\frac{T_1 - T_2}{T_1 - T_{\text{flame}}}\right]_{\text{small-scale}} \tag{4.1}$$

This yields a tube outer diameter on the order of 6 mm for bench-scale experiments, with the closest commercially available diameter being 6.35 mm (1/4 in). Commercial grade copper tubing with a

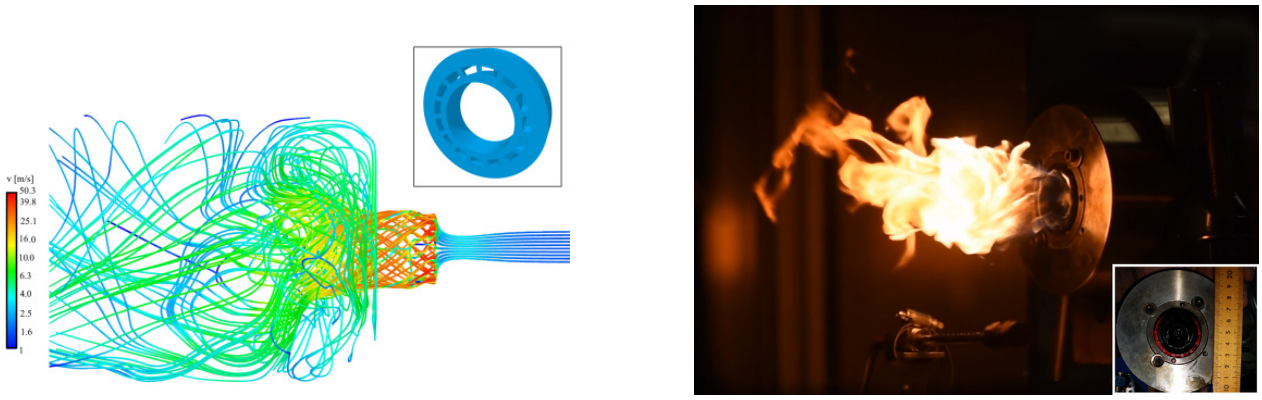

(a) (b)

Figure 4.2 (a) CFD simulation of the air flow through the small-scale burner swirler, performed with the Simscale software. The swirler is shown on the top right. (b) Kerosene flame stabilization close to the burner injector. The insert shows the front side view of the burner with the orange PLA swirler located behind the fuel nozzle.

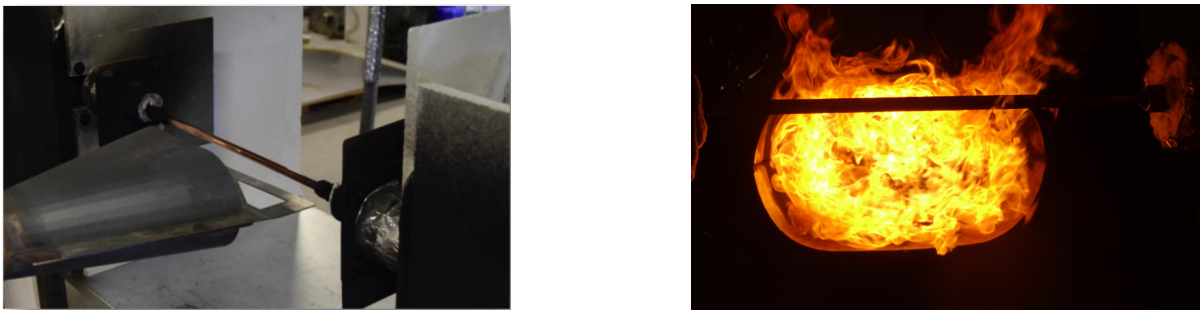

(a) (b)

Figure 4.3 (a) BTU heat transfer device positioned 102 mm (4 in) from the edge of the burner extension tube. Reflective shields and fibre boards on both sides are also visible. (b) Visualization of the tube vertical displacement required to capture the maximum flame heat flux density, to account for flame buoyancy.

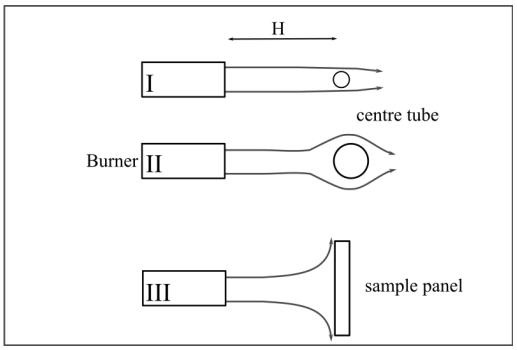

(a)

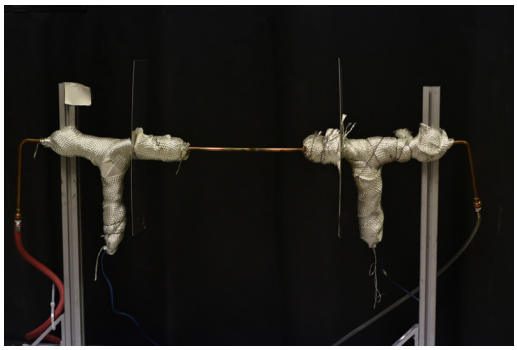

(b)

Figure 4.4 (a) Schematic representation of the heat transfer configuration for the flame impingement on a tube and on a flat wall. Adapted from [79]. (b) Small-scale heat transfer device with reduced exposed tube length and diameter. RTD probes are used to measure upstream and downstream temperatures, facing downwards and wrapped in high temperature glass-like cloth.

wall thickness of 0.7 mm was used. The water temperature measurement was performed upstream and downstream of the test section with platinum resistance thermometers (RTD, Omega Engineering, PR-13E-3-100-1/8-6), protected with a high temperature glass-like cloth.

The heat transfer between the copper tube and the water in the large-scale is considered instantaneous, with the pipe flow being laminar and mainly controlled by the Reynolds number:

$$Re = \frac{\rho v L}{\mu} \tag{4.2}$$

where ρ is the density, v is the velocity, L is the characteristic length and μ is the dynamic viscosity. For water flow in a pipe, the characteristic length is the pipe diameter D and the velocity can be extended to the water volume flow rate $\dot{V}$. To maintain the same heat transfer characteristics during scaling, the following model law needs to be satisfied:

$$\left[\frac{\dot{V}}{D}\right]_{\mathrm{LS}} = \left[\frac{\dot{V}}{D}\right]_{\mathrm{SS}} . \tag{4.3}$$

Using this approach, the flow rate of the small-scale (SS) apparatus was selected at 92 L/h, compared to 227 L/h for the large-scale setup. The same material and surface properties were used for all calorimeter tubing, i.e. hard copper (type L) with a cleaned surface as specified in [46]. Non-filtered tab water was used in an open circuit and the temperature was monitored to ensure that it is at room temperature (21 °C) when entering the circuit. The resulting small-scale BTU heat transfer device is shown in Fig. 4.4b. The exposed tube measures 20 cm in length, corresponding approxi-

mately to the maximum flame diameter that can be produced by our bench-scale kerosene burner. However, for flames calibrated to achieve the conditions prescribed in the certification standards, the length of copper pipe engulfed by the flame ("wetted length") is much shorter than the total exposed area.

As discussed above, the heat flux measurements using the BTU heat transfer device are complicated to implement and do not give an accurate measure of the heat flux density transferred to a flat surface, the configuration encountered in our tests, as shown schematically in Fig. 4.4a. To obtain more reliable and simpler heat flux density measurements, we also carried out measurements on our small-scale flames using a thin film gauge (TFG, Hukseflux, SBG01), calibrated for up to $200\,\mathrm{kW/m^2}$. For the heat flux calibration using either the small-scale apparatus or the TFG, the device was positioned at a standoff distance H equal to the separation between the burner and the sample, typically 75 mm. The device (tube or gauge) was shielded by an insulating ceramic fibre board until the flame stabilized for a few minutes, which was then manually removed to start recording.

The large-scale tests were performed at the facilities of Pratt & Whitney Canada and Resonate Testing Ltd. In both cases, the burner is allowed a 5 min warm-up period after ignition prior to the start of the calibration. After translating the burner in front of the BTU heat transfer device, the thermal power is measured for a minimum duration of 3 min and afterwards the burner is transferred immediately to the vertically mounted test panel. It is important to note here that for all burner presented here the control parameters are precisely set, yielding very repeatable results, independent from ambient conditions.

4.2.4 Temperature measurements

To measure the flame temperature, thermocouple-based probes are used. Similarly as for heat flux density measurements, the probe sizes were scaled to match the size of the flames in the small-scale tests and ensure similar heat transfer characteristics. Temperature measurements of the flame were performed with coated (Omega Engineering, Omegabond 600) type R thermocouples (0.3 mm in diameter) as specified in Ch. 3.

For the temperature calibration, a thermocouple rig was mounted on motor-driven stage that allowed to position the TC rake in the flame without opening the test chamber. A typical warm-up period of 30 s was considered. Due to space constraints in the small-scale experimental chamber, it was not possible to switch the thermocouple rake for the small-scale standard apparatus without infringing the safety of operation. The temperature and heat flux measurements where thus performed in separate test sessions.

For the calibration of the large scale burners, after flame stabilization the burner is transferred on a motorized stage in front of a thermocouple rake. Tests are performed with 7 thermocouples simultaneously, with the rake moved vertically across the flame in steps of 25.4 mm to map the temperature field for a given standoff distance to the burner. Burner parameters are modified at this stage to satisfy the temperature requirements before evaluating the heat flux density using the BTU heat transfer device, as described previously.

4.3 Heat flux density calculation

The heat transfer from the flame to the tube in the BTU heat transfer device has a radiative and a convective component. The tube itself emits some of the heat received by radiation towards its surroundings, with the remainder being transported by the water flow. The resulting energy balance on the tube is:

$$\dot{q}_r + \dot{q}_c = \dot{q}_e + \dot{q}_t \tag{4.4}$$

The contributions are $\dot{q}_r$, the radiative power received, $\dot{q}_c$, the convective power received, $\dot{q}_e$, the radiative power emitted and $\dot{q}_t$, the thermal power transported by the flowing water. The calculations presented in ISO 2685 and AC 20-135 [9,37] assume the heat transfer from the flame to the tube to be purely convective and equal to the heat transfer from the tube to the water:

$$\dot{q}_c = \dot{q}_t = \dot{m} c_p \Delta T \tag{4.5}$$

In the certification standards, the quantity of interest to characterize the heat transfer potential of the flame is the heat flux density. This is simply calculated by dividing the heating power received in the water by the surface of the calorimeter pipe, assuming that the tube is engulfed entirely around its circumference:

$$\dot{Q}_{\text{flame}} = \frac{\dot{m} c_p (T_{\text{out}} - T_{\text{in}})}{\pi D_{\text{tube}} L_{\text{WL}}}, \tag{4.6}$$

with:

$\dot{m}$	mass flow rate of water [kg/s]
c_p	Heat capacity of water [J/(kgK)]
$T_{\text{in/out}}$	Temperature of water flowing *in* and *out* [K]
D_{tube}	Outer diameter of BTU device centre tube [m]
L_{WL}	"Wetted" length of the tube, engulfed by the flame [m]

There is therefore an obvious ambiguity regarding the length of pipe L that should be considered for this calculation, with common values being either the total pipe length (between the two reflective shields installed on either sides of the test section) or the effective "wetted length" in the flame, measured through photographs.

As this calorimetry technique was first proposed in the context of aerospace firewall certification through FAA's advisory circular AC 20-135, the operation parameters for the BTU device are often still considered in the imperial unit system. As such, L_{WL} is frequently fixed at 11 in (279.4 mm) and the denominator becomes $0.5\pi \cdot 11$ in (11 148 mm^2). The heat capacity of water is assumed with 1 BTU/(lbF) (4190 J/(kgK)) and the flow rate is set according to the regulations at 500 lb/h (3.78 L/min). Since the standard specifies the heat flux density in BTU/(sec – ft^2), an additional factor has to be added to maintain the units consistent:

$$\dot{Q} = \frac{500 \cdot 1 \cdot (T_{\mathrm{out}} - T_{\mathrm{in}})}{\pi \cdot 0.5 \cdot 11 \cdot 0.006944 \cdot 3600} = 1.16(T_{\mathrm{out}} - T_{\mathrm{in}}) \tag{4.7}$$

The target values lies between 9.3 BTU/(ft^2−sec) and 11.1 BTU/(ft^2−sec). With most parameters predetermined, a typical temperature difference measured with the BTU heat transfer device ranges from 8.0 °F to 9.6 °F (3.8 °C to 5.3 °C). Data obtained using the large-scale Carlin CRD oil burner, fitted with a Monarch 2.25 GPH 70° nozzle and a modified swirler is shown in Fig. 4.6a and Fig. 4.6b.

Following the test protocol, the burner needs to be calibrated before and after the tests, to capture eventual changes in flame conditions. Two things are important to note. First, the heat flux curves for a single calibration run slowly decline over time as can be seen in Fig. 4.6a. Second, the heat flux measured at the beginning of a fire resistance test is typically significantly higher than the same calibration performed following a 15 min fire test. Both observations are linked to the same cause, the soot deposition on the copper tube exposed to the flame (Fig. 4.5).

The operating conditions of the large-scale burners are chosen to be representative of a standard fire hazard, with combustion efficiency out of consideration. Consequently, flames are often locally rich with a high prevalence of soot particles that tend to deposit on the BTU heat transfer device tube during calibration. The particulate fouling due to incomplete combustion is driven by diffusion and thermophoresis, adding thermal resistance between flame and tube as shown schematically in Fig. 4.5b. The fouling rate is influenced by the soot particle concentration, heat flux, fluid flow velocities, surface temperature and condition. Thus cleaning the soft copper tube with for example steel wool creates more sites for carbon built up.

The fouling factor R_f, characterizing the growth rate of the soot layer, may be understood as the balance between the soot deposition and removal rate [159]:

$$R_f = \Gamma_{\mathrm{deposition}} - \Gamma_{\mathrm{removal}} \tag{4.8}$$

However, the removal rate is negligible here as the tube is located in the rich region of the flame

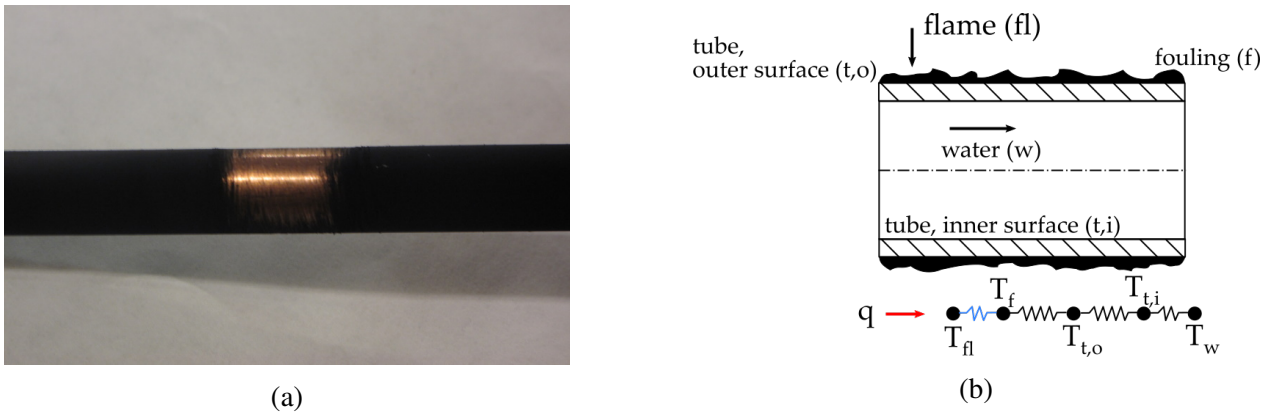

(a) (b)

Figure 4.5 (a) Close-up of the centre tube showing soot deposition after two subsequent calibration runs of 3 min each. (b) Schematic representation of the heat transfer between the flame, fouling soot layer, both tube surfaces and water.

where soot oxidation is weak. The amount of material deposited per unit area m_f depends on the density ρ of the foulant and its thickness x_f, which are both linked to the fouling factor and the thermal conductivity of the soot layer k_f through:

$$m_f = \rho_f \cdot x_f = \rho_f \cdot k_f R_f \longrightarrow R_f = \frac{x_f}{k_f} \tag{4.9}$$

Among available fouling models, the analysis proposed by Knudsen [160] allows the expression of the fouling rate as a function of the change in heat transfer coefficient and thus to write the change in heat flux as the tube transitions from clean (c) to fouled (f) as :

$$\frac{q_f}{q_c} = \frac{1}{h_c R_f + 1} \longrightarrow q_f = \frac{q_c k_f}{h_c x_f + k_f} \tag{4.10}$$

4.4 Results and Discussion

4.4.1 Heat flux density in large-scale burners

Fig. 4.6 shows heat flux density measurements obtained with the BTU heat transfer device, with Fig. 4.6a containing specifically the curves corresponding to the pre- and post-test temperature calibrations presented in Fig. 4.8a and Fig. 4.8b. In the first case (Fig. 4.6a), the heat flux density is well above the target values indicated by grey horizontal bars, despite the flame temperature being in the acceptable range. This very aggressive flame has nevertheless been used for certification testing, as a result of the operating characteristics of the Carlin burner and of the introduction of additional requirements by the FAA in 2009. The Advisory Circular AC 33.17-1A [38] requests

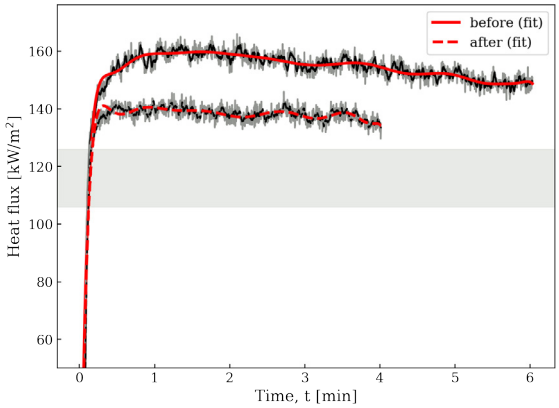

(a)

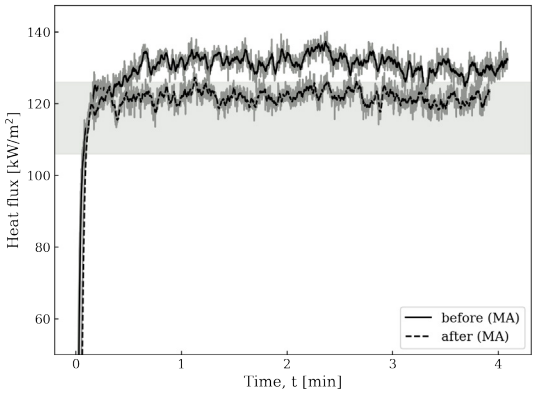

(b)

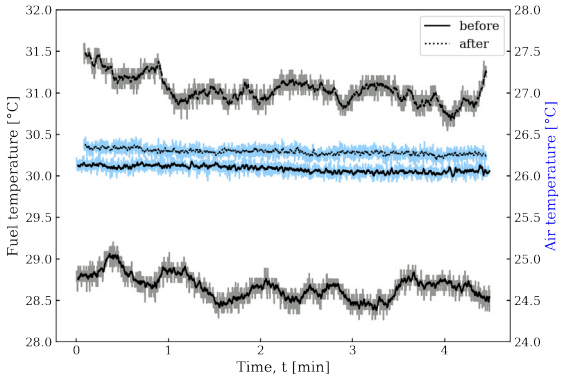

(c)

Figure 4.6 (a) and (b) Heat flux calibration data from large-scale tests using a Carlin 205 burner with (a) large and (b) moderate decrease in apparent power due to BTU tube fouling. The gray area shows the desired heat flux range according to ISO 2685. (c) Fuel and air temperature during the calibration before and after the fire resistance test. Raw data has been converted from imperial to SI units.

now a minimum average flame temperature of 1100 °C for seven adjacent thermocouples in the rake, as opposed to the original standard AC 20-135 that allowed for a temperature range ((1100 ± 80) °C). To satisfy this minimum requirement, the fuel flow rate needs to be increased, which consequently increases the heat flux. Tests conditions for composite materials intended as firewalls thus exhibit a discrepancy when performed under FAA regulations or when following the ISO 2685 European standard, that does not have this additional requirement. The Carlin burner flame is particularly prone to influence from the test environment, because the air of combustion is provided through a fan. Fig. 4.6b shows an alternative calibration test with a significantly reduced difference between the before and after test run.

Another factor to note is the apparent decrease in heat flux density between pre- and post test calibration. For the curves shown in Fig. 4.6a, the difference amounts to approximately 19 % and for the tests depicted in Fig. 4.6b, the difference is approximately 9 %. The measured heat flux density not only decreases between the two calibration runs but also during measurement. As discussed above, both effects are linked to the soot deposition on the calorimeter tube, with an example shown in Fig. 4.5. Using average values from Fig. 4.6a, the heat flux measured with the fouled tube (f) is $0.81 q_c$, with q_c the heat flux measured with the clean (c) tube. The simplistic approach to account for fouling by the Knudsen model introduced in Eq. (4.10) allows to solve for the soot layer thickness x_f:

$$x_f = \frac{k_f - 0.81}{0.81 h_f} \tag{4.11}$$

Based on data from Chang et al. [161] for candle soot and using literature values for the heat transfer coefficient from Welker et al. [162] the soot layer thickness shown in Fig. 4.5b for a tube exposed twice for 3 min is estimated at 500 µm. The particle deposition rate and thus final layer thickness depends among other things on the combustion efficiency. Without changing the fuel or oxidizer flow rates, a change in the combustion efficiency is mainly linked to differences in the atomization of the fuel in the nozzle. Many factors can result in such differences, but here fuel temperature is a likely suspect. Fig. 4.6c shows that the fuel temperature has increased on average by 3 °C between the two measurements, and consequently the fuel viscosity has decreased. Based on literature data from Fortin [163] on aviation fuel, this decrease is equal to approximately 4 %. For pressure driven nozzles, the droplet size will decrease as the viscosity decreases, improving the overall combustion efficiency. The particle deposition rate can thus be expected to be lower during the second calibration measurement, as can qualitatively be seen by the lower slope in the data shown in Fig. 4.6a.

To avoid time consuming and costly calibration procedures involving repeated alternating temperature and heat flux density measurements, common practice therefore often involves adjusting the burner power to ensure meeting the temperature criteria, knowing that the excessively high heat

flux will be artificially recorded lower following the test due to tube fouling. Adjusting the burner more frugally can be risky, as shown in the calibration data presented in Fig 4.6b. In this case, the post-fire heat flux density falls within the desired values, but just barely. Slightly more soot-caused fouling of the calorimeter tube would have resulted in a failed post-test calibration and in a wasted specimen.

To allow comparison between heat flux density measurements carried out with the BTU heat transfer device and more convenient sensors, a TFG sensor was placed at the same horizontal position H from the burner cone, 25.4 mm above the burner centerline (Fig. 4.7a). These tests have been performed with a Sonic burner. For these measurements, the gauge is water-cooled but not the ceramic shield in which it is embedded, leading to the measurement of the heat flux towards a wall with non-uniform temperature distribution. The surrounding fibre board absorbs heat from the flame and causes additional heat flux transfer to the sensor. The difference between the heat flux density readings obtained via the TFG and the BTU device is approximately 12 % with only the first part of the BTU measurement considered. This deviation can be partly attributed to the additional contributions from the board which according to Ochs et al. [164] can increase the overall reading by 13 %.

4.4.2 Flame temperature in large-scale burners

Temperature mappings based on raw data obtained from the calibration of a Carlin burner in a large-scale certification setting are shown in Fig. 4.8. The maps are used to qualitatively assess the temperature distribution in the flame. Assuming that the flame cross section is equal to the burner cone cross section (375.68 cm^2), the area where the temperature is within the prescribed threshold covers approximately 32.6 % of the cross section in the first calibration run and approximately 34.3 % after 20 min of continuous operation. The overall spatial variation between the two temperature maps can be considered negligible and within the uncertainty of the measurement.

The curves in Fig. 4.8c were acquired with a rake of seven thermocouples positioned slightly above the horizontal centre line of a sonic burner. With an average horizontal flame width of 280 mm, the thermocouple rake covers approximately 50 % (150 mm) of the flame diameter. These demonstrate that the burner cone geometry prescribed by the certification standards results in the formation of a central hot spot in the flame with little temperature variation, with a diameter of approximately 19 cm.

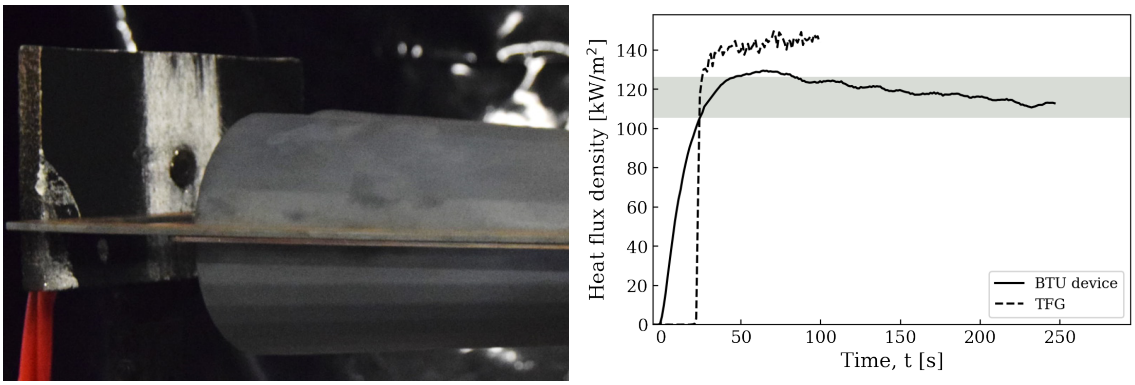

(a) (b)

Figure 4.7 (a) Positioning of TFG sensor with respect to the burner exit cone. (b) Comparison of the heat flux density measurements from TFG and BTU devices with a burner calibrated to nominal certification values.

4.4.3 Heat flux measurements in the small-scale burner

Similar to the campaign performed with the large-scale burners, the heat flux density measurement was carried out both with the scaled-down version of the BTU heat transfer device and with a thin film gauge. The results are compared in Fig. 4.9. Similar to the large-scale tests, the cooled gauge is mounted in a ceramic board. The heat flux difference between the two methods is approximately 16 %. Visual inspection of the TFG sensor after the tests showed a slight coating damage, and an additional error of 3 % is assumed. Based on tests performed with a similar TFG from the same manufacturer, the measurement uncertainty for this gauge is estimated at $\pm 12\,\mathrm{kW/m^2}$.

4.4.4 Temperature measurement in the small-scale burner

The flame of the small-scale kerosene burner used in this test campaign is approximately a third in diameter compared to the large-oil burner. Instead of a fixed rake placed in front of the burner, four thermocouples have been installed on a motorized stage and travelled through the flame. Fig. 4.10 shows the flame temperature data obtained during calibration. Contrary to the large-scale test data, these results have been corrected with the iterative method described in detail by Béland [146] and also proposed by Kao [142]. The average temperature across the four thermocouples is $(1067 \pm 37)\,°\mathrm{C}$. Due the hollow cone nozzle and the swirler design (Fig. 4.2), the mixing in the centre area of the flame creates a zone with homogeneous heat flux and temperature distribution of approximately $35\,\mathrm{mm} \times 35\,\mathrm{mm}$ which is approximately 16 % of the flame cross section.

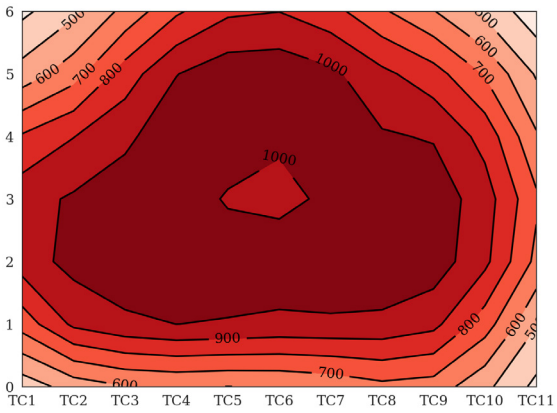

(a) Pre-test

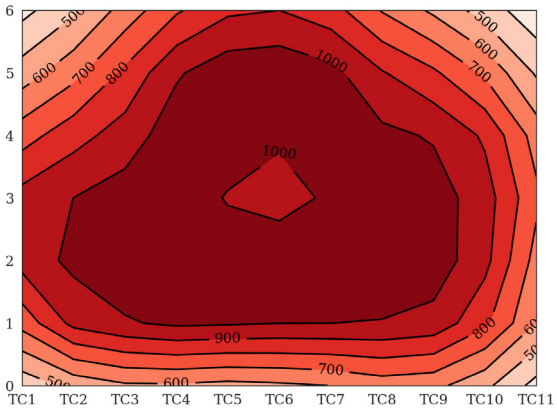

(b) Post-test

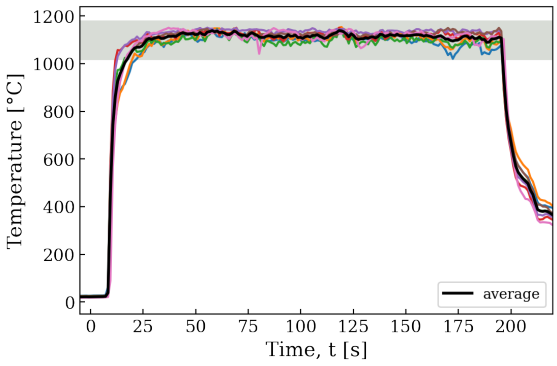

(c) Pre-test

Figure 4.8 (a) and (b) Temperature mapping from a rake of 11 thermocouples travelling vertically in steps of 25.4 mm, in a plane 102 mm from the burner exit, before and after fire testing using a Carlin burner.(c) Line mapping at a singe position as specified in the standards from a Sonic burner.

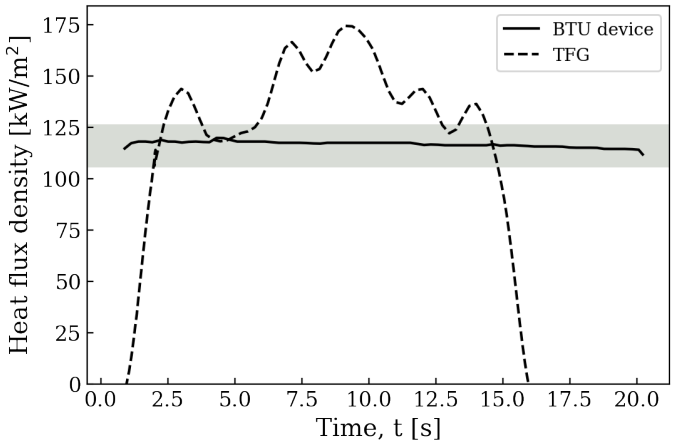

Figure 4.9 Heat flux measurements performed with a thin film gauge and the small-scale standard apparatus.

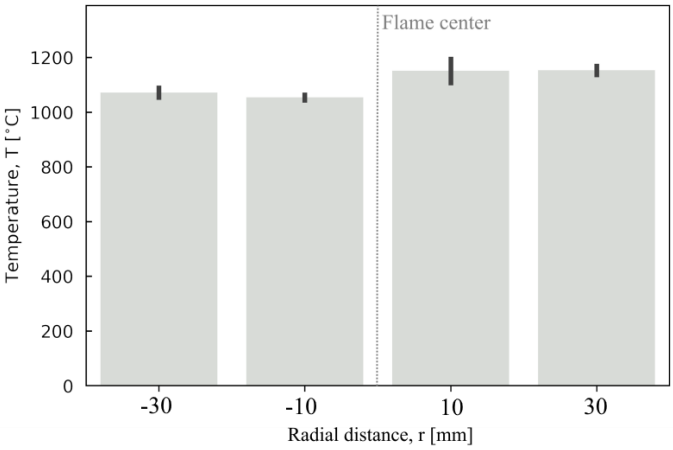

Figure 4.10 Time-averaged and radiation corrected thermocouple data indicating the flame temperature at different horizontal positions from the flame centre.

4.5 Conclusion

To calibrate a pilot flame used to recreate the conditions prescribed in aerospace firewall testing, we scaled the water flow calorimeter and temperature probes commonly used in fire testing laboratories. The results from the so-called standard BTU heat transfer device are also compared against measurements from a simple to implement thin-film gauge. The calibration results demonstrate that bench-scale experiments can adequately reproduce the certification conditions, but that appropriate calibration tools must be used to capture the biases induced by the requirements of the appropriate standards.

A major problem when using the BTU device for calibration is the intensive carbon built-up that leads to an apparent decrease in heat flux density. With the addition of restrictions for the minimum average flame temperature, components tested under FAA regulations undergo mush harsher conditions than when tested according to European standards. The small-scale burner is able to reproduce the demanded heat flux density and flame temperature at a horizontal standoff distance of 75 mm and has symmetric temperature distribution with homogeneous centre zone that is wider than the intended coupon sample width of 25 mm.

The preliminary tests show that the heat flux measurement methods used in current fire testing need a more thorough review. Future tests should benefit from advanced diagnostic tools such as laser induced fluorescence spectroscopy or infrared thermography. In addition the heat flux measurements integrating TFG sensor in cooled plates could provide a better understanding of the heat received by the sample.

Declaration of competing interest

The authors declare no potential conflicts of interest with respect to the research, authorship, and/or publication of the this article.

Funding

The authors want to acknowledge the financial support from the Natural Sciences and Engineering Research Council of Canada (NSERC/CRSNG) grant no. CRDPJ 478687-15, and the partners from CRIAQ ENV-708 project.

Acknowledgements

The authors wish to express their gratitude towards Mary Dowey and Tom Mallon from Resonate Ltd. for sharing their calibration data, but even more for the in-depth technical discussion that helped to improve our bench-scale tests. We wish to thank Simon Hind from the National Research Canada for many insightful discussions. Martin Cloutier, Jason Hamp and Barry Barnett from Pratt & Whitney Canada provided burner calibration data and many otherwise unaccessible technical details on certification testing for which we are very grateful.

CRediT authorship contribution statement

Tanja Pelzmann: Conceptualization, Data Curation, Formal analysis, Investigation, Methodology, Software, Writing - Original Draft, Writing - Review & Editing. **Martin Lévesque:** Funding acquisition, Supervision, Writing - Review & Editing. **Étienne Robert:** Funding acquisition, Supervision, Writing - Review & Editing.

CHAPTER 5 ARTICLE 2 SURFACE TEMPERATURE AND EMISSIVITY MEASUREMENT FOR MATERIALS EXPOSED TO A FLAME THROUGH TWO-COLOR IR-THERMOGRAPHY

Tanja Pelzmann[a], Fabien Dupont[b], Benjamin Sauté[a], Étienne Robert[a]

[a]Polytechnique Montréal, 2500 Chem. de Polytechnique, Montréal (QC), H3T 1J4, Canada
[b]Telops Inc., 100-2600 St-Jean Baptiste Ave, Québec (QC), G2E 6J5, Canada

This article was submitted to the *International Journal of Thermal Sciences* (March 14th, 2022).

Abstract

Two-color (2C) pyrometry has long been used for flame temperature and soot concentration studies and is now becoming more widely used to measure surface temperatures of burning materials. With the obvious advantage of being a contact-free method that requires only minimal optical access, 2C pyrometry combined with high-speed acquisition is a promising diagnostic tool to obtain exceptional temporal and spatial resolution of thermally degrading samples. However, its conceptual simplicity relies on a set of basic assumptions that when violated can result in large errors. In this work, we use an experimental configuration representative of fire resistance testing for aerospace and naval applications to analyze the impact of camera parameters and test setup on the accuracy of the surface temperature results obtained. Two types of fibre reinforced polymer composites and a steel plate are used to investigate material specific aspects that affect the measurements. An improved workflow for camera calibration is presented that takes the actual experimental setup into account. The temperature and emissivity mapping obtained trough in-situ IR measurements is compared against data acquired through thermocouples and post-fire hemispherical directional reflectance measurements at room temperature. This comparison illustrates the necessity for proper post-processing and demonstrates that emissivity values obtained from pristine or burnt samples are not well suited to obtain accurate surface temperatures through conventional (single color) IR thermography. We also present a detailed error budget and suggestions for calibration measurements to keep the overall error well below 50 °C in a temperature range from 400 °C to 1200 °C.

Keywords: Thermography; Infrared imaging; Temperature emissivity separation; Fire testing; Surface temperature measurement; Emissivity change; Thermal degradation

Highlights

- 2C pyrometry allows for exceptional temporal and spatial resolution for in-situ temperature measurements of thermally degrading materials
- Multi-layer radiometric transfer modelling takes the test configuration into account
- Filter selection is tailored to fire tests
- Comprehensive image post-processing combined with dedicated calibration measurements help to significally reduce errors in temperature measurements
- Sample emissivity for composites show temperature dependency generally decreases as the temperature increases

5.1 Introduction

Polymer matrix composites (PMC) are widely employed in the transportation sector and continue to replace traditional metal parts. Despite their versatile mechanical properties and the significant weight reduction they allow, important challenges must be addressed for applications at high temperature. Under these conditions, thermal degradation results in rapid changes in the material mechanical, thermal and optical properties. For aerospace or naval applications, these materials are subjected to certification testing where they are exposed to a calibrated heat source, typically a heating coil, a lamp, or a flame. For components located close to fire hazards, the tests involve a pilot flame fueled by either propane or oil. Predicting and understanding the thermal degradation mechanisms of PMCs requires precise knowledge of the material temperature, a quantity difficult to obtain experimentally under the conditions of certification fire tests. Optical techniques such infrared (IR) thermography can provide high spatial resolution, non-intrusive measurements but require careful calibration to yield accurate results, a time-consuming step not always implemented in practice. Here we introduce a novel two-color IR camera calibration approach that includes optical path modelling and geometrical corrections, drastically reducing the error budget associated with optical thermography, thus bridging the gap with point-based thermocouple (TC) measurements.

Regardless of the heat source used in fire testing, radiative heat transfer towards the sample is the main process that initiates and drives the PMCs thermal degradation [23, 165–167]. The specific experimental conditions affect both, how the material degrades and how surface temperature can be measured by IR cameras. Two important factors are hence the spectral dependency of the sample absorptivity with respect to the heat source and the spatial heterogeneity in the heat source

itself. Depending on the type of test apparatus, the latter may be less pronounced (cone calorimeter) or significant (high temperature lamp). The case of samples that ignite is even more complex as the surface flame is a secondary source of radiation and the emission pattern as a whole is affected. Numerical models to predict the thermal degradation heavily rely on sample emissivity and absorptivity that determine the energy distribution and heat loss [23, 168]. Stoliarov et al. [123] reported uncertainties of ±50 % for the absorption coefficient and ±20 % for the reflectivity. This may be partly attributed to the design of their model, where all radiative properties are kept constant, although most of the material parameters are temperature dependent and change as it degrades. Studies on the surface reflectance and absorptance of several materials [169], polymers in particular [170], show that the spectral characteristics of the heat source, not only its nominal temperature, affect how much heat is actually absorbed by the exposed sample. The flame radiation of hydrocarbon fuels is located in the infrared spectrum [171], where most polymers commonly have a high absorptance with little variation. However, sample emissivity and absorptance might still change as the material decomposes [172]. The radiation absorbed by a sample causes its temperature to change, and the measurement of this change is essential to understand the outcome of many fire test. In large-scale certification setups, this measurement is commonly limited to a few thermocouples (TCs) at defined positions, allowing limited insights [7] and coming with their own experimental challenges [173]. Meanwhile, several bench-scale setups have been developed [100, 117, 122, 127, 174–176] that monitor the spatial and temporal temperature evolution through IR thermography at the sample back face, i.e. away from the heat source. The sample temperature is then obtained from an inversion of Plank's law, which requires the sample emissivity as input. Since this value is inherently difficult to assess experimentally, it is practical to assume it constant over the whole test period, taken either from the literature or measured before or after testing. However, the spectral emissivity of most materials varies with temperature, wavelength, and surface conditions. Thermal degradation affects all three variables and therefore the apparent temperature obtained by single-wavelength pyrometry may be seriously in error [177]. In several reports dealing specifically with PMCs [116–118, 127, 178] these significant contributions to the radiometric model are neglected, leading to measurements values being reported as overly precise. A potential approach to overcome this problem is two-color (2C) – or ratio – pyrometry. This technique is commonly used to measure soot concentration [132, 179], temperature evolution in turbulent flames [180], or for flame-wall impingement studies [181–183]. The basic idea is to measure the sample radiance through two different narrow spectral bands and then use the signal ratio to calculate the object temperature [184–186]. For thermally degrading materials such as PMCs, 2C IR pyrometry has not yet been implemented to yield precise assessment of the surface temperature with high spatial and temporal resolution. Moreover, the question of radiometric precision in one and two color pyrometry warrants a careful review in the context of fire testing.

In this paper, we present a rigorous 2C pyrometry framework, covering hardware selection, camera calibration and post-processing, and implement it to measure the backside temperature of thermally degrading materials. The experimental campaign covers metallic samples and PMCs commonly used in aerospace and transportation applications. We discuss the potential sources of noise and error associated with the IR acquisition for rapidly degrading materials such as PMCs. We also develop a radiation model and assess the validity of the assumptions underlying 2C pyrometry and how they affect the accuracy of the surface temperature and emissivity measurements. This multi-step thermography image processing scheme offers a comprehensive approach to accurately study rapidly degrading materials under intense flame attack.

5.2 Material and methods

5.2.1 Sample panels

Two types of carbon fibre and one type of glass fibre reinforced polymer (CFRP and GFRP, respectively) composite panels were tested, along with stainless-steel samples, to cover effects of emissivity and thermal conductivity. The two SAE 304 stainless steel panels measured 305 mm × 305 mm, with a thickness of 1.6 mm. Concentric circles with 10 mm radial spacing were marked onto the backside, as reference for welding thermocouples (TC). All metal panels were used in the condition they were received in and do not display significant surface wear. Two CFRP panels with phenolic CYCOM 2400-1M resin and T650 carbon fibers (8 harness satin) were fabricated with four plies in $[0/+45/-45/0]_S$ orientation. Type K TC with a diameter of 0.08 mm, coated with a thin layer PFA insulation to prevent electrical conduction with the material, were embedded in-between plies, as well as on each face to measure the temperature evolution throughout the sample thickness. The panels measured 65 mm×300 mm and were 1.65 mm thick. CFRP samples were also manufactured with epoxy resin as 25.4 mm × 305 mm wide coupon strips and used for flame calibration and some verification testing. A glass-fibre panel with phenolic resin (GF-Ph), 35 mm × 300 mm, was used for emissivity measurements.

5.2.2 Fire test configuration

The top view of the experimental configuration used to expose the material samples to open flames is shown in Fig. 5.1. It is representative of fire certification tests where a vertically mounted sample is exposed to a horizontally impinging flame [9, 37]. An environmental chamber connected to a fume hood, with a volume of approximately one cubic meter, houses the sample mount and the burner. Samples with an area smaller than the flame cross section were shielded from both sides with insulating ceramic fibre boards (CeraMaterials), with a recessed step, to prevent the flame

from wrapping around the specimen while maintaining the exposed surface uniform, as visible in Fig. 5.1. The coupons are clamped on the bottom and top to vertically align the center of the sample with the flame. The mounting frame can be moved horizontally to control the distance to the burner exit. The chamber provides optical view ports on all four sides, with the main visualizations carried out from the back side using IR and visible cameras. A DSLR camera (Nikon D750) is also used to provide complementary imaging.

5.2.3 Gas and oil burner

A laboratory-scale kerosene burner [146] was used to generate conditions representative of the large-scale testing of aerospace components [46]. Jet fuel-A is atomized through a 60° hollow-cone bypass nozzle (Delavan 33769-2 with adapter no. 17147). Adjusting the inlet and bypass pressure allows the desired fuel flow rate, and hence burner power, to be attained. The oxidizer is laboratory compressed air, regulated with an Omega FMA5400 flow controller, allowing precise control over the flame chemistry. The air passes through a stream stator with 25 blades at 15° orientation to enhance mixing with the fuel droplets and increase the evaporation rate. This swirling flame configuration was developed to mimic large-scale burners, such as the NexGen burner [74, 158], prescribed in certification testing standards [9, 37]. A commercial off-the-shelf gas blow torch (Bullfinch No.1270) was used to generate propane flames, motivated by its use in the literature for similar fire resistance investigations [81, 100, 187]. The burner has been modified with a collar around the air inlet to control the oxidizer amount and therefore the flame chemistry.

5.2.4 Temperature, emissivity, and high-speed infrared thermography measurements

Type K TC were used to measure the sample temperature, with the probe design adapted to the sample type and test setup. These measurements served as second independent measurements for validation and comparison against IR thermography. Probes that measured the temperature on the sample back (cold) face were not in direct contact with the flame and thus needed no protective coating to prevent catalytic reactions or surface degradation. For the steel samples, sturdy type K thermocouples (1.628 mm in diameter) were welded at different radial distance from the sample centre to ensure proper contact throughout the tests. The radius was increased in steps of 10 mm. Most of the composite samples had thin (0.08 mm) PFA-coated type K TC placed in-between each ply, with their beads slightly shifted relative to their neighbours, allowing the temperature gradient throughout the sample thickness to be measured without inducing local deformation. All thermocouples, except for those irreversibly integrated in composite panels, were tested prior to use with a dry-well (Fluke Calibration 9140).

The multispectral (MS)-IR camera (Telops FAST-M350) was configured with a 50 mm lens and an

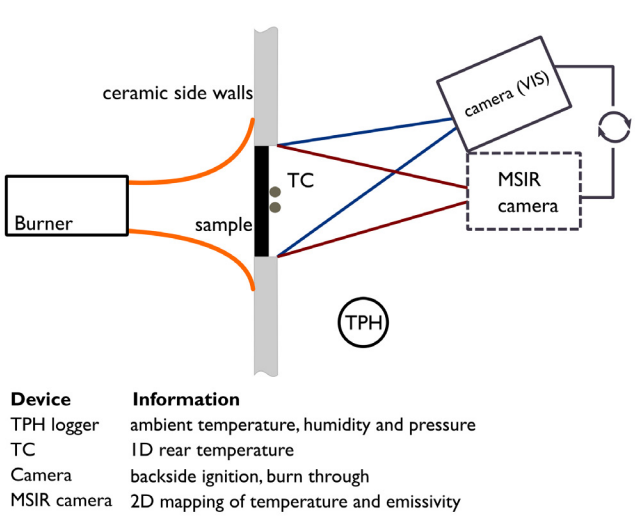

Device	Information
TPH logger	ambient temperature, humidity and pressure
TC	1D rear temperature
Camera	backside ignition, burn through
MSIR camera	2D mapping of temperature and emissivity

(a)

(b)

Figure 5.1 a) Schematic depiction of the experimental setup. The test rig is comprised of the following main parts: the exchangeable burner, the sample mounting grips and ceramic shields, exhaust and air entries and optical ports on four sides. b) Photograph of the propane flame impinging on a steel sample.

eight-position fast-rotating filter wheel to record different wavelength bands (Fig. 5.2). The focal plane area (FPA) of the indium antimonide (InSb) detector is 640 px × 512 px with a detector pitch of 15 µm. The camera numerical aperture is F/3. The mid-wave IR filter configuration is listed in Tab. 5.1. The optical density (OD) indicates the amount of energy blocked by a given filter. In the case of the neutral density filters in position FW#2 and FW#3, the transmission is evenly reduced across their spectral range to 2.5 % and 0.1 %, respectively. The filters FW#7 and FW#8 are so-called 'through-flame' filters because they limit contributions from combustion gases and ensure that the radiance contribution received by the sensor is dominated by the contribution from the hot surface. Software-defined automatic exposure control (AEC) was used to ensure proper exposition during strongly varying conditions and fast recording rates. The MS-IR camera was positioned perpendicular to the sample backside and the windows of the test chamber were unmounted to limit ray path obstruction. Radiance calibration measurements were performed with a Fluke Calibration 4181 black body.

The emissivity of the samples is expected to change as the samples thermally degrade and their surface alters. To compare the initial and final emissivities obtained through IR measurements against alternative techniques, CFRP and GFRP samples have been analysed in their pristine state and post-fire. The absorptivity of selected regions on the samples were measured using a SOC100 Hemispherical Directional Reflectometer (HDR) (Surface Optics Corporation) coupled with a FTIR

Spectrometer at a sample temperature of 20 °C. The incident polar angle is fixed at 10°, near normal incidence. Kirchhoff's law (absorptivity α equals emissivity ε) and assuming the transmissivity of an opaque material ($\tau = 0$) enable the link between the hemispherical directional reflection factor ρ and the emissivity ε for a given wavelength:

$$\varepsilon(\lambda) = 1 - \rho(\lambda)\,. \tag{5.1}$$

The total directional sample emissivity was then calculated from the ratio between the luminance $L(\lambda)$ radiated from the sample and the luminance $L^0(\lambda)$ from a black body integrated over the spectral range from 2.0 µm to 30.2 µm.

$$\varepsilon = \frac{\int_{\lambda_1}^{\lambda_2} L(\lambda)\,\mathrm{d}\lambda}{\int_{\lambda_1}^{\lambda_2} L^0(\lambda)\,\mathrm{d}\lambda}\,. \tag{5.2}$$

Table 5.1 Filter wheel configuration of the MS-IR camera.

Position	Description	Spectral Range [µm]		OD	Transmittance [%]	Temperature Range [°C]	
FW#1	Sapphire window (Broadband)	1.5	6.00	N/A	100	10	338
FW#2	Neutral density filter, OD 1.6	1.5	6.00	1.6	2.2	207	1500
FW#3	Neutral density filter, OD 3	1.5	6.00	3.0	0.1	539	1500
FW#4	NPB-3010-40 (H2O)	2.98	3.03	N/A	70	408	1440
FW#5	NBP-4450-150 (CO2 and CO)	4.31	4.61	N/A	70	155	850
FW#6	NBP-3700-110 (Through flame)	3.65	3.76	N/A	70	225	1194
FW#7	NP-3800-040 (Through flame)	3.78	3.82	N/A	70	297	1500
FW#8	NB-3950-040 (Through flame)	3.94	3.98	N/A	60	282	1500

5.3 Theory and calculation

The radiative power of a blackbody $L_\sigma(\sigma, T)$, an ideal material with an emissivity ε equal to unity at thermal equilibrium, depends on temperature and wavenumber as described by Planck's law:

$$L_\sigma(\sigma, T) = 2 \cdot 10^8 \cdot hc^2\sigma^3 \frac{1}{\exp\left(\frac{100hc\sigma}{k_\mathrm{B}T}\right) - 1} \left[\mathrm{W/(m^2\,sr\,cm^{-1})}\right] \tag{5.3}$$

with $L_\sigma(\sigma, T)$ the spectral radiance, σ the wavenumber [$\mathrm{cm^{-1}}$], T the temperature [K], h the Planck constant, c the speed of the light and k_B the Boltzmann constant. Integrating the spectral radiance over all wavenumbers yields the well-known Stefan-Boltzmann law, but for our application, only

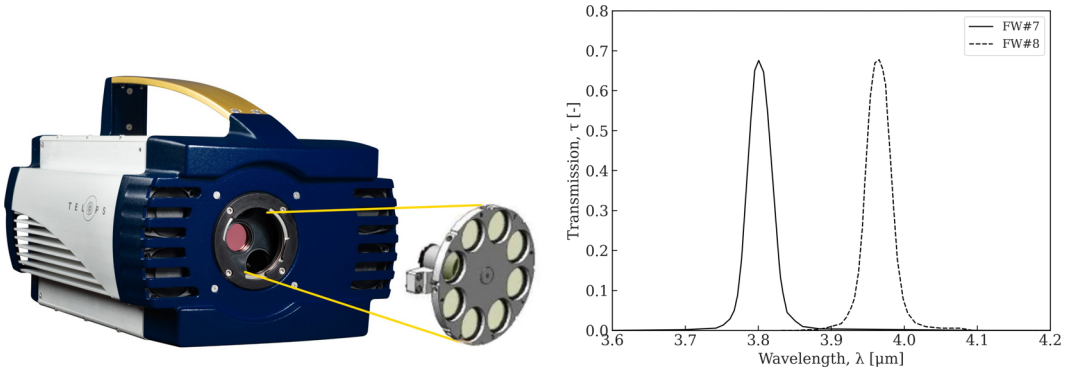

(a) (b)

Figure 5.2 (a) The Telops MSIR camera has a fast-rotating eight-position filter wheel. (b) Transmittance curves for the through-flame filters (cf. Tab. 5.1) provided by the camera manufacturer: NP-3800-040 (FW#7) and NB-3950-040 (FW#8).

the spectral range of the camera for a given optical configuration is of interest. The in-band radiance (IBR) for a given filter from a cut-on, σ_{low} to cut-off σ_{high} wavenumber is mathematically linked to the black-body temperature by:

$$\mathrm{IBR}(T) = \int_{\sigma_{\mathrm{low}}}^{\sigma_{\mathrm{high}}} L_{\sigma}\left(\sigma, T\right)\, \mathrm{d}\sigma \left[\mathrm{W}/(\mathrm{m}^2\,\mathrm{sr})\right] \tag{5.4}$$

A key feature of Eq. (5.4) is that the function is strictly monotonic, thus allowing only one value of IBR per temperature for a given optical configuration. The radiometric camera calibration provides this unique link between an incoming radiance signal and a given black-body temperature. Through this relation, the radiometric temperature measured by a calibrated thermal infrared camera assumes an ideal black-body (BB) radiation $L_{BB}(\sigma)$, from which real materials typically deviate, with the degree of deviation accounted for by their specific emissivity $\varepsilon(\sigma)$. This value must be obtained experimentally or from the literature to yield the corrected spectral radiance $L(\sigma) = L_{BB}(\sigma)\varepsilon(\sigma)$. As the emissivity is a surface property, the important change in composition and morphology occurring as composite materials degrade has a direct effect on ε. For metallic samples, the formation of oxide layers and changes in surface finish may present an important source of error [188, 189]. In addition, spectral variations and temperature dependency make emissivity a material property that is difficult to assess, but easily changed by other material properties.

Two-color (2C) pyrometry overcomes some of the challenges associated with obtaining accurate emissivity data. Instead of assuming an overall constant emissivity, it is only assumed constant between two narrow and closely located wavebands ($\sigma_{1,low}$ to $\sigma_{1,high}$, and $\sigma_{2,low}$ to $\sigma_{2,high}$). The IBR measured by the camera for a given spectral bands becomes:

$$\mathrm{IBR}_{\sigma_i}(T) = \int_{\sigma_{i,\mathrm{low}}}^{\sigma_{i,\mathrm{high}}} L_{\sigma_i}\left(\sigma_i, \mathrm{T}\right)\, \mathrm{d}\sigma \left[\mathrm{W}/(\mathrm{m}^2\,\mathrm{sr})\right] \quad \text{with } i \in \{1,2\}. \tag{5.5}$$

Although the relation between temperature and IBR is nonlinear and may even vary depending on the spectral filter, it remains monotonic. Therefore, the ratio of the two IBR signals is monotonic as well. 2C pyrometry employs this mathematical property to eliminate the emissivity-dependance and to retrieve the true temperature of a material based on the IBR ratio.

5.3.1 Radiation model

The processing of IR images to extract temperatures requires proper assessment of the optical path (Fig. 5.3) and of the factors influencing the total incident spectral radiance $\mathrm{L}_{\sigma_i}(\sigma_i,\mathrm{T})$ in Eq. (5.3) arriving at the detector in the different filter band for a given experimental setup. Phenomenologically, the optical path is described with a multi-layer radiative transfer model. The individual layers of the model for the configuration where a camera images the back (cold) face of a thin sample exposed to an open flame are depicted in Fig. 5.3. It includes contributions from the background (bkg) reflected onto the sample (s), the pilot flame (fl) as well as the atmospheric (atm) and filter (ft) transmission characteristics. The radiative properties of each layer are derived according to the first law of thermodynamics, where absorptivity, reflectance, and transmittance of a material sum to unity, $\alpha+\rho+\tau=1$. Furthermore, assuming diffusive gray body behavior, the relation can be rewritten based on Kirchhoff's law, as the absorptivity directly equals the emissivity, $\alpha_s = \varepsilon_s$. The radiative properties of the contributing layers are summarized in Tab. 5.2.

Table 5.2 Radiative contributions from the model components shown in Fig. 5.3.

Model component	negligible quantity	energy balance	contribution
Background	$\tau = 0$	$\alpha = 1$	$\varepsilon_{\mathrm{bkg}} = 1$
Atmosphere	$\rho = 0$	$\tau + \alpha = 1$	$\varepsilon_{\mathrm{atm}} = 1 - \tau_{\mathrm{atm}}$
Filter	$\rho = 0$	$\tau + \alpha = 1$	$\varepsilon_{\mathrm{ft}} = 1 - \tau_{\mathrm{ft}}$

The radiance $\mathrm{L}_1(\sigma,\mathrm{T})$ close to the sample surface is determined by the sample spectral emissivity $\varepsilon_\mathrm{s}(\sigma)$ and temperature $\mathrm{T_s}$ as well as by potential background contributions $\mathrm{L_{bkg}}$ reflected to the sample:

$$L_1\left(\sigma, T\right) = \varepsilon_\mathrm{s}\left(\sigma\right) L_\mathrm{s}\left(\sigma, T_\mathrm{s}\right) + \left(1 - \varepsilon_\mathrm{s}\left(\sigma\right)\right) L_\mathrm{bkg}\left(\sigma, T_\mathrm{bkg}\right) \left[\mathrm{W}/(\mathrm{m}^2\,\mathrm{sr}\,\mathrm{cm}^{-1})\right] \tag{5.6}$$

The atmosphere can alter the total radiance received at the detector, especially if species with strong absorbance bands in the IR spectrum are present, such as water vapour and carbon dioxide:

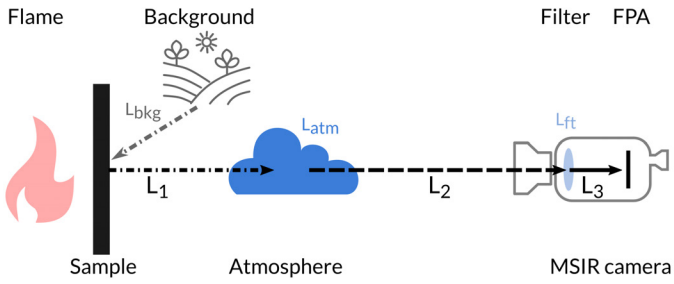

Figure 5.3 Schematic representation of the ray path from sample to detector. The direct line of sight signal is affected by the filter characteristics and by potential contributions from the background and the atmosphere. The filter is installed in the internal wheel of the multi-spectra IR camera.

$$L_2(\sigma, T) = (1 - \tau_{\text{atm}}(\sigma))\, L_{\text{atm}}(\sigma, T_{\text{atm}}) + \tau_{\text{atm}}(\sigma)\, L_1(\sigma, T) \left[\text{W}/(\text{m}^2\,\text{sr}\,\text{cm}^{-1})\right] \tag{5.7}$$

The camera band-pass filters characteristics finally determine the total spectral radiance incident on the camera detector:

$$L_3(\sigma, T) = (1 - \tau_{\text{ft}}(\sigma))\, L_{\text{ft}}(\sigma, T_{\text{ft}}) + \tau_{\text{ft}}(\sigma)\, L_2(\sigma, T) \left[\text{W}/(\text{m}^2\,\text{sr}\,\text{cm}^{-1})\right] \tag{5.8}$$

In the case of an external filter wheel and un-cooled camera used in other setups [116, 117, 132, 181, 190], additional contributions from the environment reflected by the filter outside of its transmissivity range would have to be considered. In our experiments, the filters are installed in an internal wheel located within the cooled MS-IR camera (Fig. 5.2a), which renders the radiation reflected negligible relative to the direct line-of-sight signal [133]. Eq. (5.8) contains seven unknowns and integrating over the spectral range of the camera adds two more parameters, while only a single value, the total integrated band radiance of the camera IBR_{cam} is accessible. Radiometric calibration, filter specifications and well-justified assumptions allow the model to be reduced to two unknowns, the sample temperature and emissivity. First, the radiometric camera calibration from the supplier already considers the band-pass filter response (Fig. 5.2b) in the spectral and temperature region of interest and provides a direct access to the incoming radiance to the camera:

$$\text{IBR}_{\text{cam}}(T) = \int_{\sigma_{\text{low}}}^{\sigma_{\text{high}}} L_3(\sigma, T)\, d\sigma \left[\text{W}/(\text{m}^2\,\text{sr})\right] \tag{5.9}$$

Secondly, band-pass filters are chosen to be transparent to the atmosphere at short distances (<1 m) from the target and the camera is placed at 85 cm from the sample surface. It is thus assumed that both, $\tau_{\text{atm}}(\sigma)$ and $\tau_{\text{ft}}(\sigma)$, are equal to unity over the full spectral range. With this, $L_3(\sigma,T) = L_2(\sigma,T)$,

and $L_2(\sigma,T) = L_1(\sigma,T)$, and Eq. (5.9) becomes:

$$\mathrm{IBR}_{\mathrm{cam}}(T) = \int_{\sigma_{\mathrm{low}}}^{\sigma_{\mathrm{high}}} L_1(\sigma, T)\, \mathrm{d}\sigma \left[\mathrm{W}/(\mathrm{m}^2\,\mathrm{sr})\right] \tag{5.10}$$

With a band gap as small as 0.04 µm for FW#7 and 0.08 µm for FW#8, emissivity is assumed constant over these two spectral ranges. With this important simplification, $\varepsilon_s(\sigma) = \varepsilon_s$ and Eq. (5.10) now becomes:

$$\mathrm{IBR}_{\mathrm{cam}}(T) = \int_{\sigma_{\mathrm{low}}}^{\sigma_{\mathrm{high}}} \left[\varepsilon_s L_s(\sigma, T_s) + (1-\varepsilon_s) L_{\mathrm{bkg}}\left(\sigma, T_{\mathrm{bkg}}\right)\right] \mathrm{d}\sigma \left[\mathrm{W}/(\mathrm{m}^2\,\mathrm{sr})\right] \tag{5.11}$$

The surface emissivity ε_s also determines the relative importance of the reflected background radiance, but this contribution may be disregarded if the sample temperature is significantly higher than its background, which is generally the case in the fire certification test considered here. As a rule of thumb, the background radiance should be less than one percent of the sample radiance [131]. As a first estimate, we assumed an average background temperature of 300 K, an emissivity of $\varepsilon = 0.6$ for metal samples, and $\varepsilon = 0.8$ for composite samples. Aiming for a signal-to-noise ratio of 100, for the filters with a centre wavelength $\lambda = 3.7$ µm, the minimum sample temperature above which the background contribution can be disregarded is approximately 440 K (167 °C) for metals and 400 K (127 °C) for composite samples. Both temperature values lie well below the minimum temperature of the filters FW#7 and FW#8 used for our tests (cf. Tab. 5.1). With these assumptions the transfer model from Eq. (5.11) can be further simplified:

$$\mathrm{IBR}_{\mathrm{cam}}(T) = \varepsilon_s \times \int_{\sigma_{\mathrm{low}}}^{\sigma_{\mathrm{high}}} L_s(\sigma, T_s)\, \mathrm{d}\sigma \left[\mathrm{W}/(\mathrm{m}^2\,\mathrm{sr})\right] \tag{5.12}$$

Finally, the assumption that led to Eq. (5.11) is generalized. Since the two filters bands are close to each other by design, the sample emissivity is not only considered invariable in the spectral range of each filter, but also assumed to be the same for both filters. The initial radiation model with nine unknowns can thus be reduced to a system of only two unknowns, $\mathrm{IBR}_{\mathrm{filter,\,1}}$ and $\mathrm{IBR}_{\mathrm{filter,\,2}}$, which are both experimentally accessible. Applying the 2C pyrometry principle, we use Eq. (5.12) to form the IBR signal ratio for two filters, an expression independent of the sample emissivity:

$$r(T_s) = \frac{\mathrm{IBR}_{\mathrm{filter1}}}{\mathrm{IBR}_{\mathrm{filter2}}}\ [-] \tag{5.13}$$

The monotonicity of Eq. (5.12) ensures that Eq. (5.13) is also monotonic and hence that any given temperature for a sample with emissivity ε_s corresponds to a distinct IBR ratio value. Simulated

IBR-temperature curves for FW#7 with different ε are shown in Fig. 5.4. Using an exemplary value of 50 kW/(m^{2}sr) (red line), it becomes immediately apparent that errors in emissivity can easily result in wrong temperature readings when relying on single color (1C) pyrometry. Wrongly assuming an emissivity of 0.8 for a sample with ε= 0.6, the sample temperature is underestimated by 53 °C in our example.

The practical implementation of the 2C techniques is referred to hereafter as the Temperature-Emissivity-Separation (TES) algorithm and relies on several steps. First, the IBR ratio in Eq. (5.13) for two different filters is simulated by numerically solving Eq. (5.12) over the respective filter bands and over a temperature range of interest. Then, the IBR ratio obtained from the actual camera readings $IBR_{filter1}$ and $IBR_{filter2}$ is compared with the simulation to identify the corresponding sample temperature. In a last step, this sample temperature can be used to calculate the corresponding spectral radiance for a black body based on Eq. (5.12) and using the information from a single filter channel. This allows to calculate the sample emissivity:

$$\varepsilon_{s,i} = \frac{\mathrm{IBR}_{\mathrm{filter,i}}}{\int_{\sigma_{i,\,\mathrm{low}}}^{\sigma_{i,\,\mathrm{high}}} L_s\left(\sigma, T_s\right)\,\mathrm{d}\sigma}\,[-]\,. \tag{5.14}$$

Because the IBR ratio, $r(T_s)$ is built pixel-wise, the TES algorithm allows to obtain sample temperature and emissivity mappings with the size and resolution determined by the exposed detector area and distance to the sample.

5.3.2 Sources of error

The principle of 2C pyrometry allows to separate temperature and emissivity calculations for the same scene using two images acquired with different band-pass filters. The apparent simplicity of this technique to obtain both quantities from the same measurement comes with several key requirements for the acquired IR signal that are implied by the choice of radiation model and assumptions described in Sec. 5.3.1. Any deviation from the ideal case contributes to the overall error budget.

Starting right-to-left with respect to Fig. 5.3, three basic limitations are linked to the camera hardware: mechanical precision, attainable speed of the fast-rotating filter wheel and minimal detector noise. The mechanical transition from one filter to another induces a parallax error because of the bore-sight displacement. A fine co-registration is crucial for pixel-based IBR calculations, otherwise small features are more prone to accumulate errors at low spatial resolution and a dedicated post-processing step is recommended. For the metal and PMC samples tested in this study, the focus was set on the entire sample region visible or on a larger sub-region so that the resolution

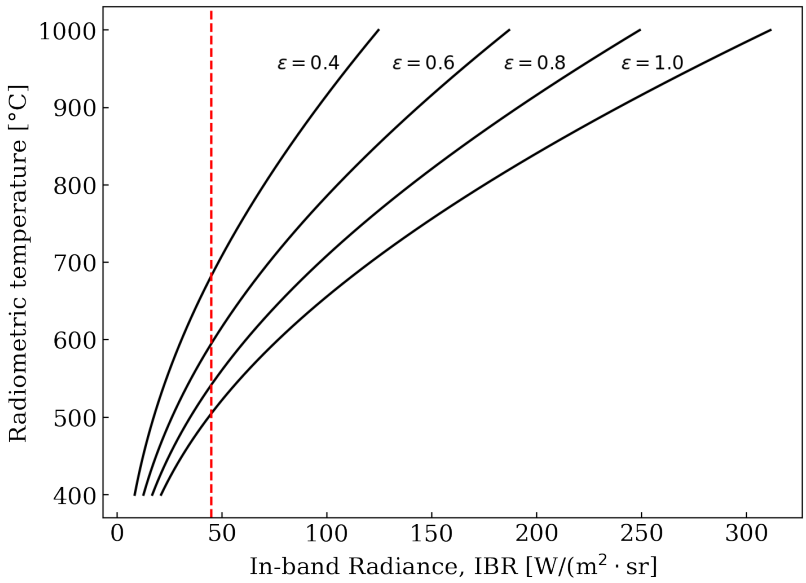

Figure 5.4 Simulated temperature curves for filter FW#7 (cf. Tab. 5.1) as a function of IBR for different sample emissivities ε demonstrating the monotonous relationship between. The red line highlights was added as an example to illustrate that a wrong emissivity value results in wrong temperature readings.

was never below $4\,\mathrm{mm\,px^{-1}}$. The filter wheel mechanics are responsible for filter positioning and image alignment, while ensuring stable and fast rotation. A critical potential source of error in fire testing, where temperature and material properties can change quickly, is temporal resolution. In this situation, one is typically interested in following rapid changes in temperature as, for example, during the first few tens of seconds when a PMC is heated and ignited. To accurately track the temperature, the delay caused by the filter wheel turning needs to be small enough for the camera IBR signal to be considered invariant between subsequent acquisitions. To this end, the camera acquisition frame rate is synchronized with the filter wheel rotation and the filters of interest are mounted in adjacent positions. The IBR-ratio is calculated for the successive frames for each filter wheel rotation where any signal variation contributes to the overall error budget. The selection of an appropriate acquisition frequency is thus an essential part of the experimental design. The frame rate is limited by a combination of window size, exposure time, and the fastest (mechanically) attainable wheel speed.

The temporal noise at the detector impacts the pixel-wise error for each frame and shall be limited by the camera shot noise. For this requirement, the camera manufacturer usually refers to the noise equivalent temperature difference (NETD) at room temperature. The NETD can be expressed in terms of radiance with the noise equivalent differential in-band radiance (NEdIBR). This formulation provides a useful performance figure for each filter within a specific temperature range as to

the amount of change in radiance needed to equal the system noise. High-quality band-pass filters with a narrow gap and sharp cut-on and cut-off characteristics increase the radiometric accuracy. Neglecting test specific error sources, the ultimate performance limit of 2C pyrometry is therefore governed by the camera hardware (detector, filter, rotating wheel) and the resulting camera specific NEdIBR.

The challenge to quantify both temperature and emissivity becomes immediately apparent when considering a small error in one of the spectral bands. This error can be caused by a calibration inaccuracy for a filter, by variations of the radiance signal within a filter's spectral band or in-between acquisitions. Using the spectral bands for filters FW#7 and FW#8 used in our experiment (cf. Tab. 5.1), the calculated temperature variation due to an error of 1 % or 3 % in the spectral band of filter FW#7 is simulated in Fig. 5.5. At 500 °C, a common upper limit for backside temperatures of PMC fire testing, the temperature is underestimated by approximately 43 °C and more than 140 °C, for 1 % and 3 % filter errors, respectively. For PMCs, the temperature regime around 500 °C is critical, as many important processes occur, such as resin decomposition, degradation of the fibre sizing agent and fibre oxidation [81, 113]. Aiming for a measurement accuracy of 10 °C for each contributor to the overall error budget requires the radiance variation between two filters to be as low as 0.25 %. The same requirement applies to the radiometric accuracy of the camera calibration.

Finally, the samples are required to behave as gray bodies with an emissivity that is independent of wavelength, temperature, and solid angle in both filter bands, $\varepsilon_s(\lambda, T, \Theta) = \varepsilon_s$. The crux of the problem for PMCs is that the "body" thermally degrades into several different materials, as shown in Fig. 5.6 from a partially burnt carbon-fibre epoxy sample exposed for 30 s to a kerosene flame calibrated to 116 kW/m^2, representative for aerospace large scale fire tests [9, 37]. Already after this short flame exposure, distinct zones with likely different emissivities can be observed on the back side as the resin partially burns and decomposes. For steel, the surface undergoes an important emissivity change due to oxidation but once the oxide layer is established the temperature dependence of the target emissivity is sufficiently subtle and can usually be neglected [191].

In general, the total emissivity for many materials shows a strong temperature dependency. Additionally, the change of emissivity with temperature is often correlated to its change with wavelength. A surface temperature rise for a sample means also that its emission is shifted to shorter wavelengths. In general, $\varepsilon(T)$ increases with T for conductors and decreases for insulators [192]. Although electrically conductive, an emissivity decrease with temperature has also been reported for carbon fibre composites [179, 193, 194]. Some authors [179, 192, 193] propose a second-order polynomial fit for the $\varepsilon(T)$ relation, with the coefficients based on literature data that remain valid only within a strict temperature range. Although such a fit certainly does not provide much insight

into the physics at play it allows for a simple judgment method to compare the data presented in Sec. 5.5.4 against similar experimental studies that attempt to take into account the temperature dependence of emissivity.

5.4 Image postprocessing

The TES algorithm uses the IR raw signals from filter channel FW#7 and FW#8 to calculate a pixel-wise IBR ratio. This ratio is then used to retrieve the corresponding radiometric temperature from look-up tables. The post-processing accounts for the simplifications that have led from Eq. (5.8) to Eq. (5.12) by dedicated measurement blocks. The MS-IR camera records the IBR signal per pixel and registers the sequences in a proprietary Telops format (.hcc). Signal post-processing was performed using Matlab® 2019 and the Python programming environment (Python Software Foundation). The analysis workflow is depicted in Fig. 5.7 with each independent measurement block being grouped by a dashed line: radiance correction, temperature calibration, and emissivity evaluation. The filter-wise radiance correction are important, but independent steps when measuring thermally degrading complex materials. The calibration step allows a "proof of concept" and helped us to compare the TES algorithm results against independently measured values, relying on thermocouples.

Part of the filter-wise correction account for the radiance of the detector area actually illuminated. This step is necessary as the camera calibration by the manufacturer is based on black body measurements with all sensor pixels exposed to a similar radiant flux. For tests with composite coupons strips, the camera field of view (FOV) was chosen to cover the vertical sample length that corresponds to the diameter of the stagnation zone of the impinging flame. The numerical simulations based on Eq.(5.12) rely on the manufacturer calibration of the camera for each filter which is based on a homogeneous illumination of each sensor pixel. Black-body measurements are used to create a look-up table that relates the number of illuminated pixels to a suitable radiance correction factor. It is important to note that each filter needs to be corrected independently. The calibration block tests, the gray body assumption as well as the temperature and emissivity mapping are compared against HDR and TC measurements. Since the HDR emissivity measurements were performed on $25.4\,\text{mm} \times 25.4\,\text{mm}$ cut-out samples after fire exposure, the TES algorithm used only the respective regions of interest (ROI) of the same samples on a subset of frames at the end of acquisition. The emissivity thus calculated was then averaged over the sub-region and frame set. In a similar manner, temperature mapping in a small pixel region at the estimated TC position was extracted over all frames and compared against the TC data.

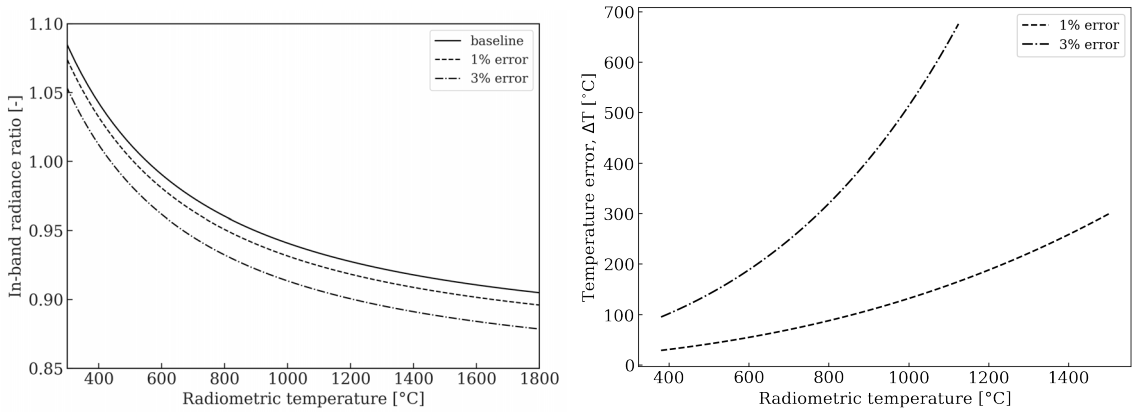

(a) (b)

Figure 5.5 (a) Simulated in-band radiance ratio (IBR) signal for filters FW#7 and FW#8 over the temperature range of interest. A deviation of 1 % and 3 % from the baseline signal is shown. (b) Assuming an otherwise perfect measurement system, these deviations result in large errors especially at high temperatures.

5.5 Results and discussion

5.5.1 Filter-wise radiometric correction

In a first step, a gas flame (2.7 slpm C_3H_8 and 8 slpm oxidizer mixture consisting of 60 % O_2, diluted with CO_2) was used to heat a 305 mm × 305 mm stainless-steel sample with thermocouples welded at different radial distances from the stagnation point on its backside. A rich flame (Φ=1.3) is used to create a homogeneously heated zone with a temperature maximum below or equal to 500 °C that can be recreated with the black-body. The IR image of the steel back face and the temperature curves measured by the TC in the FOV are shown in Fig. 5.8. The pixels above the filter specific radiance threshold (Fig. 5.8a) corresponds approximately to a circular zone with a diameter of 75 mm and an area of 35 000 px^2. Fig. 5.8b shows the corresponding minimum temperatures for both filters as horizontal lines. Similar tests were repeated with flames of different diameters.

The calibration starts by comparing the internal camera calibration against a black-body (set at 500 °C) with a similar apparent temperature and FOV as the exposed sample during the experiment. To this end, the black-body was partially shielded, with the size of the illuminated area (IA) increased from 4 % to 58 %. The IA represents the fraction of total pixels 640 px × 512 px contributing to the total signal. The results are listed in Tab. 5.3. Radiance correction (rc) is the inverse of the radiance ratio between the full aperture and a given IA. The IA-radiance relation is highly nonlinear, as can be seen in Fig. 5.9. For instance, an IA of 10 % yields an incoming signal through for filter FW#7 that is only 91 % of the expected radiance signal for a body of the same temperature

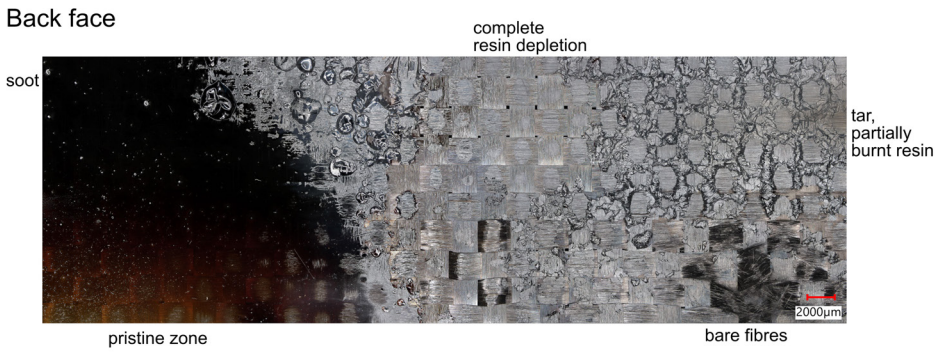

Figure 5.6 Back face (BF) of a carbon fiber epoxy sample strips after a 30 s fire test using a kerosene flame, revealing highly variable surface properties. The sample strip shown is 25.4 mm × 80.0 mm.

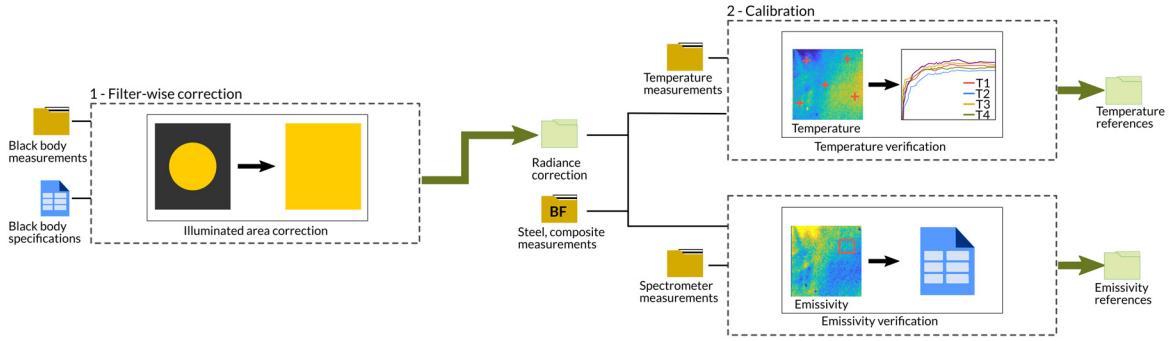

Figure 5.7 Diagram of the different steps of the 2C thermography post-processing technique. Each section is linked to a dedicated experimental design and test campaign.

and emissivity. As a result, without correction temperatures will be underestimated and emissivity will be overestimated, and hence a geometrical correction is essential for accurate 2C pyrometry measurements over a surface with steep temperature gradients.

5.5.2 Post-fire emissivity measurements

The in-situ emissivity values obtained with the TES algorithm are compared against an independent measurement technique implemented at room temperature following fire exposure. A kerosene flame (calibrated to 116 kW/m^2) was used to burn a carbon-fibre phenolic (CF-Ph) and a glass-fibre phenolic (GF-Ph) sample, both with integrated thermocouples, as well as a stainless-steel plate with welded thermocouples (Fig. 5.10) for 5 min. After the test, square samples were cut from selected regions within the camera FOV to measure their averaged spectral emissivity on the back face with a reflectometer.The results for the three different materials and subregions (Fig. 5.10) are listed in

Table 5.3 Radiance correction for the two filters, FW#7 and FW#8, obtained from black body measurements. The correction values (rc-FW#7, rc-FW#8) are filter-wise radiance correction for the illuminated area in the field of view.

IA [%]	IA [px]	ε[-]	T [°C]	rc-FW#7	rc-FW#8
4	12679	0.993	492.0	1.151	1.144
10	34419	0.910	500.6	1.061	1.055
38	125195	0.986	489.1	1.003	1.000
58	190468	0.988	492.3	1.003	1.002

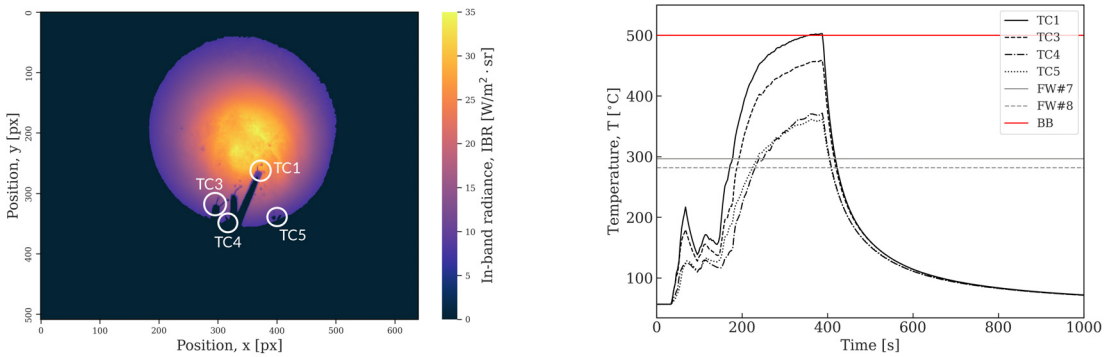

(a) (b)

Figure 5.8 IR image of the backside of the steel plate, heated with a gas torch from the opposite site, with spot-welded thermocouples and their ceramic tubes partly visible. (b) Thermocouple temperature curves during a test, reaching approximately 500 °C in the centre. TC4 and TC5 are located at the same radial distance (30 mm) from the centre. The thermocouple accuracy is ±0.75 % in this range and does not exceed ±3 °C. The lower threshold temperatures for FW#7 and FW#8 are indicated with horizontal lines.

Tab. 5.4 in the 'SOC100-HDR' column.

As a general trend for two composite materials, the emissivity is lower when CF is used as reinforcement compared to GF, and spatial variations are small ($\Delta\varepsilon$ = 0.02). The average emissivity was 0.9 for GF-Ph samples, while it was 0.86 for CF-Ph samples. The effective emissivity of pristine CF samples has been measured as 0.88. Total emissivity of pristine GFRP is typically indicated between 0.9 and 0.95 in the literature [195, 196]. As the resin burns the main contribution to the total sample emissivity shifts from the virgin matrix to the thermally degrading matrix and finally to the reinforcement fabric itself. For silica glass, emissivity values at room temperature are reported as 0.9-0.95 and for (graphitized) carbon 0.77-0.8 [197]. Sample GF-Ph4 was essentially bare fabric following fire exposure and thus the value obtained of ε=0.91 is coherent with the literature data.

For the large SAE 304 steel plate sample, the flame was impinging on the centre, approximately

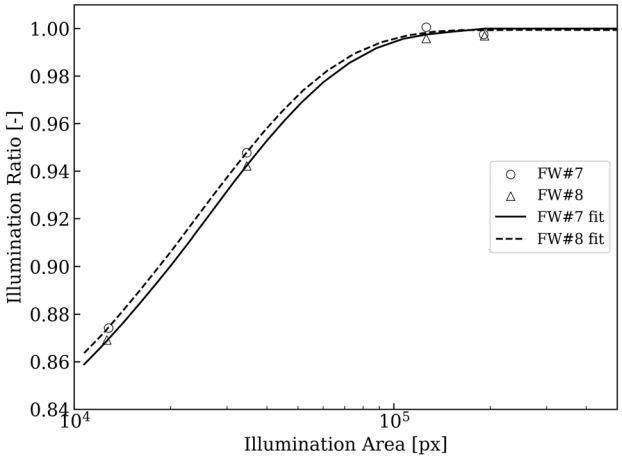

Figure 5.9 Radiance correction based on the contributing pixels with respect to a fully illuminated sensor array.

where SS-3 is located. As Fig. 5.10 shows, the thermal treatment of the steel resulted in an oxidation of the surface, which also increased its roughness. Away from direct flame impingement, the oxide layers create distinct "annealing colors" that give an estimate of the maximum temperature occurring in the zone. For instance, the golden yellow that transitions into purple as seen on sample SS-1 is representative for a temperature from 350 °C to 450 °C for this alloy. The total emissivity measured for SS-3 ($\varepsilon = 0.65$) is in excellent agreement with values reported for comparable stainless-steel samples oxidized for 5 min at 800 °C [198]. The samples SS-1 and SS-3 are out of the FOV of the IR camera and cannot be compared against results from the TES algorithm. Based on literature data [199,200] the golden yellow oxide layer is estimated to be less than 500 nm and the blue oxide layer to be approximately 200 nm thick. Roebuck et al. [201] have presented a study that shows that thin oxide layers like these can impose large temperature errors when using 1C pyrometry. The effect of the oxide layer thickness on the emissivity of steel, in particular for shorter wavelengths, has been previously reported to result in values coherent with our observations by Jo et al. [189].

5.5.3 Verification of gray body hypothesis

The HDR results presented in Sec. 5.5.2 and in Tab. 5.4 give the effective emissivites of the samples, that is the integrated value over the entire spectral range. However, emissivities often show a spectral dependency, as shown in Fig. 5.11a for three different samples. The thermally degraded GF-Ph3 sample showed a pronounced decrease of emissivity at wavelengths shorter than 2.5 µm. The emissivity of the CF-Ph3 and steel SS-3 samples remained relatively constant over the spectral range used in the HDR measurements. Two important assumptions of our radiation model are that

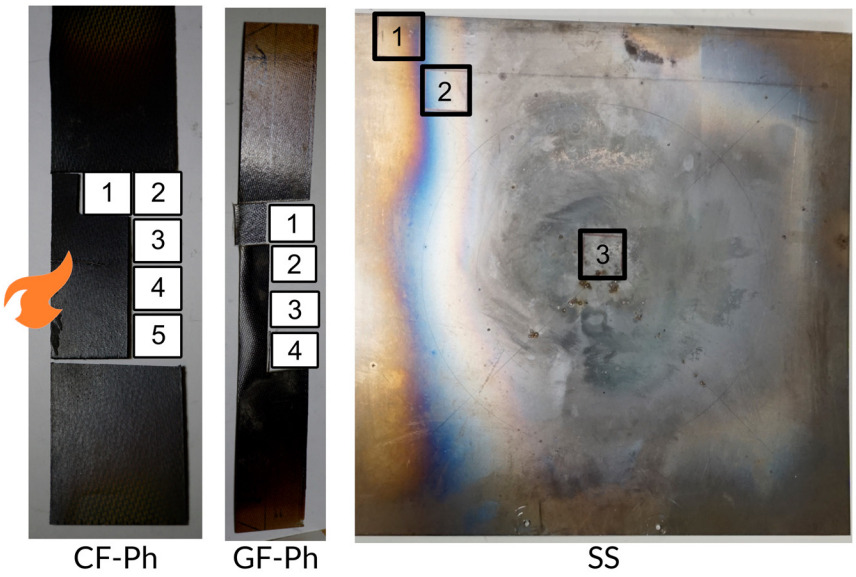

Figure 5.10 Samples used for post-fire emissivity measurements. The flame impingement was centred at the vertically oriented samples in-between position two and three for the GF-Ph and in-between position three and four for the CF-Ph sample. 25.4 mm × 25.4 mm squares have been cut from the samples for emissivity measurements.

Kirchhoff's law can be applied (cf. Tab. 5.2) and that the sample emissivity is constant within the spectral band of the filters. The HDR measurements were used to test this last hypothesis and the hemispherical emissivity data shown in Fig. 5.11b is linearly fitted. Although the slope is different from unity for all materials, the emissivity varies not more than 0.14 % for all samples over the spectral bands of filter FW#7 and FW#8. It is thus reasonable to assume constant values within each filter band. Nevertheless, the emissivity may vary from one filter to another by a conservative estimate of 1 % at 0.8 nominal emissivity. The resulting error for a given filter contributes with 8.1 °C to the overall error budget.

5.5.4 In-situ emissivity measurements

Comparison between the emissivity mapping obtained from the TES algorithm and the HDR measurements was carried out by computing the average over the pixel-area within the FOV that corresponds to the sample cutouts in Fig. 5.10. Two important points must be highlighted for the subsequent discussion. First, the HDR measurements were performed at room temperature following fire exposure. Second, the minimum radiance level necessary to overcome the noise level for the filters used require a minimum sample temperature of approximately 300 °C. In addition to this temperature difference, the sample also continues to degrade during cool down and thus

Table 5.4 Comparison of surface spectral emissivity measurements averaged over a square cutout of 25.4 mm length after fire testing by hemispherical directional reflectometry (HDR) and 2C pyrometry. The sample numbering refers to Fig. 5.10 and indicates the spatial location.

Category	Sample	Measured spectral emissivity, ε[-]				
		SOC100-HDR		IR camera		Difference
		Mean	SD	Mean	SD	$\Delta\varepsilon$
Carbon-fibre phenolic	CF-Ph1	0.88	0.02	0.65	0.04	0.23
	CF-Ph2	0.86	0.02	0.70	0.04	0.15
	CF-Ph3	0.86	0.02	0.65	0.04	0.21
	CF-Ph4	0.86	0.02	0.70	0.04	0.16
	CF-Ph5	0.86	0.02	0.76	0.04	0.11
	mean	0.86	-	0.69	-	0.17
Glass-fibre phenolic	GF-Ph1	0.90	0.01	0.67	0.03	0.23
	GF-Ph2	0.88	0.01	0.71	0.03	0.17
	GF-Ph3	0.89	0.01	0.63	0.03	0.26
	GF-Ph4	0.91	0.01	0.72	0.03	0.19
	mean	0.90	-	0.68	-	0.22
Stainless steel	SS-1	0.07	0.25	-	-	-
	SS-2	0.11	0.25	-	-	-
	SS-3	0.64	0.27	0.66	-	0.02

the sample state as seen by the HDR can differ from the end of the sequence acquired by MS-IR camera. To minimize this discrepancy, only the last 50 frames of the IR acquisition were used to calculate emissivity and temperature maps of the sample subregions. The results from this analysis are summarized in Tab. 5.4. Representative emissivity and temperature maps for the CF-Ph sample at approximately 380 °C are shown in Fig. 5.12, together with the subregions that correspond to sample CF-Ph3.

It is apparent from Tab. 5.4 that the in-situ emissivities obtained with the TES algorithm are significantly lower for the composite samples than the ones analysed post-fire. This is caused by the complex temperature dependency of the emissivity. The values we report are consistent with a similar CFRP sample subjected to the same burner and conditions, where TES analysis yielded comparable values in the range of 0.5-0.7 [202]. Although Fig. 5.12 illustrates that the thermal degradation of composite materials can display large spatial variations, an averaged emissivity value is still meaningful if the ROI is chosen accordingly.

Jones et al. [192] proposed a model for the temperature dependence of glass-fibre composites emissivity. Using their model and accounting for the temperature difference ($\Delta T \approx 420\,°C$) between

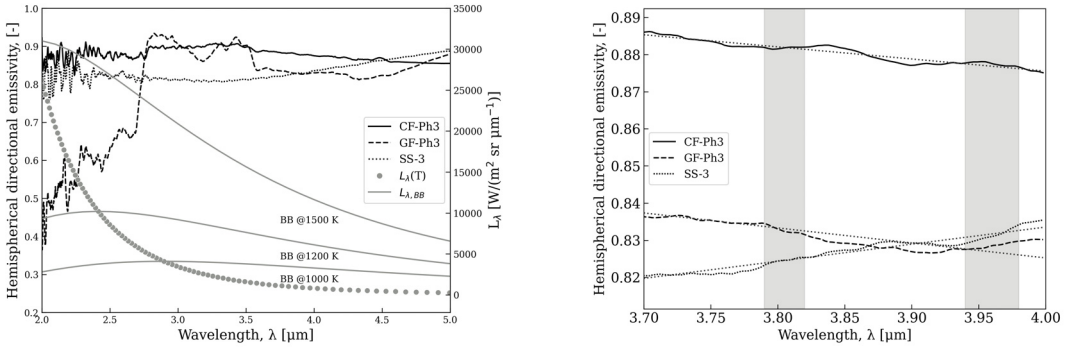

(a) (b)

Figure 5.11 (a) Hemispherical directional emissivity of a carbon-fiber phenolic (CF-Ph), glass-fiber phenolic (GF-Ph) and stainless-steel (SS) sample degraded under a kerosene flame of 116 kW/m^2. The radiance of a black-body at different temperatures is overlaid. (b) Emissivity in the spectral region of the filters used for 2C pyrometry, shown as gray bars.

HDR and TES measurements, the coefficients identified from GF-Ph data corresponds well to the coefficients typical for glasses. It is to be expected as resin depletion at the end of the test results in the exposed surface being mostly reinforcement fibres. Furthermore, the decrease in emissivity from approximately 0.9 at room temperature (HDR at 20 °C) to 0.65 at 440 °C (TES with ΔT = 420 °C) is also consistent with the high temperature emissivity measurements of quartz glass at similar temperatures reported in the literature [203, 204].

For the stainless-steel sample, the emissivity obtained for SS-3 through TES calculations from IR data is in excellent agreement with the HDR measurements. Once the oxide layer has reached substantial thickness (>10 µm), temperature and emissivity variations over successive 50 frames interval can be neglected. Moreover, the oxide layer reduces reflective contributions which contributes to reduce the overall error.

The results from this analysis suggest that total emissivity can indeed be regarded as independent from wavelength within the spectral range of the filters. Moreover, it can be justified to use averaged emissivity values for subregions that are homogeneously burnt. A global constant emissivity value measured at room temperature is not representative for high-temperature tests for composite samples not even for ones that are significantly degraded and whose emissivity is mainly determined by their fibre reinforcement. Although the emissivity from steel samples has a less pronounced temperature dependence, it is important to notice that the surface oxidation progresses rapidly under flame exposure resulting in drastically changed emissivity and making it extremely challenging to measure surface temperatures during heat-up with conventional IR thermography.

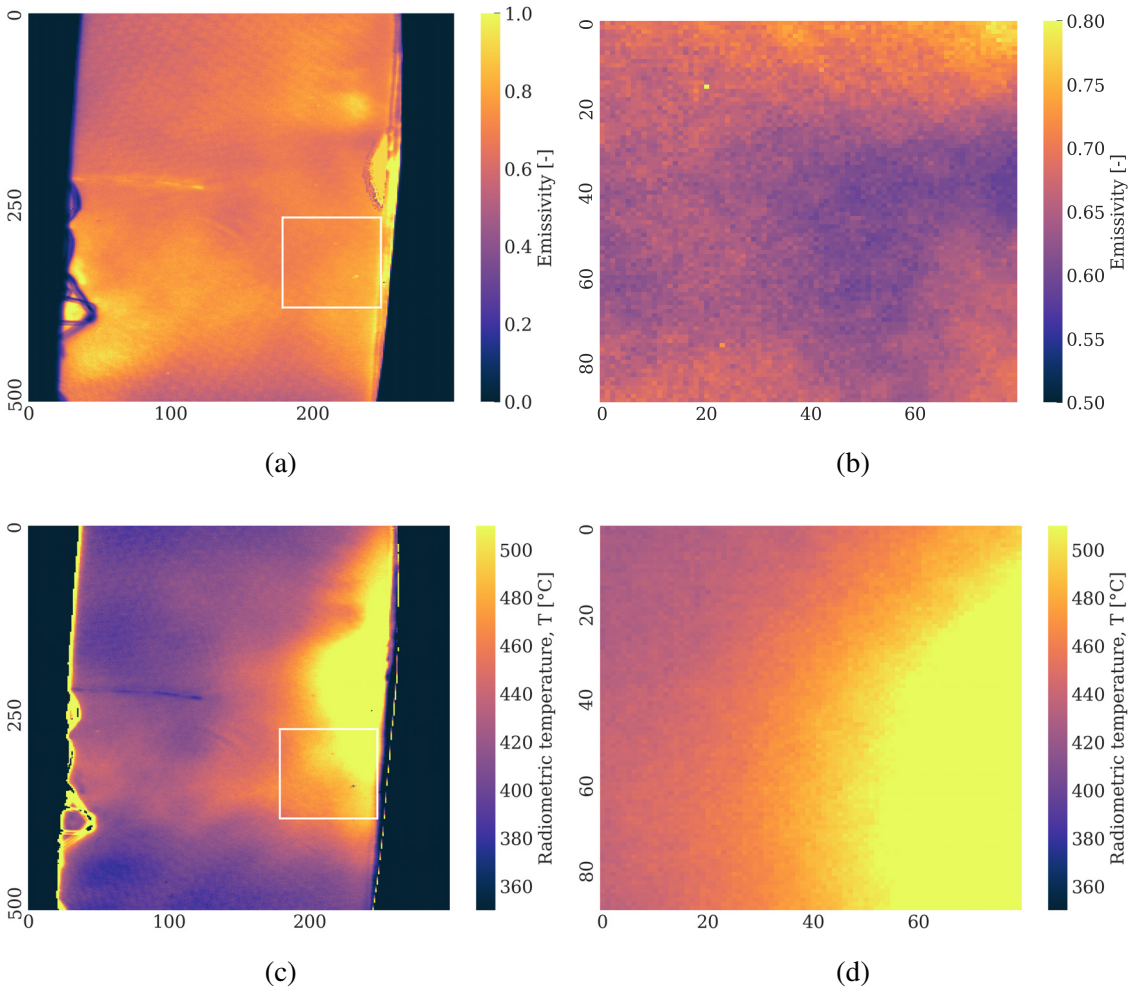

Figure 5.12 Emissivity and temperature mapping of a CF-epoxy sample exposed to a flame. The images on the right are the subregions indicated by the white rectangle. The subregions are used to calculate average value. The colorbar range for the emissivity subrange has been modified to better illustrate spatial variations.

5.5.5 In-situ temperature measurements

To test the radiometric accuracy of the TES algorithm, the temperature was simultaneously acquired at the back of a CF epoxy sample using a thermocouple probe and the IR camera. The acquisition frame rate was set to 20 Hz as temperature changes were not expected to be fast, based on previous TC measurements on similar samples. Fig. 5.13 shows an example of an infrared image of the sample back face during cool-down, with the integrated thermocouple clearly visible. During post-processing, an area of 20 px × 20 px at the location of the thermocouple probe is used to obtain average signals for the filters (Fig. 5.13). The raw signals (Fig. 5.13b) from FW#7 and FW#8 are smoothed using a moving average and then used to form the signal ratio. In a final step the temperature and emissivity of the sample in the vicinity of the thermocouple is calculated from the IBR ratio. The final IR temperature signal was further smoothed with a Savitzky-Golay filter with a window size of 69 successive frames.

Fig. 5.14a shows the temperature curves obtained through the TES alogorithm compared against the TC measurements. The acquisition with the IR camera was triggered slightly delayed so that the first data points start when the back face temperature has already risen above 400 °C. The curve obtained with the 2C technique implementing the necessary corrections is in excellent agreement with the thermocouple data. The results are compared against an implementation of conventional 1C pyrometry data, using only a neutral density filter (FW#2) or a single channel (FW#7), relying on the emissivity of pristine CF epoxy samples (ε=0.88). This data illustrates that assuming a constant emissivity value for composite samples, often taken from post-fire measurements, might result in high errors in temperature readings, as variation exceeding 10 % are easily observed during the test, especially when doing single-color pyrometry.

With the temperature available, the emissivity evolution was calculated and is shown in Fig. 5.14b for approximately the last five minutes of a fire exposure test. The emissivity range obtained for the CF-epoxy samples averaged over different subregions through the TES algorithm is red shaded. The gray shaded area represents literature data for the emissivity of CF-epoxy samples exposed from 30 s to 100 s to a radiant heat flux of 65 kW m^{-2}, with the dashed black line indicating an emissivity value often used for 1C pyrometry measurements in similar fire exposure tests [100, 118].

5.5.6 Error budget

Tab. 5.5 lists the individual contributions to the overall error budget, along with typical values. The temporal noise is the uncertainty of measurement associated to a single temperature reading and thus a single pixel. The radiance ratio suffers from the temporal noise in each of the two filter channels. The typical FW#7 camera noise for an apparent temperature of 500 °C is 30 mW/(m^2 sr)

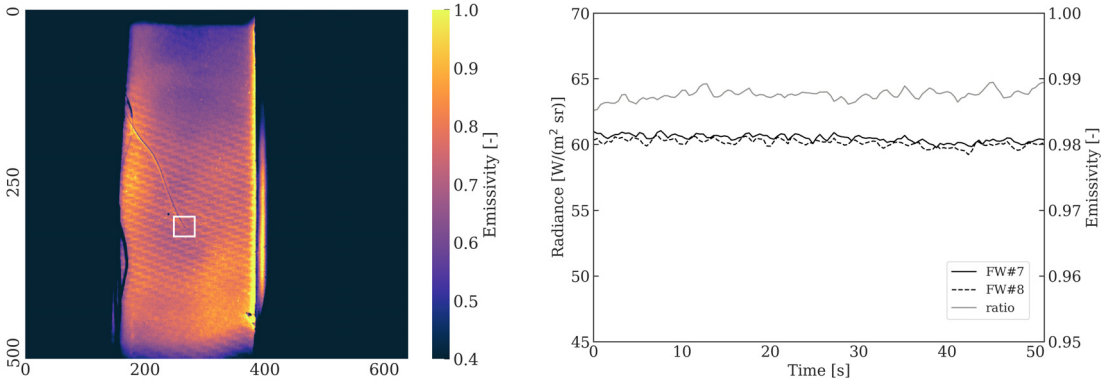

(a) (b)

Figure 5.13 (a) IR image of the sample backside, with the attached thermocouple wire clearly visible. A measurement area of 20 px × 20 px has been placed around the thermocouple junction (white rectangle). (b) Raw radiance signal from the two filter used to calculate the IBR-ratio.

for a radiance of approximately 43.5 W/(m^2 sr). This figure of performance is similar with the second filter. The resulting standard deviation on the radiance ratio is then 0.00094, translating to an error of 3.8 °C for a scene of approximately 500 °C. This pixel-wise performance figure can be improved with either temporal or spatial averaging. The temporal noise measurement for high temperature targets can be for instance performed with a high temperature black-body in front of the camera, but is difficult due to thermal turbulence. Therefore, the temporal noise is simulated and scaled to the filter response to provide the noise equivalent differential IBR.

If the image superposition is not perfect between the two frames used for the 2C pyrometry method, a parallax error is associated with a band ratio difference, leading to inaccurate temperature-emissivity retrievals. The camera enables a position correction for each spectral band in both axes, but results on the sample backside did not require its implementation for our tests. Since the spatial resolution is about 0.6 mm per pixel, the region of interest is chosen wide enough to spatially average the signal. This allows for an improved signal to noise ratio for the macro-pixel. The error caused by the difference in spatial features from one filter to the other is evaluated to be lower than 0.01 W/(m^2 sr).

Radiometric accuracy is verified against a calibrated black-body for each spectral band. The camera absolute accuracy is found to be in the order of ±0.2 % for a black-body set at 500 °C, that translates into an error contribution of 5.5 °C for the retrieved temperature.

As outlined in Sec. 5.5.1, the filter-wise radiometric correction requires an estimation of the number of pixels in the illumination area. The uncertainty of providing the accurate illumination area leads to a maximum error of 0.7 % in the illumination ratio for each spectral band. The resulting error is again 6.4 °C for a scene at 500 °C.

The assumption that the emissivity remains constant within the filter spectral range for both filters contributes to the error budget. For a maximum error of 1 % in the emissivity difference between the two filter bands, the resulting error is 8.1 °C.

For the measurements considered here where both the sample temperature and emissivity change with time, the choice of the acquisition frequency can be an important source of error. Ideally, the frame rate must ideally be selected such that the overall uncertainty of the measurement is on the same order of magnitude as the temporal noise. The temperature increase remained below 0.224 °C/s at a sample temperature of approximately 500 °C. Acquiring the signal at a frequency of 0.8 Hz allowed to keep the maximum error below 0.28 °C. The corresponding error contribution is 7 °C. However, if the temperature increase is instead 2.24 °C/s, the associated error is ten times higher. This specific behavior underlines why great care must be applied to select a frame rate sufficiently high to limit frame rate related errors as they can rapidly overwhelm other sources of uncertainty.

Table 5.5 Example of a typical error budget for a measured sample temperature of (500 ± 28) °C. The reported expanded uncertainty U of measurement is stated as the standard uncertainty u of measurement multiplied by the coverage factor k = 2, which for a normal distribution corresponds to a coverage probability of approximately 95 %.

	Quantity		Maximum error	
Source	Description	Estimate	u [a.u.]	u [°C]
Pixel-wise	Temporal noise	0 mW/(m^{2}sr)	30 mW/(m^{2}sr)	3.8
	Parallax error	<60 mW/(m^{2}sr)	10 mW/(m^{2}sr)	0.9
Filter-wise	Camera accuracy	<0.20 %	10.00 %	5.5
	Geometric correction	<0.70 %	0.12 %	6.4
	Emissivity assumption	<1.25 %	0.21 %	8.1
	Frame rate limitations	<0.224 °C/s	0.224 °C/s	7.0
			total	14.2
			expanded uncertainty U	28.4

5.6 Conclusion

Infrared thermography is a powerful tool for in-situ observation of the temperature evolution of fast degrading materials, such as polymer-matrix composite samples exposed to a flame. However, conventional IR thermography requires the prior knowledge of the sample emissivity. As burning composites degrade rapidly and the metallic samples carry over large contributions from the surroundings, the proper characterization of the source emissivity becomes virtually impossible.

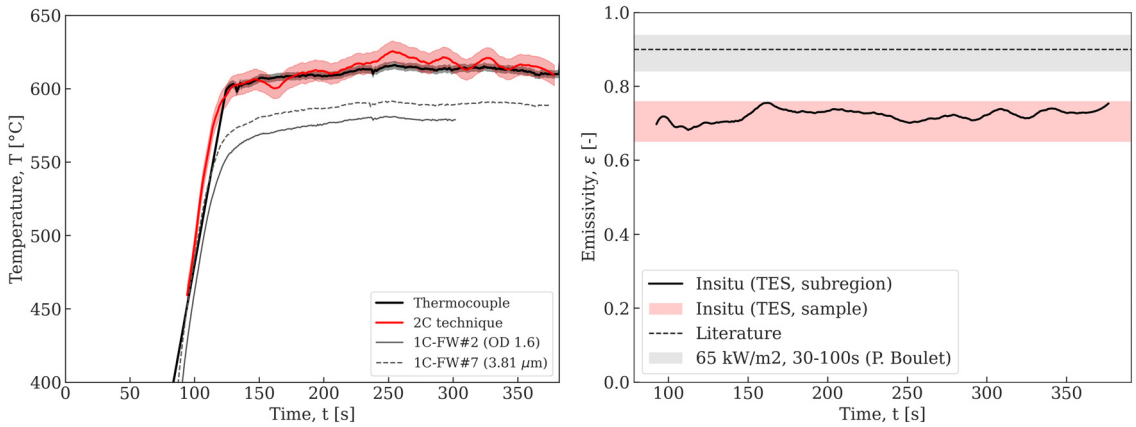

(a) (b)

Figure 5.14 (a) Thermocouple signal compared against the temperature signal retrieved using the 2C technique from a 20 Hz frame rate acquisition as well as 1C thermography calculations. (b) Emissivity evolution on the backface of CF composite sample exposed to a flame measured through 2C pyrometry. The gray area corresponds to the emissivity measured for different zones on a similar sample subjected to comparable test conditions from literature [172].

Two-color pyrometry is a technique that can overcome this problem, but although it becomes popular in the fire testing community its common error sources are often unappreciated. In this work, the temperature and emissivity evolution on the back face of samples subjected to a flame were studied using a multispectral IR camera equipped with a fast-rotating filter wheel.

We present a detailed radiometric model to account for the contributing factors of the overall radiance signal originating from the sample itself, the background and the atmosphere. The background contribution is particularly significant below 300 °C but can be neglected in our case as the optical band-pass filter selected does not detect below this temperature. A thorough sensitivity analysis demonstrated that two basic assumptions must hold true between two subsequent acquisition frames: first, the material under thermal degradation must behave as a gray-body and second, the transmission of the selected optical filters must not depend on the emissivity of the object within their respective spectral band.

We implement a multi-step image analysis process, associated experiments to obtain necessary material properties. In a first step, a geometric correction helps to adapt the camera calibration to the actual illuminated area and thus to take into account only the pixels that contribute to the overall radiance signal. Without such a correction, the target temperature was underestimated by 10 °C and yielded unphysical emissivity values above one. In a second step, we subjected carbon-fibre and glass-fibre composites as well as stainless steel plates to a calibrated kerosene flame. The emissivity of the burnt samples at different position was also measured using hemispherical directional

reflectometer. It could be shown that these composite materials exhibit the same selective transmitters tendency as other polymer and that their emissivity decreases as a function of temperature, relative to measurements conducted at room temperature. For the steel sample tested, the thickness of the oxidation layer is important and the spatial variation of emissivity ranged from 0.07 to 0.64 for heavily oxidized steel plates .

The emissivity results obtained using the 2C technique and the proposed corrections are in excellent agreement with literature data measurements obtained from embedded thermocouples. The experimental methods, hardware selection and image post-processing including necessary corrections presented here allows the measurement of the back face temperature of composite materials exposed to a flame within an uncertainty below 30 °C at a temperature of 500 °C.

Declaration of competing interest

The authors declare no potential conflicts of interest with respect to the research, authorship, and/or publication of the this article.

Funding

The authors want to acknowledge the financial support from the Natural Sciences and Engineering Research Council of Canada (NSERC/CRSNG) grant no. CRDPJ 478687-15, and the partners from CRIAQ ENV-708 project.

Acknowledgements

The authors wish to thank Jean-Philippe Gagnon for his expertise and valuable support during the initial experimental campaign.

CRediT authorship contribution statement

Tanja Pelzmann: Conceptualization, Data Curation, Formal analysis, Investigation, Methodology, Software, Writing - Original Draft, Writing - Review & Editing. **Fabien Dupont:** Data Curation, Formal analysis, Methodology, Software, Validation, Writing - Original Draft, Writing - Review & Editing. **Benjamin Sauté:** Validation, Writing - Review & Editing. **Étienne Robert:** Funding acquisition, Supervision, Writing - Review & Editing.

CHAPTER 6 ARTICLE 3 EFFECT OF FLAME CHEMISTRY ON THE THERMAL DEGRADATION OF CARBON FIBRE EPOXY COMPOSITES

Tanja Pelzmann[a], Pablo Chávez-Gómez[a], Louis Laberge Lebel[a], Martin Lévesque[a], Étienne Robert[a]

[a]Polytechnique Montréal, 2500 Chem. de Polytechnique, Montréal (QC), H3T 1J4, Canada

This article was submitted to the *Fire Safety Journal* (April 26th, 2022).

Abstract

Modern commercial and military aircraft are for the most part made of high-performance composites due to their high strength paired with low weight and high stiffness. These materials are also required to be fire-resistant for safety-critical applications, with component certification relying on costly tests that expose specimens to standardized kerosene flames. Gas-fueled and small-scale highly instrumented test rigs are useful to provide insight on the degradation and failure mechanisms, but the calibration procedures prescribed by certification standards can yield differences in the oxidative potential of the flame atmosphere. The present study investigates how the flame chemistry and thus the composition of the reactive flow influences the thermal degradation of a carbon-fibre epoxy composite material. Three types of flames, all with the same nominal heat flux density and temperature, are used in a bench-scale instrumented rig operated with composite coupons. The effect of two different propane flames is compared against a kerosene flame, providing backside temperature data acquired with thermocouples and infrared imaging, mass loss over time and residual mechanical strength. The microstructural analysis of burnt specimens and oxidized fibres is also presented. Experimental results clearly show that the nature of the flame cannot be neglected, while demonstrating that a gas flame can be modified to induce thermal degradation behaviour very similar to a kerosene flame. The influence of parameters such as the reactants flow rate, the flame equivalence ratio and the oxidizer concentration in the flame exhaust should be acknowledged when performing fire tests at any scale, when the aim is to mimic the aerospace fire hazards considered for certification testing.

Keywords: Aircraft composites; Fire resistance; Kerosene flame; Propane flame; Small-scale testing; Thermal degradation

Highlights

- Composite specimens are subjected to kerosene and gas flames, with the residual mechanical properties measured
- Heat flux density and flame temperature measured at the stagnation point are not sufficient to characterize a fire hazard
- The nature of the flame directly affects the thermal degradation of composite materials
- Dilution with carbon dioxide provides a way to control the aggressiveness of gaseous flames towards fibre oxidation

6.1 Introduction

Economic and environmental pressure on the transportation sector motivates a sustained effort to reduce energy consumption and enhance the power-to-weight ratio. The combination of carbon fibres (CF) and thermosetting epoxy resins has now attained widespread use in aerospace applications [205]. For example, more than 50 % of the structural weight of modern aircraft such as the Boeing 787 [206] or the Airbus 350 [207] is made of CF reinforced composites. As the application domain of Polymer-Matrix Composites (PMCs) is extending, they are now considered for demanding operating conditions and elevated temperatures such as firewalls. By maintaining their structural integrity for a prescribed time, firewalls are meant to protect the aircraft structure and ensure the continuous operation of critical components following an in-service or post-impact fire event. Response to fire is evaluated in certification tests such as those described in AC 20-135, issued by the US Federal Aviation Administration (FAA) [37], with the test equipment detailed in the FAA Powerplant Engineering Report No. 3A [46]. The international ISO 2685:1998(E) standard [9] refers to both of these documents, with test conditions largely considered equivalent.

The general approach of the certification agencies has been to develop lab-scale tests with easily observable acceptance criteria, whose results can be correlated to large-scale tests where full components are burnt [7]. For aircraft firewalls, vertically mounted specimen panels larger than $305\,\mathrm{mm}^2 \times 305\,\mathrm{mm}^2$ are exposed to a calibrated flame for between five and fifteen minutes. The "standard" flame has a heat flux density of $(116 \pm 10)\,\mathrm{kW/m^2}$ and an average flame temperature of $(1100 \pm 80)\,°\mathrm{C}$. Still, even these lab-scale tests are at best intermediate-scale and remain costly as only a limited number of test facilities perform them. Moreover, they only provide a pass/fail verdict that is not conducive to product development [208], modelling [209] or quick screening of promising material systems [145].

Small-scale bench tests at the coupon level can be very useful to understand the thermal degradation mechanisms occurring as PMCs are exposed to flames representative of aerospace fire hazards. Gas torches are extensively used for this purpose, as they are much simpler to implement, when compared to kerosene burners. Bartlett [210] proposed an oxygen acetylene heating tip for certification-like testing on aluminum and composite panels. Kim [211] later used a propane gas torch combined with external mechanical loads for fatigue testing of silicon carbide fibre-reinforced silicon carbide matrix composites. Akshatha [212], among others, used a Bunsen-type burner for an experimental study on protective solutions for firewalls. Gibson [81,213] first used the propane torch model also used in this study to evaluate composites under fire. This equipment selection inspired other similar fire test rigs targeting composite testing, such as the work of Tranchard [214]. Hörold [22] used the same equipment to support numerical modelling and more recently Tabaka [102] addressed response to fire under compressive loads. It is interesting to note that the SAE AS401B gas burner, proposed by ISO 2685 [9], features a premixed flame supplied by a nozzle grid. The common small propane torches, when operated with a pure fuel stream, fail to recreate the flame momentum and fluid dynamics of this large-scale gas burner.

For FAA regulations however, propane gas burner and oxy-acetylene torches previously allowed for certification testing are now banned [37]. This strict requirement for liquid-fuelled flames acknowledges that gas burners fail to produce a representative fire hazard and limits the value of work done at the coupon level using simple gas flames. Soot formation, turbulent mixing and the composition of the flame atmosphere are all known to play a role in the aggressiveness of the flame attack, in particular for polymer degradation [101,215–218].

The few bench-scale test rigs involving an oil-fuelled burner presented in the literature to evaluate the response to fire of PMCs rely on commercial oil burners, such as that used by Sanchez et al. [128] to study surface temperatures via infrared thermography. Schuhler et al. [118] also opted for a domestic oil burner that was modified with an extension tube to direct a hot jet of combustion products towards the specimen. In the absence of an established consensus on burner hardware, fuels, and operating conditions for small-scale testing, assessing calibration equivalency remains difficult. Consequently, different research groups do certification-like tests at different scales under nominally identical heat flux and temperature, but with different flame chemistry and dynamics in the reactive flow. Both factors, however, are important and directly affect the degradation behaviour by promoting oxidation [219] or varying the heat transfer pattern.

In this work, we use a small-scale kerosene burner developed in-house [119] and designed to reproduce the characteristics of the sonic oil burner developed as part of FAA's NextGen program [142, 158], as well as a commercially available propane torch extensively used in the fire research community. The latter is operated with pure propane or a diluted propane mixture. The two gas

flames and the kerosene flame with nominally the same heat flux and temperature allow the investigation of the fire response of carbon fibre (CF) epoxy specimens as a function of flame chemistry.

We measure the residual mechanical properties following fire exposure for different periods of time as well as the specimen backside temperature and mass loss over time for all three flame types. The post-fire microstructure and the degree of fibre oxidation in the specimens are compared using optical microscopy and scanning electron microscopy (SEM). The novelty of this study lies in the investigation of the interplay of material degradation, flame chemistry and burner parameters in small-scale tests. The impact of the flame nature on the residual strength and thermal degradation of CF epoxy composites is discussed and shown to be an important parameter in small-scale fire tests and the interpretation of their results.

6.2 Materials and methods

6.2.1 Specimens

Specimen strips measuring 25.4 mm × 305 mm and approximately (1.65 ± 0.02) mm in thickness were cut from aerospace-grade NCAMP [150] carbon-fibre epoxy panels (MTM45-1, Solvay). The material system is an Out-of-Autoclave (OOA) toughened epoxy with 36 % resin content and standard-modulus carbon fibre reinforcement (HTS40 E13) with a 3K plain weave. The panel lay-up is a quasi-isotropic, balanced and symmetric 8-ply laminate ($[0°, +45°, 0°, -45°]_S$) and was prepared according to the manufacturer's recommended cure and post-cure cycles. This material is representative of composites considered for firewalls applications outside the fuselage, with or without parasitic fireproofing treatment, [147] and comparable to the configurations used in similar work [118, 128, 214]. 76 coupons were cut by waterjet to minimize edge damage, with an average mass of 18.55 g each. Thermogravimetric analysis (TGA) of this material at different heating rates, in oxidative (air) or inert (nitrogen) environment, is available in our previous work [147]. Thermal and chemical properties obtained from differential scanning calorimetry (DSC) and Xenon flash thermal constant analyzer (XFA) are also presented by Langot et al. [220].

6.2.2 Small-scale test rig and burners

A schematic representation of the experimental facility is shown in Fig. 6.1, viewed from the top, with a vertically mounted specimens exposed to the pilot flame, reproducing the conditions of large-scale fire tests, nominally a heat flux of (116 ± 10) kW/m^2 and a temperature of (1100 ± 80) °C. The rig is integrated in a test chamber of approximately 1 m^3 in volume with a constant ventilation of 13.6 m^3/min, sufficient to prevent smoke accumulation but without inducing perturbation on the pilot flame interaction with the specimen. The chamber allows the monitoring of ambient

conditions and provides optical access from four sides through large acrylic windows. For the tests discussed in this work, the specimens were clamped on top and bottom. This limits specimen delamination and improves the accuracy of the back face temperature measurements during the fire tests. Additionally, the specimens were shielded from both sides with low density ceramic fibre boards (CeraMaterials), protecting the edges from the impinging flame. A camera on the backside (GoPro Hero 5) allows the observation of backside ignition, if any.

An overview of the three flame configurations used in this work is provided in Tab. 6.1, compared to burner parameters prescribed by the certification standards and those used by a selection of other research groups. Unfortunately, the fuel and oxidizer flow rates are often not disclosed in the literature, which makes it difficult to recreate operating conditions yielding the same flame chemistry. For the work presented here, the gaseous pilot flame is generated using a propane torch (Bullfinch BF1270), modified in a similar way as in the work of Tranchard et al. [214] by the addition of a copper cooling coil connected to an open bath circulator (Julabo EH-5). The water supplied to the coil is maintained at (21.0 ± 0.1) °C to prevent the metal torch from preheating the reactant mixture and hence increasing the flame temperature as the test progresses. Using a cooling temperature below 19 °C results in water condensation inside the cone and promotes corrosion. The fuel flow (propane, consumer-grade (HDP5) C_3H_8, Parkland Fuel Corporation) is supplied through a mass flow controller (HFC202, Teledyne Hastings), with the option of mixing in a controlled amount of inert dilution gas (CO_2, 99.99 % purity, Air Liquide Canada). Although carbon dioxide does not react in the flame, its presence can contribute to the oxidation of carbon fibres [219], thus providing a mean to control the aggressiveness of gaseous flames independently of flame temperature and heat flux.

Two operating conditions are used for the gas burner in the results presented here. In the first (Prop100), propane is supplied pure at a constant flow rate of 7 slpm. The oxidizer is ambient air that is drawn in by the expanding fuel stream through an opening located immediately downstream of the nozzle. Due to the torch design, the oxidizer flow rate cannot be controlled or quantified. The flame can be described as turbulent, partially premixed and approximately stoichiometric, from its largely blue colour. In the second configuration (Prop90), the propane is diluted with 10 % CO_2 (by volume). The resulting flame (Prop90), is slightly leaner, cooler and shorter compared to the first configuration. To compensate and achieve the same temperature and heat flux at the specimen location, the fuel mixture flow rate is increased to 9 slpm. The standoff distance between specimen and burner is also adjusted between these two flame configurations. For the Prop100 configuration, the standoff distance is 75 mm while for Prop90 it is 185 mm, in both cases resulting in the exposure of the specimens to the nominal conditions prescribed in the certification standards. Photos of the flames together with the respective burner parameters are presented in Fig. 6.2.

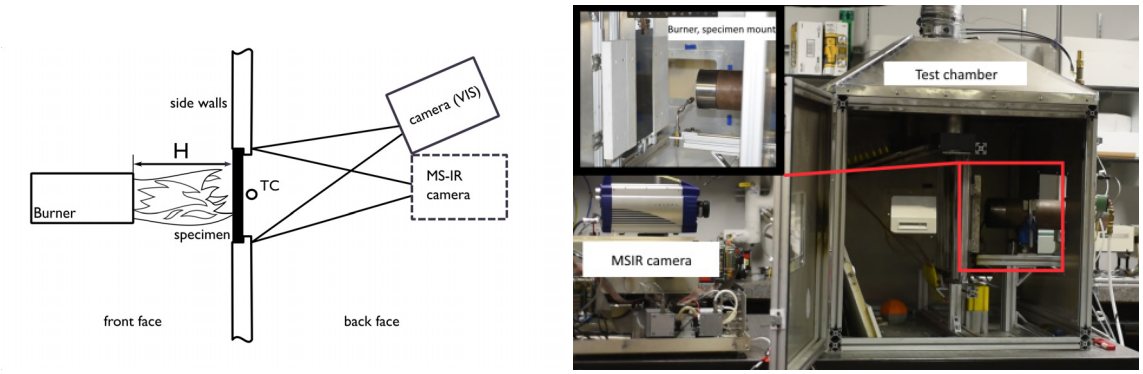

(a) (b)

Figure 6.1 (a) Schematic representation of the experimental setup. The burners used can be either a small-scale kerosene burner or a propane torch. (b) Photo of the test setup with a close-up of the specimen mount. The optical camera is behind the IR camera.

A small-scale kerosene burner (miniK) has been developed to reproduce the conditions of the ISO 2685 standard using liquid fuels for bench-top experiments at the coupon level. It features a swirl-stabilized flame, as described in detail by Béland [146]. For the work presented here, a swirler with 15 blades oriented at 25° is used, resulting in stable flames with a thermal power ranging from 8 kW to 30 kW. Several parameters affect the flame produced by this burner, with a careful selection of the fuel atomization nozzle being essential to achieve stable combustion for the low-power conditions required here. Indeed, most nozzles rated below 20 l/min are pressure-driven and operating a nozzle below its nominal rating directly affects the flow pattern, droplet size and consequently the flame shape and stability [222]. To ensure efficient combustion, a return-flow (bypass) nozzle (Delavan 33769-2) is implemented to ensure the required pressure for proper fuel atomization even at very low flow rates. Another key aspect to maintain a reproducible and well-controlled flame chemistry is the oxidizer used. The oxidizer intake of the miniK is supplied through a flow controller (Omega, FMA5444) and uses dehumidified air at constant pressure and temperature. Large-scale oil burner used for certification, such as The NextGen burner developed by the FAA, are much more powerful with a typical thermal heat release rate of approximately 80 kW. The required conditions in terms of heat flux and temperature have been shown to be achievable in both lean and rich conditions [142], although the exact flame chemistry is seldom available in the literature. In lean flames, the residual oxygen content in the exhaust gases can increase the reactivity of PMCs and promote their degradation. To avoid this effect from perturbing our investigation, all three flames considered here have nominally the same heat flux density at the stagnation point, flame temperature and equivalence ratio. The differences between flames is therefore limited to *Re*, shape, and the nature of the fuel used.

Table 6.1 Flame configurations used in this study and compared to selected literature. Φ denotes the equivalence ratio and H the standoff distance between burner exit plane and specimen surface. All flames aim to reproduce the conditions prescribed in ISO 2685 (heat flux of 116 kW/m^2 and temperature of 1100 °C).

Fuel	Oxidizer	Φ	H [mm]	Model	Reference
C3H8, 7 slpm	air, -	1	75	Bullfinch 1270	This work (Prop100), [100, 221]
C3H8, 10% CO2, 9 slpm	air, -	<1	185	Bullfinch 1270	This work (Prop90)
C3H8,-	air	1	275		[102]
C3H8, -	air,-	-	340	Bullfinch 1270	[21]
C3H8, -	air, -	-	75	SAE AS401B	ISO2685 [9]
Jet-A, 0.45 g/s	air, 6.6 g/s	1	75	miniK	This work (Kero), [146]
Jet-A, -	air, -	0.85	50	Cuenod	[101, 118]
Jet-A	air	0.65	102	Carlin 200CRD	[65]
Jet-A	air	0.82-1.1	102	NextGen	[142]

6.2.3 Heat flux and temperature measurements

To measure the heat flux density at different locations in the flame, a sensor (Huxeflux, SBG01) combining the principles of Gardon and of Schmidt-Boelter gauges is flush-mounted in a flat ceramic plate (CeraMaterials, 25.4 mm thick) and traversed in a plane perpendicular to the flame axis. The gauge is connected to a controlled water cooling system maintained at 20 °C. 2D heat flux mappings have been obtained by moving the burner horizontally and vertically in steps of 10 mm relative to the sensor. Each mapping is based on 122 individual measurements, gathered with the sensor remaining at least 30 s in each position and the ceramic plate allowed to cool down in between measurements.

The temperature at the specimen back face was measured with two thermocouples (TC) and the infrared (IR) camera, two complementary techniques that each have their challenges with burning composites. For TCs, it is difficult to maintain effective contact between the probe and the specimen as it degrades. The local surface temperature is measured with bare type K thermocouples (1.63 mm in diameter) positionned on the specimen backside, opposed to the flame stagnation point. The spatial temperature evolution on the specimen back face is assessed with an IR camera. The multispectral (MS) IR camera (Telops FAST-M350) is set up with a 50 mm lens and an eight position filter wheel. The results presented here are gathered using a neutral density filter and two narrow band-pass filters (Tab. 6.2). A decadic absorbance (OD) of three corresponds to a total transmittance of 10 % over the spectral range from 1.5 µm to 5.4 µm. The total focal plane area (FPA) of the indium antimodine (InSb) detector is 640 px × 512 px with a detector pitch of 15 µm. A FPA window size of 132 px × 132 px and an acquisition frame rate of 60 Hz are selected. The rotation of the filter wheel is synchronized with the frame rate and the exposure time is automatically

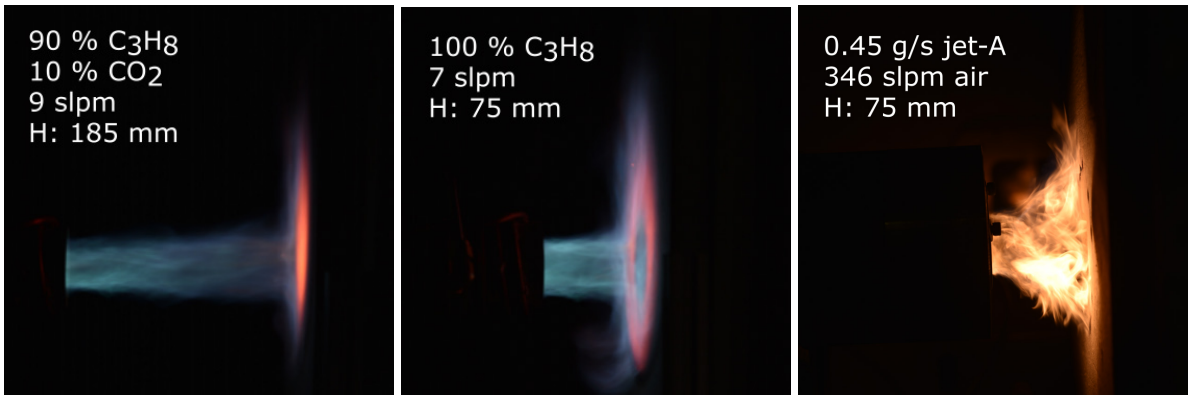

(a) Prop100 (b) Prop90 (c) Kero

Figure 6.2 Side view on the three flame configurations used in the small-scale fire test rig, all yielding $(116 \pm 10)\,kW/m^2$ and $(1100 \pm 80)\,°C$ at the specimen location. a) Pure propane flame. b) Propane flame with a fuel mixture made with 90 % C_3H_8 and 10 % CO_2. c) Kerosene flame.

set by the camera software based on these parameters. With IR thermography, the significant and rapid change in specimen emissivity is problematic as camera are typically calibrated using a fixed emissivity value. To obtain a reliable measurement of the temperature evolution, advanced signal processing tools must be implemented. Using the two-colour pyrometry approach and the image post-processing technique described by Pelzmann et al. [223], back face temperatures were obtained from regions of interest (ROI, 25 px x 25 px, Fig. 6.8b) located at the centre of the specimen back face without prior knowledge of the its emissivity.

Table 6.2 Filter configuration of the multispectral IR camera. The transmittance (τ) of the neutral density (ND) filter in position (Pos) 2 is evenly reduced across its spectral range (SR). The temperature range (TR) indicates the operating limits.

Pos	Description	SR [µm]	τ [%]	TR [°C]
2	ND filter, OD 3	1.50 – 5.40	0.1	539 – 1500
7	NP-3800-040	3.79 –3.82	70	297 – 1500
8	NB-3950-040	3.94 – 3.98	70	282 – 1500

6.3 Mechanical testing, mass loss and microscopy

Pristine composite specimens were monotonically tested according to ASTM D3039 [224] to determine their ultimate tensile strength (UTS, 4 repetitions). To assess the continuous mechanical degradation as a function of fire exposure duration, the pilot flame is shut off and the specimens are quenched with nitrogen after 15, 30, 45, 90, 300 and 900 seconds. Four coupons are tested for

each exposure time and flame configuration, thus the sample size is 24 for each flame configuration and 72 in total for specimens exposed to flame and subsequent load. Post-fire tensile tests on these specimens, realized on a MTS load frame with MTS 647 hydraulic wedges (69 bar operating pressure), provide insights on the laminate stiffness following short exposure times and on the residual fibre strength once the resin is depleted. Due to the fragility of the degraded coupons, it is not possible to install strain gauges or an extensometer and therefore the displacement of the upper crosshead is used to assess coupon extension for reference only. Burnt coupons are observed under a digital microscope (Keyence, VHX7000), before and after the tensile testing process. The oxidation of carbon fibres in specimens exposed to gas and kerosene flames is studied on 25.4 mm $\times$ 25.4 mm cutouts from selected specimens via scanning electron microscopy (SEM, JSM7600F, JEOL).

6.4 Results and discussion

6.4.1 Flame calibration

The burner flame is typically calibrated by measuring the flame temperature and heat flux density at a single fixed distance from the burner exit plane. In bench-scale testing, the measurements are performed at the stagnation point [100, 118], whereas in large-scale testing they are taken at slightly above [9, 37]. Fig. 6.3a presents a typical configuration during heat flux measurements. A pure propane flame (Prop100) is shown impinging on a ceramic fibre board. The free jet region (I) transitions into the stagnation zone (II) from which the wall jet region develops with a near field mixing zone (III) and a far-field zone with buoyant spreading (IV). Representative temporal profiles of the Prop100 propane flame and the kerosene flame (Kero) at the stagnation point are shown in Fig. 6.3b, revealing excellent stability, within the allowable range prescribed in the certification standards. The curves are averaged over 20 measurements for each flame configuration. However, single point measurements provides only limited information on the overall heat flux distribution experienced by a specimen. We therefore built heat flux density maps by translating the sensor on a plane perpendicular to the flame axis. By displacing the burner in 10 mm steps relatively to the sensor, transverse profiles (Fig. 6.4) and 2D heat flux maps (Fig. 6.5) were obtained.

Transverse heat flux density profiles for both propane flame configurations are compared against data presented by Tranchard [100] and Le Neve [225] in Fig. 6.4a, respectively for a small-scale research burner and a large-scale certification burners. The flame diameter of a large-scale oil burner is typically in the order of 305 mm, and the heat flux profile shown for a sub-region of 100 mm can be assumed to be well within the stagnation zone where little heat flux variation is expected. The oil burner data [225] shown in Fig. 6.4a was measured with a water cooled heat flux

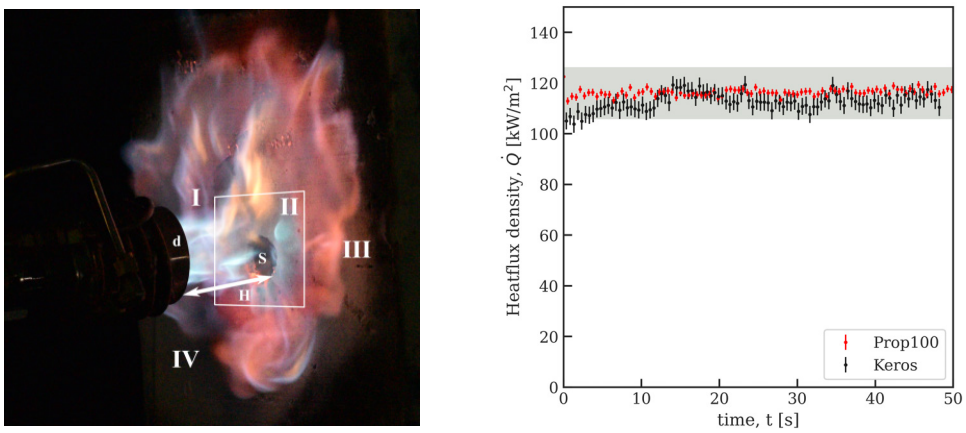

(a) (b)

Figure 6.3 (a) Axisymmetric gas flame impinging on a wall with different flow regimes, with H the standoff distance. S indicates the stagnation point and d is the burner diameter. (b) Heat flux density variation as a function of time, measured at the stagnation point for the kerosene and the pure propane flames.

meter from a flame that was previously calibrated with the BTU heat transfer device to a nominal heat flux of $\leq$106 kW/m^2. Measurements with the BTU heat transfer device are averaged over the length of the pipe exposed to the flame. As a result, these values are likely overestimations of the local heat flux densities close to the stagnation point and not suited for direct comparison with heat flux gauge measurements. The horizontal profile of the large-scale gas flame is slightly asymmetric with a narrow peak where the heat flux complies with the nominal values (gray region) and decreasing shoulders that quickly fall well below the minimal required value of 106 kW/m^2, probably due to heat loss to the surrounding.

Our measurement with the pure propane flame reveals a very uniform transverse heat flux density profile, within the target range of (116 $\pm$ 10) kW/m^2 for the whole width of 100 mm investigated. The difference in heat flux density over the width of the coupons (25.4 mm) is with 7.6 % in reasonable good agreement with the data reported by Tranchard [100], obtained with the same burner and identical operating conditions. The diluted small-scale flame (Prop90) features a similar heat flux density as the Prop100 configuration in the wall impingement area close to the stagnation point but shows, in overall, a higher heat flux density in the outskirts. As discussed by Chander [226], burner geometry, equivalence ratio and Reynolds number (*Re*) are all factors that directly influence the heat transfer characteristics. The higher overall heat flux density of the Prop90 flame may thus be attributed to a higher *Re*, and thus larger convective heat transfer contribution caused by its increased flow rate (9 slpm when compared to 7 slpm for Prop100).

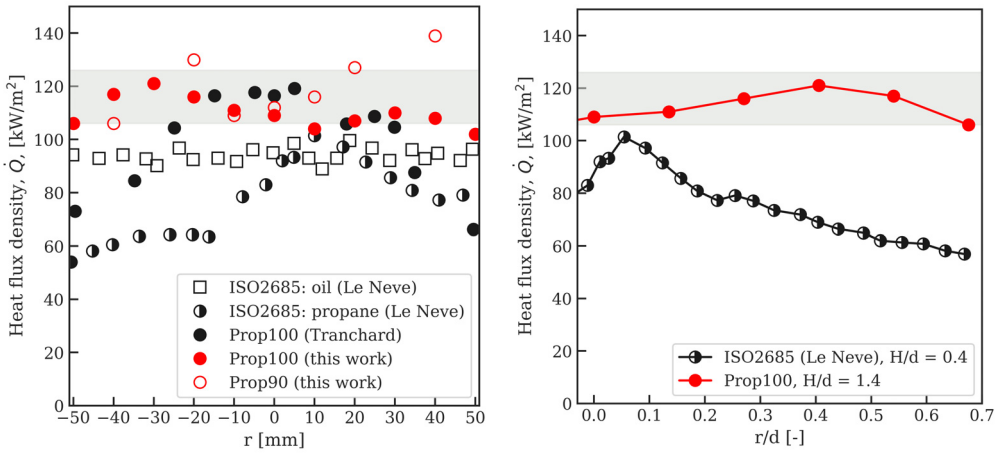

Figure 6.4 a) Transverse measurements centred at the stagnation point, compared against similar measurements from the literature. (b) Heat flux as a function of the radial distance (r) from the stagnation point, non-dimensionalized by the burner diameter, for the large-scale [225] and the small-scale propane burners at Φ=1.

For response to fire tests at all scales the size of the pilot flame must of course be commensurate with the size of the specimen exposed. In the ISO 2685 standard, the flame cross-section must be at least half as large as the major cross-section of the component to be tested. The AC 20-135 requires that sheet materials and panels have one side measuring at least 254 mm and that the test flame provides standard conditions over an area of 127 mm $\times$ 127 mm. Considering a typical large-scale test panel of 610 mm $\times$ 610 mm and the heat flux density profile reported by Le Neve [225], reproduced in dimensionless form in Fig. 6.4b, the outer edge of the specimen lies at $r/d = 1.2$ where the heat flux density has significantly decreased. This implies that the specimen experiences a significant heat flux and temperature gradient from the flame stagnation point to its edges and that only a limited central portion is exposed to the conditions prescribed in the certification standard. To allow the measured effects of flame exposure to be associated with flame characteristics in our bench-scale tests, the specimen size has been chosen to maintain conditions as uniform as possible over its width, in terms of heat flux density and temperature. As can be seen in Fig. 6.4, the 25.4 mm wide specimen correspond to a $r/d = 0.24$ when non-dimensionalized by the burner diameter. Over this width, all three flames used in this work have very uniform heat flux density profiles, ensuring that the coupons indeed experience uniform flame conditions in their central portion, where degradation is characterized in the following sections.

To further characterize the effective conditions experienced along the specimen height and width, the two gas flames have been mapped on a 2D grid, with the result presented in Fig. 6.5. The heat

flux gauge was unfortunately damaged before a similar mapping on the kerosene burner could be performed. The 2D heat flux contours shown in Fig. 6.5a and 6.5b also indicate zones within the test criteria shaded in grey, the exposed specimen central area is red. The Prop100 configuration (Fig. 6.5a) has an average value of 106.9 kW/m^2 with a standard deviation of 9.6 kW/m^2(9.0 %). Despite several attempts, we were not able to recreate the perfect axisymmetric pattern reported by Tranchard [100] with the same burner. The heat flux around the stagnation zone meets the certification requirements, although close to the lower acceptable limit of 106 kW/m^2, and the flame pattern is characterized by hotter zones at the outskirts of the stagnation zone where the air entrainment is non-uniform. For the diluted flame Prop90, the mean heat flux density over the entire measured area is 114.1 kW/m^2 and the standard deviation is 16.9 kW/m^2 (14.8 %). The inner reaction cone (brighter chemiluminescence) is further away from the wall, so that the hot jet impinging on the sensor can be expected to be mainly composed of hot combustion products, for this configuration. The maximum heat flux density should be highest in the stagnation point and decreases radially. However, this ideal behaviour is perturbed by buoyancy and air entrainment in the recirculation zone, yielding spots with elevated heat transfer below of the stagnation point and calmer regions above the stagnation point. The difference in the two 2D maps is visualized in Fig. 6.5c where the individual maps from Prop100 and Prop90 have been first averaged in square subregions of 20 mm and then subtracted. The color map shows the difference between the two heat flux profiles with respect to Prop100 in %. In the centre of the map, where our 24.5 mm wide specimens are located, the difference between the two flames is below 10 %. Overall, both flames configurations are suitable for bench-scale tests complying with AC 20-135 and ISO 2685 using the coupons size presented in this work, with tests on specimens up to 100 mm wide also possible.

The small-scale kerosene burner can be tuned by changing its nozzle and swirler, as well as by modifying its operating parameters such as supply and return pressures. In this study, the small-scale burner is operated at a fuel flow rate of 0.45 g/s and an air flow rate of 6.6 g/s, yielding a burner power of 22 kW and corresponding to an equivalence ratio close to stoichiometric, similar to that of the gas flames ($\Phi = 1$). Similar to the Prop100 flame, H/d is below one and the burner exit plane is positioned close to specimen surface. The turbulence introduced by the swirler was designed to ensure proper mixing of the fuel droplets and the supplied air [146] and visual inspection of the coupons shows repeatably homogeneous degradation across the entire specimen width (r/d = 0.13, Fig. 6.6).

6.4.2 Mass loss due to thermal decomposition

The mass loss of the specimens was measured by weighing specimens subjected to the flame for a duration ranging from 15 seconds to 15 minutes (900 seconds), the full duration of an ISO 2685

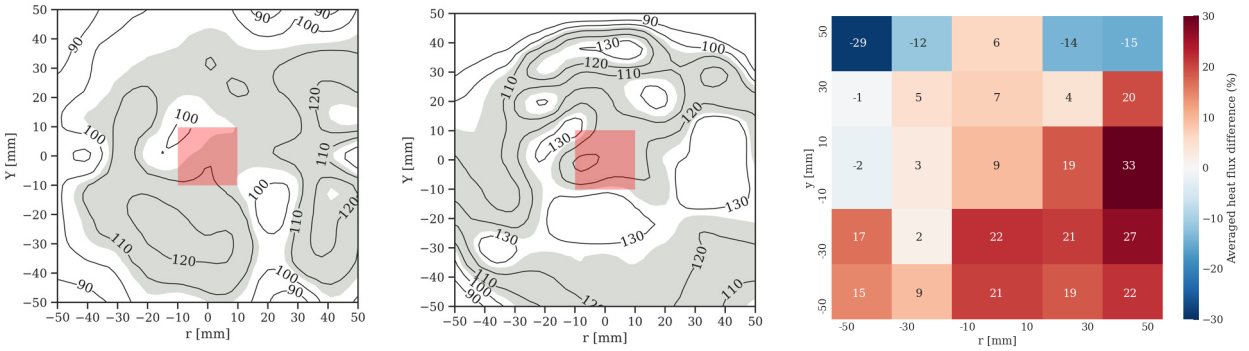

(a) Prop100 (b) Prop90 (c) (Prop100-Prop90)

Figure 6.5 a) and b), 2D heat flux density maps of the propane flames configurations. Zones that are within in the demanded range from 106 kW/m^2 to 126 kW/m^2 are shaded in grey, the exposed specimen central area is indicated in red. c) Averaged difference of the two maps in %, referenced to the pure propane flame (Prop100).

certification test. Following flame exposure, the coupons were quenched with a mild jet of inert gas and carefully removed from the specimen holder. Four specimens were tested for each exposure time per flame configuration. The decay in residual mass over time for the three flames is shown in Fig. 6.7. The mass loss within the first 45 s is comparable for all flame configurations (Fig. 6.7a) and driven by the onset of matrix pyrolysis. The Prop100 flame has by far the greatest variability (SD = 31.9 MPa) of mass loss for specimens quenched at 45 s. For CF epoxy specimens, the first 40 s mark the approximate duration of pyrolysates combustion [220] and is also the time frame where backside ignition is most likely to occur. The specimens tested consistently showed backside ignition for tests of 90 s and longer when tested with the gas flames, but under exposed to the kerosene flame, backside ignition occurred also in 30 s and 45 s tests, with the behaviour being inconsistent over repeated tests. The secondary flame on the backside increases the mass loss rate and contributes to the test variability. The diluted Prop90 flame closely followed the trend of the kerosene flame with low variability in the results. After most of the resin is depleted within the stagnation zone, the mass loss is mainly driven by char and fibre oxidation. Consequently, the slope of the mass loss curve decreases (Fig. 6.7b and Fig. 6.7c). For the kerosene flame, the variability appeared to increase with long duration tests, likely as a result of sporadic delamination enhanced by the turbulent impinging flame (Fig. 6.7b).

For comparison, data found in the literature for the mass loss for CF epoxy specimens of 2 mm thickness exposed to propane [101] and kerosene flames [118] are overlaid in Fig. 6.7b and Fig. 6.7c. For a test duration up to 45 s, the residual mass observed in our experiments is in good agreement with literature data with an average difference of 0.3 % for Prop100 flame and gas tests

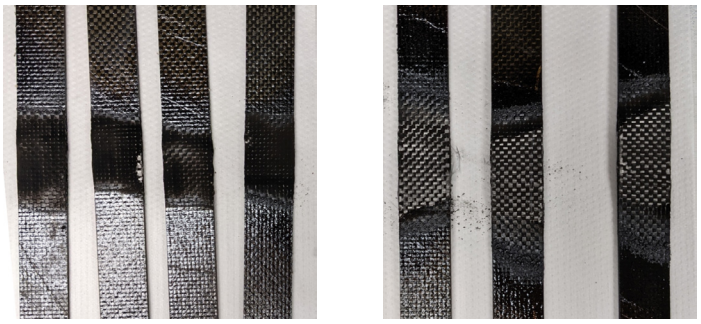

(a) (b)

Figure 6.6 Burnt specimen after being subjected to the kerosene flame for (a) 15 s and (b) 45 s. The composites are homogeneously damaged over the entire sample width of 25.4 mm with the extent of thermal damage decreasing in both vertical directions.

presented by Chazelle et al. [101] and an average difference of 1.62 % between our kerosene flame results and data from Schuhler et al. [118]. The deviation for longer exposures can be directly linked to the difference in specimen thickness and dimension, that allows comparatively more resin to be burnt. It is interesting to note, that the literature data reported in Fig. 6.7b and Fig. 6.7c indicate a higher mass loss for the propane flame below 300 s, which is in line with our observations, but opposed to the observations commonly done at large-scale. This further underlines that the gas torch design fuelled with 100 % propane is unable to recreate the test configuration involving the original large-scale gas burner.

For our experiments with nominally identical heat flux density and temperature, the pure propane flame appears to be significantly more aggressive in terms of massloss than the kerosene and the CO_2-diluted propane flame. This could be caused by slight differences in the equivalence ratio, as although all flames are close to stoichiometric, the amount of entrained air could not be controlled precisely with the propane burner. The addition of inert CO_2 with the fuel could limit the amount of excess air available in the flame exhaust, thus throttling char and CF oxidation. With our kerosene burner, the amount of air is precisely controlled and the stoichiometric conditions ensure that only limited amounts of oxidative species are present in the exhaust gases. Interestingly, the fuel dilution approach implemented here allowed the experimental realization of a gas-fuelled flame that behaves very similarly to the kerosene flame.

6.4.3 Back face temperature

Fig. 6.8c shows the comparison of the backside temperature evolution for the three flame configurations and test duration of 300 s, obtained by post-processing the IR image sequences in the ROI.

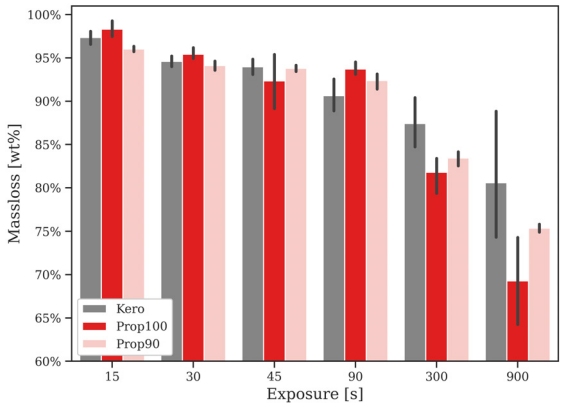

(a)

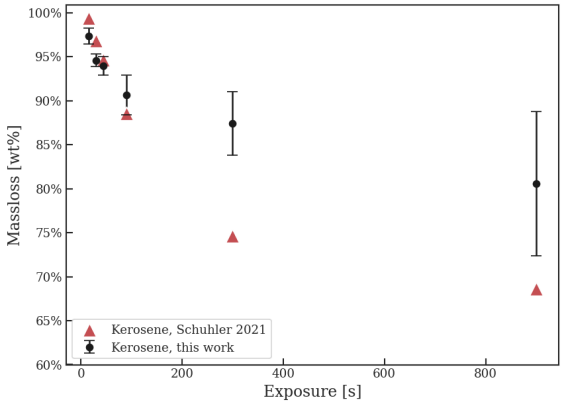

(b)

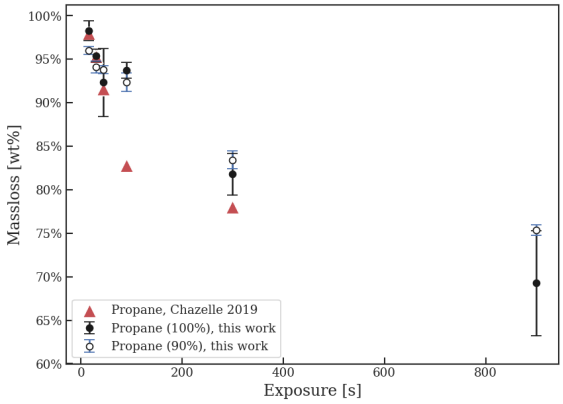

(c)

Figure 6.7 Residual mass of quenched CF/epoxy flames subjected to three different flame types for different duration, compared against the behaviour from similar CF/epoxy specimens subject to a) a kerosene flame by Schuhler [118] and b) a propane flame by Chazelle [101].

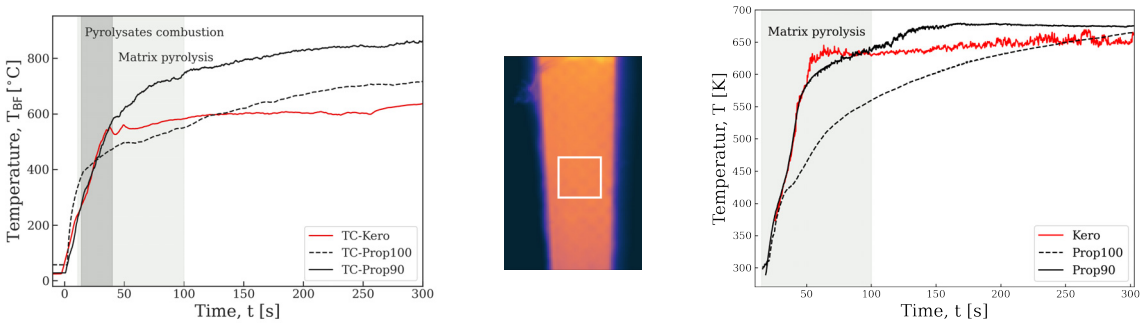

(a) (b) (c)

Figure 6.8 (a) Temperature curves obtained from TC probes located at the specimen backside, with temperature ranges shown for pyrolysis and outgassing combustion based on simulations by Langot [220]. (b) IR image of the coupon backside after an approximately 300 s exposure to the Prop100 flame, with the 25 px × 25 px ROI shown. (c) Temperature curves are obtained by averaging the pixels within the ROI for different flame configurations.

The wavelength range of the bandpass filter used in the camera cannot measure temperatures below 300 °C, thus the curves are slightly offset in time with respect to the TC measurements shown in Fig. 6.8a. Similar to the trends observed for the mass loss curves, the diluted propane flame (Prop90) and the kerosene flame show a good agreement for the back face temperature curves with an average temperature difference below 20 °C, but the pure propane flame shows significantly lower temperatures during the first minutes. The temperature curves obtained with thermocouples in Fig. 6.8a are taken at the same vertical position as the centre line of the ROI with the probe being located closer to the left specimen edge to minimize the visual obstruction in the IR camera field of view. Although the TC measurements show similar temperature curves as those obtained via IR measurements, the overall temperatures measured with TC are much higher. This is mainly due to two effects, with the first being the heat contributions from the ceramic shields and the second being an increased measurement uncertainty when the specimen ignites on the back and the flame engulfs the probe. A suitable post-treatment of this raw-data is very difficult to do as the contributions to the error budget vary rapidly over time. As a conservative estimate, the uncertainty for the TC readings is ±80 °C. The temperature curves taken from IR data are thus more reliable and representative for the backside temperature opposite to the flame stagnation zone.

TGA and DSC measurements provide means to relate thermal decomposition to temperature as the material heats up, although the heating rates representative of flame exposure cannot be reached using available hardware. From literature data, the onset of matrix decomposition for epoxy resins is expected at approximately 300 °C [88, 122]. Along with the temperature curves in Fig. 6.8a and Fig. 6.8c, the temperature ranges where pyrolysis takes place and where the pyrolysate outgassing

results in an external flame are showed as shaded regions, based on the numerical model presented by Langot [220]. The specimen surface is heated up in the first 10 s until the critical mass flow of pyrolysates can sustain combustion, after ignition at approximately 300 °C. The matrix in the thin laminates then burns rapidly until all volatiles are consumed. The matrix degradation then continues progressively until approximately 100 s when the maximum temperature is reached. From thereon, the temperature is expected to stabilize in a steady-state. As can be seen for example for the kerosene flame and Prop90 flame in Fig. 6.8c, this state is approached at approximately 240 s. The residual specimen properties from this moment until the end of the test have been averaged and summarized in Tab. 6.3.

Table 6.3 Summary of residual mass (m_{res}), back face temperature ($T_{max,BF}$) and UTS for three flames. Four specimens have been tested in each flame and test duration.

		m_{res} [%]		$T_{max,BF}$ [°C]		UTS [MPa]	
Duration	Configuration	Mean	Std	Mean	Std	Mean	Std
300	Prop100	81.8	2.4	748.0	39.3	43	28
	Prop90	83.4	1.0	829.3	60.7	26	2
	Kero	87.4	3.6	692.3	50.2	21	26
900	Prop100	69.3	6.0	737.2	59.3	7	11
	Prop90	75.4	0.6	805.6	31.2	8	5
	Kero	80.6	8.2	670.6	58.5	44	77

The IR temperature data was used to estimate the specimen heat-up rate (HUR) for each flame configuration and is shown in Fig. 6.9a. The HUR follow a power law behaviour for the Kero and Prop90 flame, asymptotically approaching zero as the system reaches steady-state. At the onset of pyrolyzate combustion ($t \approx 10$ s), the HUR estimated are approximately 16.5 K/s for the kerosene flame, 17.2 K/s for diluted propane flame and 8.7 K/s for the pure propane flame. The differences in HUR directly translates in the differences in the mass loss rate shown in Fig. 6.9b. The kerosene flame and the pure propane flame show a higher variability for a test duration of 15 s with a standard deviation of 0.011 g/s but otherwise the mass loss rate under a kerosene flame shows good repeatability (SD $\leq$ 0.004 g/s). The pure propane flame has the highest variability (SD = 0.016 g/s) for tests of 45 s where specimens sometimes ignited on the back side. The diluted propane flame shows a consistently decreasing mass loss rate for increasing test duration with good reapeatiblity (SD $\leq$ 0.005 g/s).

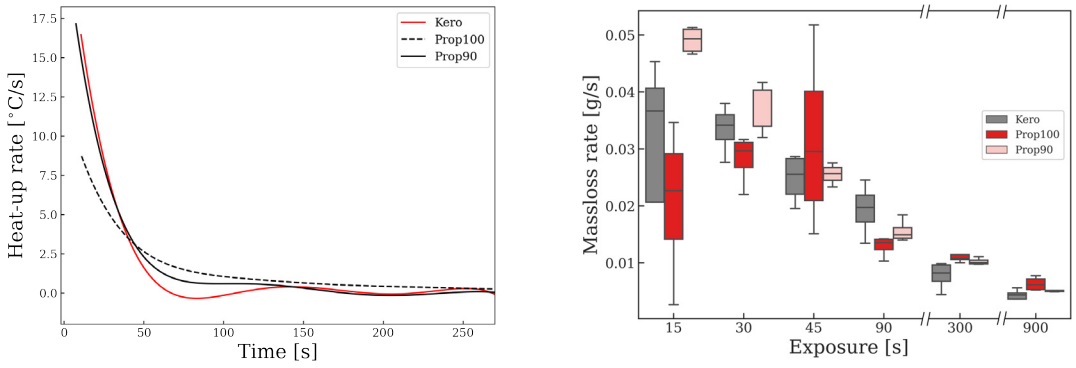

(a) (b)

Figure 6.9 (a) Heat-up rate (HUR) and (b) mass loss rate as a function of exposure time for different flame configurations. Samples tested under with the pure propane (Prop100) configuration heat-up at a slower rate and show a lower massloss rate compared to the other two flames for tests shorter than 300 s.

6.4.4 Residual mechanical properties

To understand the extent of the thermal damage for each flame exposure duration, the specimens have been tensile tested post-fire. The decrease of residual ultimate tensile strength (UTS) is shown in Fig. 6.10a. The UTS is drastically reduced in the first minute, from the rapid epoxy matrix decomposition. The diluted propane and kerosene flames result in very similar decrease in UTS as the test duration is extended. The pure propane flames, however, appear to allow specimens to retain a residual UTS twice as high as for the diluted gas flame and 1.7 times higher than for the kerosene flame. This can be in parts explained by considering the results obtained for the mass loss rate (Fig. 6.9b) and back face temperature (Fig. 6.8). By plotting the residual UTS as a function of the specimen mass loss, as shown in Fig. 6.10b, it becomes apparent that although all specimens lose mass at approximately the same rate, for pure propane flames, the associated decrease in UTS is delayed. This behaviour could be explained by the spatial distribution of the heat flux density over the specimen surface exposed to the flame, as this distribution determines the radius of the heat affected zone and the extent of thermal damage. For both the kerosene and diluted propane flame, although the average heat flux density is nominally the same, hot spots are more prevalent than for the pure propane flame. As a result, intense localized degradation can occur, resulting in weak spots compromising structural integrity comparatively faster than with the pure propane flame. Moreover, the initial drop in UTS is mainly associated with the weakening and combustion of the matrix, as shown in Fig. 6.10b. This can also be observed in the micrographs of specimens exposed to the kerosene and pure propane flames, respectively shown in Fig. 6.11a and 6.11b, where resin degradation is observed earlier in the former. After 90 s, the kerosene specimen

exhibits a completely resin-depleted fabric, that transitions away from the flame impinging point into a narrow zone of unburnt soot, followed by char and finally largely intact resin. The specimen exposed to the pure propane flame for the same duration also shows bare fabric, but the zone of partially charred resin is wider and the transitions between the zones are less distinct.

From 90 s onward, it is therefore the fibre degradation that defines the residual tensile strength. After 900 s, the specimen exposed to the kerosene flame shows burn-through, but the specimen that spent the same time under the pure propane flame maintained a uniform fabric surface. To identify the changes in the fibre microstructure resulting from the exposure to the different flames, Scanning Electron Microscope (SEM) images were acquired, with representative examples shown in Fig. 6.12. In these images, pitting is clearly visible, a degradation mechanism associated with exposure to high temperature oxidative atmospheres [219] that results in a rapid degradation of mechanical properties [227]. Specimens exposed for a shorter test duration did not exhibit pitting. The pit growth rate and spatial distribution are difficult to quantify from SEM images and consequently only general observations can be made. In the fibres subjected to the pure propane flame, pits appear to be smaller with a measured average diameter of 2.6 µm. The fibres burnt with the kerosene flame had deeper and more developed pits, that therefore decrease more significantly the material strength and can initiate failure at lower tensile stresses. The averaged pit diameter was obtained from the SEM image based on 13 measurements and is 5.8 µm. The pores on fibres exposed to the kerosene flames were also partly overlapping, with these instances not included in the statistical summary shown in Tab. 6.4. The SEM images demonstrate that although the heat flux and temperature are nominally the same, differences in flame chemistry can result in significant differences in microstructure evolution in degrading carbon fibres, and consequently on residual mechanical properties.

Table 6.4 Pitting diameter d of the fibres exposed to the kerosene and pure propane flame measured from the SEM images shown in Fig. 6.12. Smallest (min) and largest (max) values are indicated as well as the standard deviation (std) for the measurement.

	d(Kero) [µm]	d(Prop100) [µm]
average	5.8	2.6
median	5.5	2.6
min	3.9	1.3
max	9.4	4.7
std	1.6	0.9
specimen size	13	19

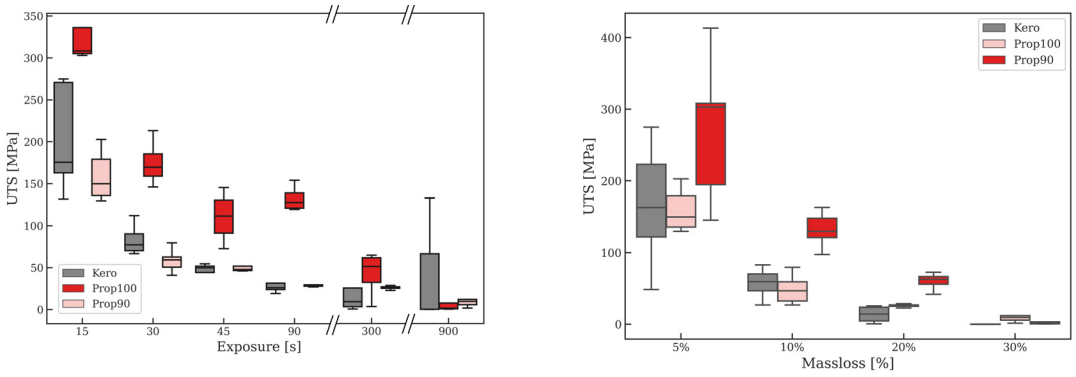

(a) (b)

Figure 6.10 Decay of specimen UTS for the three flame configurations, shown as a function of flame exposure time (a) and of the mass loss (b). Specimens have been quenched with a nitrogen stream to freeze their state of degradation.

6.5 Conclusions

This study focuses on the link between flame chemistry and the thermal degradation of CF epoxy composites, with the objective of bridging the gap between the many small-scale setups relying on propane flames to reproduce the conditions prescribed in certification testing where kerosene flames are mandated. For this purpose, three different flame configurations were calibrated, two propane flames and one kerosene flame, to nominally the same heat flux density and flame temperature of 116 kW/m^2 and 1100 °C. Mapping of the heat flux clearly demonstrated that the conditions at the stagnation point are not enough to properly describe the reactive flow.

Specimens were subjected to the flames for periods ranging from 15 s to 900 s and quenched with nitrogen to preserve the state of degradation at a given time. Back face temperature was measured using TC and IR camera in situ, mass loss and tensile strength were measured post-fire. The temperature evolution at the specimen back face opposite the stagnation zone for the diluted propane flame is in excellent agreement with the kerosene flame. As a general trend, the diluted propane flame resulted in a degradation behaviour similar to the kerosene flame. This manifests in similar mass loss over time as well as similar residual UTS for specimens burnt for the same time. The pure propane flame, the most commonly used in small-scale research facilities documented in the literature, resulted in a more homogeneously but less severe thermal degradation spread over a wider area. Tests using the pure propane configuration might thus tend to overestimate the specimen performance. Our tests have shown that it is however possible - by diluting and mixing the gas flame properly - to produce conditions that mimic very well the degradation dynamics resulting from exposure to a kerosene flame.

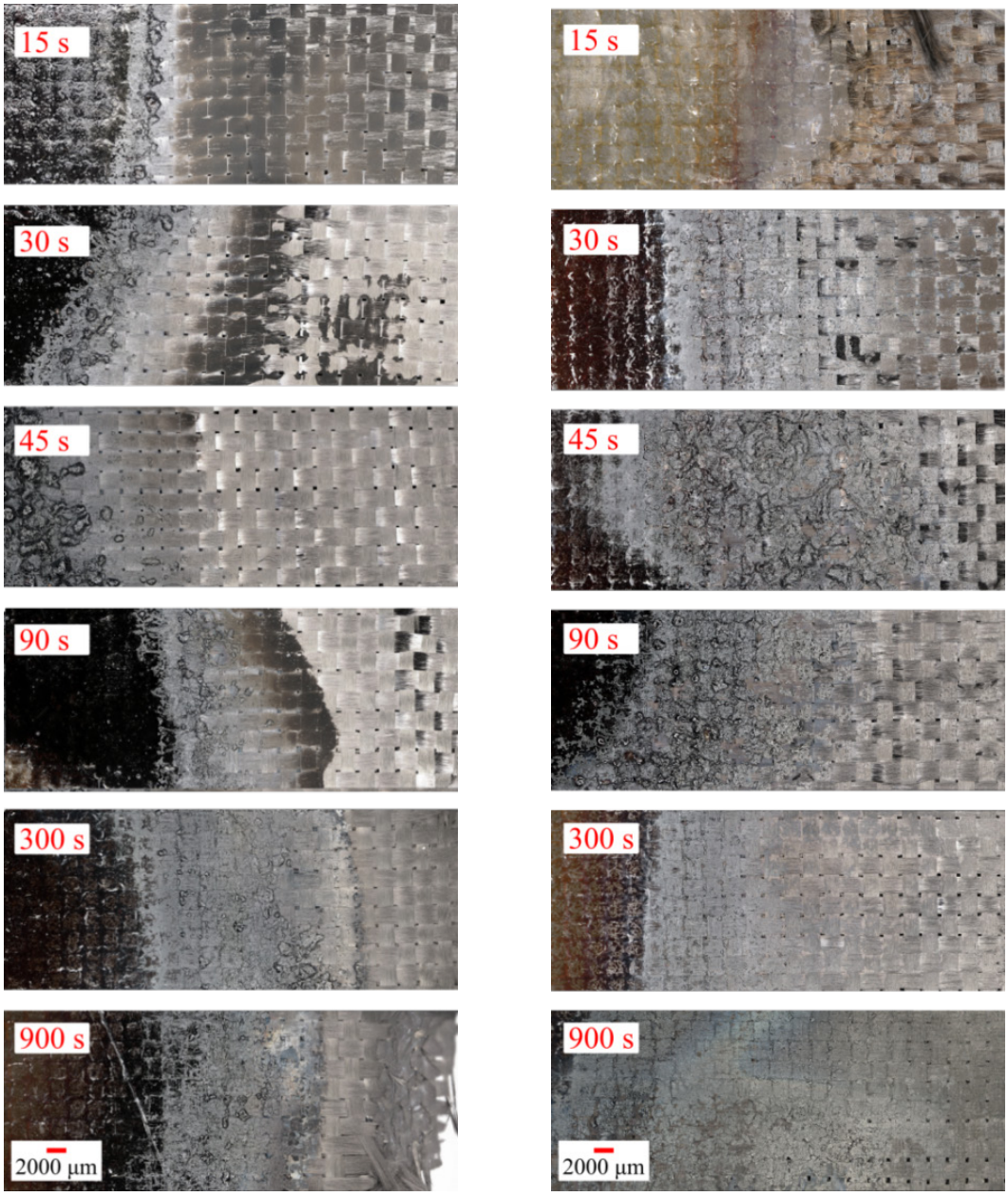

(a) Kero (b) Prop100

Figure 6.11 High-resolution microscopy of the quenched specimens in the stagnation zone of the impinging flame. Euclidean 3D reconstruction obtained from image sequences with variable focal lengths. The specimens on the left (a) were subjected to kerosene flames and the specimens on the right (b) to the Prop100 flame configuration.

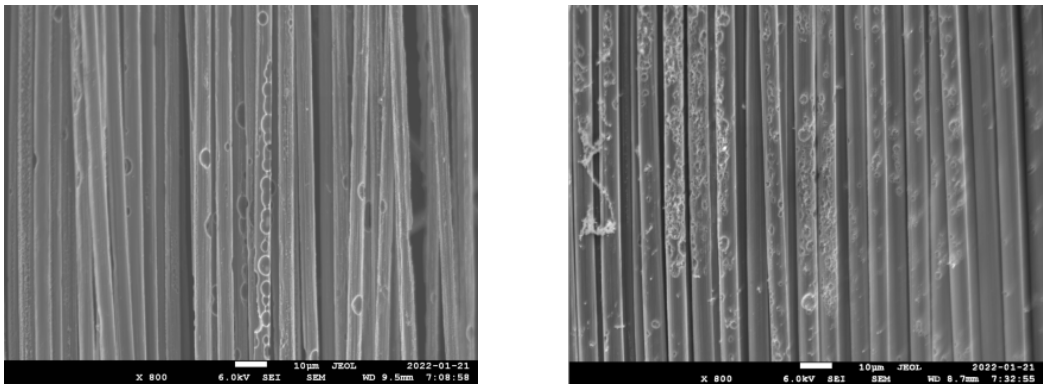

(a) (b)

Figure 6.12 Scanning electron microscope images of thermally degraded carbon fibres taken from failed specimens exposed to (a) the kerosene and (b) Prop100 flame configuration for 900 s.

This research presents a comprehensive experimental review of state-of-the-art small-scale fire test equipment. We demonstrate that the material degradation is dependent on the flame configuration used, even if the heat flux and temperature are nominally the same. The results highlight that gas torches remain simple and useful tools for material screening at a coupon level in the context of aerospace material evaluation, provided that the flame and burner parameters are well controlled to reproduce the conditions in kerosene fires. Future work should focus on the fibre oxidation behaviour as a function of flame chemistry, adding the effect of stoichiometry, and extent the experiments to the application of simultaneous thermal and mechanical load.

Declaration of competing interest

The authors declared no potential conflicts of interest with respect to the research, authorship, and/or publication of this article.

Funding

We are grateful for financial support from the Natural Sciences and Engineering Research Council of Canada (NSERC/ CRSNG), through grant no. CRDPJ 478687-15, and the assistance of the partners of the CRIAQ ENV- 708 project is acknowledged. P. Chávez-Gómez is grateful to the National Science and Technology Council of Mexico (CONACYT) for his doctoral scholarship.

Acknowledgements

The authors wish to thank Philippe Massé for the specimen preparation and his valuable support in the execution of the experimental campaign. We wish to extend our gratitude to Rodrigue Beanini for assisting the heat flux measurements and to Nicolas Jacquot for preparing the micrographs.

CRediT authorship contribution statement

T. Pelzmann: Conceptualization, Methodology, Validation, Formal analysis, Investigation, Writing - Original Draft, Writing - Review & Editing, Visualization **P. Chávez-Gómez:** Investigation, Methodology, Writing - Review & Editing **É. Robert:** Funding acquisition, Supervision, Writing - Review & Editing **M. Lévesque:** Funding acquisition, Supervision, Writing - Review & Editing **L. Laberge Lebel:** Writing - Review & Editing.

CHAPTER 7 GENERAL DISCUSSION

7.1 Discussion of main results and impact

A main objective of this thesis was the design, fabrication and calibration of versatile research infrastructure to study the fire resistance behavior of polymer-matrix composite under conditions similar to large-scale certification testing. One of the key components of this facility is the burner, that must deliver a "standard flame" of prescribed flame temperature and heat flux density. We have shown that our small-scale kerosene burner is capable to create such flames that meet the nominal conditions, with a significantly lower burner power and flame volume compared to the burners used in certification laboratories. This makes our facilities ideal to evaluate material performance using small coupon sized samples rather than large panels, enabling quick and cheap evaluation of material systems and fireproofing solutions. Additionally, we have demonstrated that these two properties, temperature and heat flux density, are not sufficient to fully characterize the conditions a material is exposed to during a flame attack. Our results clearly show that differences in sample degradation and residual properties can be caused by changes in flame chemistry, momentum or heat flux distribution.

The contributions of the present work are advancing the current state of knowledge in three closely related field of fire resistance evaluation for composite materials: the calibration of small-scale flame-based testing facilities, the monitoring of surface temperature through infra-red imaging and the investigation of the effect of flame chemistry on material degradation. In the following sections, the main contributions made through this work for each of these problems will be presented and discussed, followed by a assessment of the expected impact in the field of composite fire testing for aerospace applications.

7.1.1 Calibration of small-scale burners

Comparing any bench-scale fire resistance tests performed in the settings of a research laboratory with full-scale certification tests carried out in dedicated laboratories across different scales comes with several challenges. For example, the flame temperature is prescribed by the standard documents as (1100 ± 80) °C, a value that lies well below the temperatures expected from equilibrium calculations when the reactants are provided in stoichiometric proportions, for kerosene or for simpler gaseous fuels such as propane. To achieve this desired temperature, the flame can either be operated with lean or rich mixtures, resulting in drastic differences in the composition of the exhaust gases, affecting the thermal degradation of the sample, as discussed in Ch. 6. These differences can

also complicate flame calibration, as the certification standards do not provide guidance for the interpretation of the raw signals provided by the prescribed calibration tools (thermocouples and BTU heat transfer device). The tests conditions are therefore not defined in terms of the real flame parameters but rather as the conditions assessed through the crude calibration tools imposed by the standards. Consequently, the effective conditions in each testing facility become dependent on the approach used to achieve the desired flame characteristics, and often varies with atmospheric conditions, equipment wear and probe fouling.

For temperature measurements, the signal from uncoated thermocouple is often taken at face value for calibration in the industry. However, thermocouple probe readings in a combustion environment are significantly altered due to convective, conductive and radiative losses. Catalytic heating effects can conversely result in an overestimation of the gas temperature in flame environment, especially when platinum-based thermocouples are used. While temperature readings from our small-scale tests were corrected, we have yet to establish dedicated test campaigns with our collaborating fire test facilities to do the same at large-scale, although estimation of the associated errors are possible. Based on the adiabatic flame temperature of kerosene (≈2093 °C) and considering some heat loss to the environment as well as lean conditions, the flame temperature of the large-scale burner is expected in the range from 1500 °C to 1900 °C. Consequently, the error of the uncorrected thermocouple data amounts to several hundred degrees Celsius. This implies that our calibrated small-scale flame is most likely colder than an actual large-scale standard flame, that relies on uncoated and uncorrected thermocouple readings. As our small-scale burner can easily be calibrated to other (higher) temperatures, this problems is merely a question of properly defining test conditions, i.e. does one want to target effective conditions that meet the certification standard requirement or aim to recreate the likely harsher conditions encountered in large-scale certification tests calibrated using the crude approach typically implemented. The solution to this problem can thus only be stem from in a closer collaboration between large-scale test facilities and research, to establish what the actual flame temperatures are and to use these actual values for research tests rather than the nominal values from certifications. These changes should also be included in revised versions of certification standards.

The second important characteristic of the flame, its heat flux density, was also assessed with different tools in our work. We have shown that heat flux readings using cooled thin film gauges (TFG) embedded in non-cooled fibre board, although recreating a jet impingement characteristic for the test, tend to overestimate the flame heat flux density compared to those obtained by the BTU heat transfer device. The differences can be explained by the presence of a stagnation point when using TFGs and by the spatial averaging inherent to the use of the BTU heat transfer device. There is therefore a need to further investigate and mitigate this wall temperature discontinuity effect. A numerical correction of TFG data from non-cooled enclosures has been provided by Talib et al. [155],

but the approach takes only a laminar boundary layer into consideration. The BTU heat transfer device, despite its ease of fabrication and its simple measurement principle, comes with its own challenges. As our results show, the soot deposition on the tube affects the measurement and leads to lower heat flux density readings over time, mainly driven by this effect. Although we were able to approximate the signal decrease with simplified linear models, we find that combustion induced fouling behavior requires a closer look at the factors affecting the accuracy and repeatability, in particular given the importance of this device in fire testing. We proposed a scaling methodology to built a similar test device suited for small-scale flame. Measuring heat flux density at small-scale using the TGF and the scaled BTU device yields similar discrepancies as at large-scale, which makes us confident that the physics at play were successfully maintained.

7.1.2 Infrared surface temperature measurements on degrading solids

An important aspect of this work was to monitor the sample temperature during thermal degradation, as many of the sample properties are inherently temperature dependent. Infrared thermography allows temperature distributions to be obtained with high temporal and spatial resolutions. As our results have shown, conventional *ab initio* IR thermography relying on the estimation of fixed emissivity values significantly increases the error budget of the measurement. In doing so, two important factors are neglected. First and foremost, as the sample burns the surface changes heterogeneously resulting in a spatial variation of emissivity. Secondly, emissivity depends among other factors on temperature. We have shown that counter intuitively, emissivity decreases in the infrared spectrum as the sample darkens in the visual spectrum. We have presented a radiation model that takes into accounts in great details the features of the experimental tools used, starting with nine unknowns and then simplified based on well-defined assumptions to only two unknowns that can be experimentally assessed. Already with this degree of simplification, the two color technique yields more accurate measurements that were validated against independent measurement methods. For most of our tests, we confined our analysis to situations where the camera can be positioned close to the sample surface, thus justifying the assumption of negligible atmospheric contributions. However, the thin boundary layer next to the surface of a burning composite is at a comparatively lower temperatures, and can potentially contain pyrolyzates that absorb portions of the infrared spectrum of interest, leading to error contributions that we could not account for in our work. Due to the filter selection, our measurements were confined to temperatures above 300 °C and so this effect could not be assessed. For studies at lower temperatures, a radiant heat source might be better suited compared to an external flame, as it allows to remain below the flammability limit while still exceeding the onset of pyrolysis. In such a scenario, the filter selection will have to be adapted accordingly. The step-wise complication of our radiation transfer model offers many

research opportunities for future studies.

7.1.3 Effect of flame chemistry on thermal degradation

The calibration of different flames of nominally identical heat flux density and flame temperature was motivated by the hypothesis that the flame chemistry plays an important role in the flame-mediated degradation of polymer matrix composites. However, this implies also a need for the characterization of the actual flame chemistry. To change flame chemistry, we used different fuel types and calculated the effective equivalence ratio achieved with the different fuels. We demonstrated that the conditions prescribed by the certification standards can indeed be achieved using several different sets of operating parameters for the burners, in terms of fuel used, equivalence ratio, turbulence level in the flame and standoff distance between the burner and the sample. The effect of some of these parameters was correlated with the thermal degradation rate of epoxy matrix carbon fibre reinforced composites. For instance, exposed to a pure propane flame, specimen retained a residual ultimate tensile strength almost twice as high as when tested with a kerosene flame. These observations are however indirect, with the actual effect on thermal degradation likely mediated through the concentration of reactive radical species present in the flame atmosphere. The implementation of flame diagnostic tools such as laser induced fluorescence could enable the quantitative measurement of some of the radical species involved, with high temporal ans spatial accuracy. More specifically, by measuring the spatial distribution of the $OH^{\bullet}$ radical concentration, the spatial distribution of heat-releasing hydrocarbon combustion reaction can be referred. The experimental constraints of our setup have unfortunately not allowed the implementation of this technique, although the test chamber has been designed to accommodate laser diagnostics. Sapphire windows transparent to the laser beam can be installed with on the chamber walls for these tests.

The fuel and oxidizer flow rates for the kerosene burner can be precisely controlled, but the design of the gas torch makes it difficult quantify the amount of air drawn in the torch. Consequently, for our measurements with gaseous flames the equivalence ration cannot be known precisely. A first attempt to close the air holes with a collar connected to a mass-flow-controlled air supply was not able to recreate the flame shape obtained with an unmodified torch. Alternatively, particle image velocimetry (PIV) is the method of choice to visualize the local velocity field. This could enable the calculation of the oxidizer flow rate during burner operation. While the kerosene burner remained the main focus of this work, an additional analysis of the flow characteristics of the gas burner remains an interesting topic, mainly because this exact model is used by several other research groups.

7.1.4 Impact of the work

The main impact result of this work is to enhance the understanding of the failure modes of carbon fibre composites under flame attack with suitable experimental infrastructure. The development of a novel experimental test bed allows to mimic the conditions present in fire-prone areas of aircraft engines and to analyze key material parameters of great interest not only for the problem at hand but also for a variety of research questions in the field of combustion and fluid dynamics. The results gathered in this facility support high impact research on the behavior of combustible materials under flame attack and assist the development and evaluation of new material systems without relying solely on costly certification experiments. The work described here is even more crucial because the new regulations covering fire testing of aero-components have been reviewed by the FAA (Federal Aviation Association) and previously admissible gas burners have been banned. Thus a reliable and meaningful assessment of material properties degradation using a well-controlled oil burner is necessary for the aerospace industry to be able to make proper design and material decisions as well as passing certification processes.

CHAPTER 8 CONCLUSION AND RECOMMENDATIONS

8.1 Conclusion

The work presented here aims to contributing to the ongoing worldwide efforts addressing the current limitations of fire testing for aerospace composite materials used as firewalls. Common industrial practice is based on the use of very conservative assumptions, as no comprehensive guidelines are available to cover the spectrum of modern material system, combustion diagnostics and numerical modelling. Meanwhile, the fire research community has in recent decades focused mainly on tests using gas torches and simple hydrocarbon fuels such as propane or propene. The lack in harmonized equipment for bench-scale tests, with detailed operating parameters and calibration procedures often not disclosed, makes it difficult to compare or recreate experiments from the literature and compare them against the outcome of full-scale certification tests.

An important first step in assessing the failure behavior of aerospace-grade carbon/fibre composite materials was thus the development of a novel experimental facility allowing the creation and detailed characterization of the conditions potentially present in the fire zones of aircraft engines. The research facility developed is unique in the world, enabling to test under flame, under load, and with a fast stream of air as cooling back-flow. Most importantly, the setup features a small-scale kerosene burner developed in-house, that can be operated with a thermal power as low as 5 kW and a corresponding flame diameter of 5 cm, which makes it ideal for testing coupons sized samples. The nozzle used for fuel atomization has a large influence on the diameter, volume and shape of the flame. With the selection of fuel bypass nozzles, a stable atomization behavior is maintained over a wide range of flow rates and hence the power can easily be increased up to 35 kW and higher. Another important hardware choice made in the development of this burner is the implementation of an adjustable swirler. Our use of a 3D printed swirler provides control over the flame shape and turbulence intensity without changing the reactants flow rates. This therefore provides a mean to control the heat flux density on the samples theoretically independently from the flame temperature. The close coupling between these two parameters is difficult to avoid, and often results in one of the parameters significantly exceeding the target values in large-scale certification tests, as discussed in Ch. 2. These factors make our small-scale burner ideal not only to analyze material degradation for the problem at hand but also for a variety of research questions in the field of combustion and fluid dynamics for a wide range of applications.

Our detailed experimental study was first aimed at characterizing and calibrating our small-scale burner to identify a set of operating conditions meeting the certification requirements in terms of

temperature and heat flux density. Instead of using only the conventional BTU heat transfer device, a scaled-down version was constructed to meet the dimensions of our flame, to keep similarity across test scales. These measurements where then compared to those gathered with a water-cooled thin-film gauge embedded in a ceramic fibre board. For similar burner operation conditions, the thin film gauge indicates slightly higher values as it sits at the stagnation of the flame and does not suffer from the spatial averaging inherent to the BTU heat transfer device. Comparison between the calibrations carried out in our small scale test rig and full-scale certification conditions was done through a collaboration with three fire testing facilities: the NRC fire testing laboratory in Ottawa, Pratt & Whitney Canada in Longueuil and Resonate Testing Ltd in Northern Ireland. We were able to perform large-scale calibration tests using both the BTU device and the TFG. The two main findings are that TFG measurements overestimated the heat flux density in a similar manner as in our small-scale tests and that the carbon built-up on the BTU heat transfer device during calibration is significant, leading to an apparent heat flux decrease. Since the testing facilities are required to meet the prescribed flame conditions, the burner power is often increased to compensate, leading to overly aggressive test conditions. Ch. 4 also discussed the challenges of temperature calibration for fire testing at different scales. Data from large-scales rely typically on uncorrected data whereas the flame temperature readings from our small-scale tests have been corrected for radiation losses. For the sample width selected for coupon testing, this means that the flame has a temperature and heat flux density meeting the certification requirements across the entire sample width, enabling a direct link to be drawn between these conditions and the resulting degradation of the material, as discussed in Ch. 6.

Temperature measurements are not only a challenge in the hot gas phase but also at the surface of and within the degrading sample. Different approaches have been implemented to measure this important quantity: thermocouple probes have been placed on the sample back surface and fine wire thermocouples were imbedded between plies prior to composite curing. Additionally, a novel infrared thermography has been developped to obtain the temperature of the composite samples as they are thermally degrading. From this three approaches, IR thermography is the only one that allows temperature measurements with high spatial and temporal accuracy, without involving probe contact with the sample. Used in a conventional manner, the sample emissivity needs to be known or estimated to convert the radiance data to temperature. However, our comprehensive measurement campaign involving different types of materials clearly showed that the sample emissivity significantly changes with temperature and that emissivity values obtained at room temperature are not well suited to provide meaningful values for IR thermography at elevated temperatures. To circumvent this problem, we used a multispectral infrared camera with an integrated filter wheel to measure the signal in two narrow bands. The detailed image post-processing technique presented in Ch. 5 allows the measurement of the surface temperature of a thermally degrading material,

without prior knowledge of the surface emissivity. By comparing the results to thermocouple readings and to a conventional IR thermography approach, we could show that the difference in using a fixed emissivity could easily exceed 50 °C with an additional error of 50 °C, depending on the exact configuration. Using the 2C technique, the corrected signal deviates not more than 15 °C on overage from the thermocouple readings with an error below 30 °C. The method described is of interest to a wide range of test scenarios where the sample temperature of a thermally degrading material is of interest. More importantly, our results clearly demonstrate that IR thermography in fire testing using fixed emissivity values is not capable of achieving the accuracy of ±10 °C or less often claimed in the literature.

In the final part of the thesis, we investigated the effect of flame chemistry on the sample degradation behavior for carbon/fibre epoxy composites. Two gas flames and a kerosene flame were calibrated to the same nominal heat flux density and flame temperature. Using a carbon dioxide diluted propane flame, we were able to induce a degradation behavior very similar to that observed with the kerosene flame, a significantly more complex burner to implement, in particular with respect to mass loss rate and residual mechanical properties. The pure propane flame operated following protocols found in the literature resulted in a larger variance between tests and an overall overestimation of the sample performance. Although it is preferable to test with a flame chemistry similar to the large-scale test conditions, we showed that it is possible to obtain similar effects with a modified gas-fueled flame.

To conclude this work, we have designed and developed a versatile test bed that is able to provide a wide range of experimental conditions and as such to provide unconvoluted experimental data suitable for model validation, as for instance specimen temperature and emissivity during thermal degradation. The novel experimental facility can recreate the hazardous conditions present in the fire zones of aircraft engines, such as those resulting from leaking fuel lines. We also established appropriate measurement techniques to measure key physical and mechanical quantities that characterize the thermal degradation process. Instead of the simple pass/fail verdict provided by conventional certification testing, the material behavior under flame attack conditions can be continuously monitored in our experiments. This work is therefore intended to enable the investigation of failure modes for aerospace-grade composite components under flame attack in cheap coupon-based tests and to assist in the development and evaluation of new material systems without relying solely on costly certification experiments.

8.2 Directions for future research

This thesis presents a unique small-scale approach for fire resistance testing and addresses commonly under appreciated effects in flame calibration as well as in surface temperatures using in-

frared thermography. At the conclusion of this thesis, further work remains on these research topics :

- The role of experimental methods in flame calibration

A lack in harmonized equipment and calibration methods across different scales is currently a major hindrance in comparing and sharing results between research groups. In collaborating with certified test facilities, properly corrected flame temperature measurements for large-scale "standard" flame should be performed. With such data publicly available, researchers could then calibrate their small-scale setups with respect to these actual flame temperatures. Another important step in supporting material research and model development is to establish equipment and operating conditions for standard use cases. The fouling of the BTU heat transfer device requires more studies which will benefit research and industry alike.

- Surface temperature measurements in fire testing

Most numerical models focus on the hot face of the sample where the flame is impinging and thus the ignition is initiated. Reliable and accurate temperature measurements on the hot sample face are thus an important contribution to the ongoing model development efforts. The infrared thermography technique presented in this thesis was implemented on the cold side of the laminate and many more factors will have to be taken into account when attempting to measure a surface temperature "through-flame". The radiative transfer model will have to consider additional factors such as the signal attenuation by the pilot flame but also by the surface flame eventually developing on the sample. The surface emissivity and temperature are expected to change at a high rate and to exhibit steep spatial gradients. In consequence, the selection of hardware and camera acquisition parameters and the deconvolution of individual contributions to the signal received by the camera are among the challenges that should be tackled in such studies.

- Flame chemistry effects

Probably one of the most challenging, but scientifically most promising research opportunity come from the integration of advanced diagnostics in the existing setup. As has been outlined in the discussion, the spatial mapping of radical species and reaction rates provides a new opportunity to go beyond the assumption that only the flame temperature and the heat flux control the degradation rate at the surface of the material. The implementation of laser spectroscopic techniques could help to study the chemical processes involved in the thermal degradation and to potentially link flame radicals to local sample damage.

- Additional tests constraints

With the versatile small-scale test bench available, the next logical step is to combine tests under kerosene flame with simultaneous testing under load or compression. Moreover, additional constraints such as cooling backflow or vibration, although already available as proof-of-concept, could be integrated in parametric studies. The experimental integration comes with a lot of challenges, for example interference of resonance frequencies and the management of large amount of gas needed for cooling the back face, without inducing perturbation on the pilot flame. In particular, the combination of tests under load and kerosene flame would complement the already existing tests data considering only gas flames.

Fire resistance testing does not stop at fire walls and the kerosene burner has a wide range of accessible operation conditions. The burner can be used for tests of cabin interiors or other fire safety critical applications. Most importantly, it is a research device that lends itself well for fundamental combustion studies. In a complementary approach with numerical tools, the burner can serve to investigate dynamics of liquid fuel non-premixed swirl-type flames or help in soot particle studies.

REFERENCES

[1] P. E. Irving and C. Soutis, *Polymer composites in the aerospace industry*. Woodhead Publishing, 2019.

[2] J. T. Daniels. (2017) Smithsonian national air and space museum. Accessed on: 2017-11-05. [Online]. Available: https://airandspace.si.edu/exhibitions/wright-brothers/online/fly/1903/construction.cfm

[3] P. Doornbos. (2016) Boeing 787 dreamliner assembly. Modern Airliners. Accessed on: 2017-11-17. [Online]. Available: http://www.modernairliners.com/boeing-787-dreamliner/boeing-787-dreamliner-assembly/

[4] S. Hariram, P. Philipp, and D. Dummeyer. (2010) Fire protection: engines and auxiliary power units. Boeing Aeromagazine. Aero quaterly QTR_04/10; page 16. [Online]. Available: www.Boeing.com/commercial/aeromagazine

[5] D. E. Sikoutris, "Fire Response of Composite Aerostructures," PhD Dissertation, University of Patras, 2012.

[6] A. G. Gibson, "The Integrity of Polymer Composites during and after Fire," *Journal of Composite Materials*, vol. 38, pp. 1283–1307, 2004.

[7] V. Apte, *Flammability testing of materials used in construction, transport and mining*. Woodhead Publishing, 2006.

[8] N. Girard and J. Kneepkens. (2013) Rulemaking cooperation guidelines for the federal aviation administration and the european aviation safety agency. [Online]. Available: https://www.faa.gov/regulations_policies/rulemaking/media/FAAandEASA.pdf

[9] *Aircraft — Environmental test procedure for airborne equipment — Resistance to fire in designated fire zones*, International Organization for Standardization Std. ISO 2685:1998, 1998.

[10] D. E. Rosner, "On the effects of diffusion and chemical reaction in convective heat transfer," Aerochem Research Labs Inc., Princeton, NJ, Technical report AD0416013, 1959.

[11] D. E. Rosner, "Convective heat transfer with chemical reaction," Aeron. Res. Lab. Rept. ARL, Technical report Report. 99 Part J. AD 269816., 1961.

[12] W. A. Gray, J. K. Kilham, and R. Müller, "Heat transfer from flames," NASA STI/Recon, Technical Report A, 1976.

[13] J. E. Anderson and E. F. Stresino, "Heat transfer from flames impinging on flat and cylindrical surfaces," *Journal of Heat Transfer*, vol. 85, pp. 49–54, 1963.

[14] J. K. Kilham and M. R. I. Purvis, "Heat Transfer From Normally Impinging Flames," *Combustion Science and Technology*, vol. 18, no. 3-4, pp. 81–90, 1978.

[15] C. E. J. Baukal, "Heat transfer from a flame impingement normal to a plane surface," PhD dissertation, University of Pennsylvania, Philadelphia, PA, USA, 1996.

[16] S. Sudheer and S. V. Prabhu, "Partitioning of convective and radiative heat fluxes absorbed by a lumped body engulfed in a diffusion flame," *Fire Technology*, vol. 51, pp. 801–822, 2015. [Online]. Available: http://dx.doi.org/10.1007/s10694-014-0412-7

[17] R. J. Asaro and M. Dao, "Fire degradation of fiber composites," *Marine Technology and SNAME News*, vol. 34, pp. 197–210, 1997.

[18] M. Dao and R. J. Asaro, "A study on failure prediction and design criteria for fiber composites under fire degradation," *Composites Part A: Applied Science and Manufacturing*, vol. 30, pp. 123–131, 1999.

[19] R. J. Asaro, B. Lattimer, and W. Ramroth, "Structural response of FRP composites during fire," *Composite Structures*, vol. 87, pp. 382–393, 2009.

[20] A. Johnston, A. Jodoin, and J. MacLaurin, *Evaluation of fire performance of composite materials for aircraft structural applications*. Society of Manufacturing Engineers, 2000.

[21] T. N. A. Browne, "A model for the structural integrity of composite laminates in fire," PhD dissertation, Newcastle University, 2006.

[22] A. Hörold *et al.*, "Protecting the structural integrity of composites in fire: Intumescent coatings in the intermediate scale," *Journal of Reinforced Plastics and Composites*, vol. 34, pp. 2029–2044, 2015.

[23] C. Lautenberger and C. Fernandez-Pello, "Generalized pyrolysis model for combustible solids," *Fire Safety Journal*, vol. 44, pp. 819–839, 2009.

[24] D. Rasbash, D. Drysdale, and D. Deepak, "Critical heat and mass transfer at pilot ignition and extinction of a material," *Fire Safety Journal*, vol. 10, pp. 1–10, 1986.

[25] C. K. Law, *Combustion physics*. Cambridge university press, 2010.

[26] T. Kashiwagi, "Polymer combustion and flammability—role of the condensed phase," *Symposium (International) on Combustion*, vol. 25, pp. 1423–1437, 1994.

[27] L. Jianjuan and O. Yuxiang, "Theory of flame retardation of polymeric materials," in *Polymer combustion*. De Gruyter, 2019, ch. 1, pp. 1–44.

[28] A. M. C. Janse *et al.*, "Combustion kinetics of char obtained by flash pyrolysis of pine wood," *Industrial & Engineering Chemistry Research*, vol. 37, pp. 3909–3918, 1998.

[29] D. Q. Dao *et al.*, "Determination of characteristic parameters for the thermal decomposition of epoxy resin/carbon fibre composites in cone calorimeter," *International Journal of Hydrogen Energy*, vol. 38, pp. 8167–8178, 2013.

[30] C. Beyler, "Flammability limits of premixed and diffusion flames," in *SFPE Handbook of Fire Protection Engineering*. Springer New York, 2016, pp. 529–553.

[31] M. G. Zabetakis, "Flammability characteristics of combustible gases and vapors," U.S. Dept Of the Interior, Bureau of Mines, Technical report, 1965.

[32] J. Troitzsch, *International plastics flammability handbook: principles-regulations-testing and approval*. Hanser, 1983.

[33] A. R. Horrocks and D. Price, *Fire retardant materials*. Woodhead Publishing, 2001.

[34] D.-Y. Wang, *Novel Fire Retardant Polymers and Composite Materials*. Woodhead Publishing, 2016.

[35] R. E. Lyon and M. L. Janssens, "Polymer Flammability," Federal Aviation Administration, Technical Report DOT/FAA/AR-05/14, 2005.

[36] C. K. Law, *Combustion Physics*. Cambridge University Press, 2006.

[37] *Powerplant Installation and Propulsion System Compoent Fire Protection Test Methods, Standards, and Criteria*, U.S. Departement of Transportaion, Federal Aviation Administration Advisory Circular AC 20-135, Rev. Change 1, 2018.

[38] *Engine Fire Protection Document Information*, Federal Aviation Administration Std. AC 33.17-1A, 2009.

[39] *Test Method for Determining Material Ignition and Flame Spread Properties*, ASTM International Std. ASTM E1321, Rev. 18, 2018.

[40] *Test Method for Heat and Visible Smoke Release Rates for Materials and Products Using an Oxygen Consumption Calorimeter*, ASTM International Std. ASTM E1354, Rev. 17, 2022.

[41] *Test Methods for Measurement of Material Flammability Using a Fire Propagation Apparatus (FPA)*, ASTM International Std. ASTM E2058, Rev. 19, 2019.

[42] *Fire safety – Vocabulary*, International Organization for Standardization Std. ISO 13 943, 2017.

[43] H. Portz, *Brand-und Explosionsschutz von AZ*. Vieweg+Teubner Verlag, 2005.

[44] *Code of Federal Regulations, Title 14, Aeronautics and Space, Chapter1*, Federal Aviation Administration Std. Part 21 - Certification Procedures for Products and Parts, § 21.41, 2009.

[45] *Aircraft Materials Fire Test Handbook*, Federal Aviation Administration Std., 2009. [Online]. Available: https://www.fire.tc.faa.gov/handbook

[46] E. P. Burke, "Standard fire test apparatus and procedure (for flexible hose assemblies). revision," DTIC Document, Technical report Power Plant Engineering Report No. 3A, revised, 1978.

[47] R. Bentley, *Handbook of Temperature Measurement Vol. 3: The Theory and Practice of Thermoelectric Thermometry*, ser. Handbook of Temperature Measurement. Springer Singapore, 1998.

[48] D. N. Priest, "How accurate are those thermocouples?" *Priest & Associates Consulting*, vol. 200, pp. 1–7, 2007.

[49] C. R. Shaddix, "Correcting thermocouple measurements for radiation loss: A critical review," in *Proceedings of the 33rd national heat transfer conference NHTC'99*, M. Jensen and M. D. Marzo, Eds. ASME, 1999.

[50] L. G. Blevins, "Behavior of bare and aspirated thermocouples in compartment fires," in *National Heat Transfer Conference, 33 rd Proceedings*, 1999, pp. 15–17.

[51] L. G. Blevins and W. M. Pitts, "Modeling of bare and aspirated thermocouples in compartment fires," *Fire safety journal*, vol. 33, pp. 239–259, 1999.

[52] W. E. Kaskan, "The dependence of flame temperature on mass burning velocity," *Symposium (International) on Combustion*, vol. 6, pp. 134–143, 1957.

[53] J. H. Kent, "A noncatalytic coating for platinum-rhodium thermocouples," *Combustion and Flame*, vol. 14, pp. 279–281, 1970.

[54] K. A. Burton, H. D. Ladouceur, and J. W. Fleming, "An improved noncatalytic coating for thermocouples," *Combustion Science and Technology*, vol. 81, pp. 141–145, 1992.

[55] J. M. Madson and E. A. Theby, "Sio2 coated thermocouples," *Combustion Science and Technology*, vol. 36, pp. 205–209, 1984.

[56] J. C. Jones, "Letter to the editor," *Applied Thermal Engineering*, vol. 31, p. 4139, 2011, SET 2010 Special Issue.

[57] J. C. Jones, *Suggestions towards improved reliability of thermocouple temperature measurement in combustion tests*. ASTM International, 2003.

[58] J. C. Jones, "On the use of metal sheathed thermocouples in a hot gas layer originating from a room fire," *Journal of Fire & Flammability*, vol. 13, pp. 257–260, 1995.

[59] S. Brohez, C. Delvosalle, and G. Marlair, "A two-thermocouples probe for radiation corrections of measured temperatures in compartment fires," *Fire Safety Journal*, vol. 39, pp. 399–411, 2004.

[60] S. Krishnan *et al.*, "An approach to thermocouple measurements that reduces uncertainties in high-temperature environments," *Energy and Fuels*, vol. 29, pp. 3446–3455, 2015.

[61] A. Tereshchenko *et al.*, "Perturbations of the flame structure due to a thermocouple. I. Experiment," *Combustion, Explosion, and Shock Waves*, vol. 47, pp. 403–413, 2011.

[62] M. Tagawa and Y. Ohta, "Two-thermocouple probe for fluctuating temperature measurement in combustion-rational estimation of mean and fluctuating time constants," *Combustion and flame*, vol. 109, pp. 549–560, 1997.

[63] C. Goux, *Guide de thermométrie*. Eyrolles, 1959.

[64] Y.-H. Kao, "Experimental investigation of NexGen and gas burner for FAA fire test," Master's Thesis, University of Cincinnati, 2012.

[65] M. Kelly, "Development of FAA Copper Tube Heat Flux Calorimeter and Parametric Study of Burner Calibration," Resonate Testing Ltd., Technical report, 2016.

[66] G. L. V. Moureau and S. D. N. Chauvet, "Modeling of Conjugate Heat Transfer in a Kerosene / Air Spray Flame used for Aeronautical Fire resistance tests," *Flow, Turbulence and Combustion*, pp. 579–602, 2018.

[67] C. T. Nelson and C. G. Kidd, "How the Schmidt-Boelter gage really works," in *Proceedings of the 41st international instrumentation symposium*. U.S. Department of Energy, 1995.

[68] T. Blanchat and C. Hanks, "Comparison of the high temperature heat flux sensor to traditional heat flux gages under high heat flux conditions." Sandia National Laboratories (SNL), Albuquerque, NM, and Livermore, CA (United States), Technical report SAND2012-10683, 2013.

[69] W. M. Pitts *et al.*, "Round robin study of total heat flux gauge calibration at fire laboratories," *Fire Safety Journal*, vol. 41, pp. 459–475, 2006.

[70] A. Gifford *et al.*, "Convection calibration of schmidt-boelter heat flux gauges in stagnation and shear air flow," *Journal of Heat Transfer*, vol. 132, pp. 1–9, 2010.

[71] C. Purpura *et al.*, "Gardon gauge heat flux sensor verification by new working facility," *Measurement*, vol. 134, pp. 245–252, 2019.

[72] J. E. Demaree, "Reevaluation of burner characteristics for fire resistance tests." DTIC Document, Technical report FAA-RD-76-213, 1977.

[73] R. I. Ochs, "Development of a Next-Generation Burner for Testing Thermal Acoustic Insulation Burnthrough Resistance," U.S. Department of Transportation Federal Aviation Administration, Atlantic City, New Jersey, USA, Technical report DOT/FAA/AR-TN09/23, 2009.

[74] Y.-H. Kao *et al.*, "Experimental study of the burner for FAA fire test: NexGen burner," *Fire and Materials*, vol. 41, no. 7, 2017.

[75] D. R. Ventriglio, "Fire safe materials for navy ships," *Naval Engineers Journal*, vol. 94, pp. 65–74, 1982.

[76] L. Schlapbach and A. Züttel, "Hydrogen-storage materials for mobile applications," *Nature*, vol. 414, pp. 353–358, 2001.

[77] E. ASTM, "Astm e906/e906m-21, standard test method for heat and visible smoke release rates for materials and products using a thermopile method," *ASTM International*, vol. 04.07, 2022.

[78] V. Babrauskas, "Development of the cone calorimeter—a bench-scale heat release rate apparatus based on oxygen consumption," *Fire and Materials*, vol. 8, no. 2, pp. 81–95, 1984.

[79] V. Babrauskas and R. D. Peacock, "Heat release rate: the single most important variable in fire hazard," *Fire safety journal*, vol. 18, pp. 255–272, 1992.

[80] S. Feih *et al.*, "Tensile strength modeling of glass fiber-polymer composites in fire," *Journal of composite materials*, vol. 41, pp. 2387–2410, 2007.

[81] A. G. Gibson *et al.*, "High temperature and fire behaviour of continuous glass fibre/polypropylene laminates," *Composites Part A: Applied Science and Manufacturing*, vol. 41, pp. 1219–1231, 2010.

[82] A. Anjang *et al.*, "Deterioration of the fire structural resistance of sandwich composite under tension due to water absorption," *Composites Part A: Applied Science and Manufacturing*, vol. 87, pp. 263–270, 2016.

[83] A. Anjang *et al.*, "Tension modelling and testing of sandwich composites in fire," *Composite Structures*, vol. 113, pp. 437–445, 2014.

[84] D. Hopkins and J. G. Quintiere, "Material fire properties and predictions for thermoplastics," *Fire Safety Journal*, vol. 26, pp. 241–268, 1996.

[85] Y. C. Wang, P. Wong, and V. Kodur, "An experimental study of the mechanical properties of fibre reinforced polymer (frp) and steel reinforcing bars at elevated temperatures," *Composite Structures*, vol. 80, pp. 131–140, 2007.

[86] S. Eibl, "Influence of carbon fibre orientation on reaction-to-fire properties of polymer matrix composites," *Fire and Materials*, vol. 36, pp. 309–324, 2012.

[87] E. Kandare *et al.*, "Thermo-mechanical responses of fiber-reinforced epoxy composites exposed to high temperature environments. Part I: experimental data acquisition," *Journal of composite materials*, vol. 44, pp. 3093–3114, 2010.

[88] S. Eibl, "Potential for the formation of respirable fibers in carbon fiber reinforced plastic materials after combustion," *Fire and Materials*, vol. 41, pp. 808–816, 2017.

[89] T. M. Vetter *et al.*, "Characterization of one-sided thermal damage of carbon fiber reinforced polymers by means of depth profiles," *Journal of Composite Materials*, vol. 54, pp. 3699–3713, 2020.

[90] J. B. Henderson, J. Wiebelt, and M. Tant, "A model for the thermal response of polymer composite materials with experimental verification," *Journal of composite materials*, vol. 19, pp. 579–595, 1985.

[91] A. P. Mouritz *et al.*, "Review of fire structural modelling of polymer composites," *Composites Part A: Applied Science and Manufacturing*, vol. 40, pp. 1800–1814, 2009.

[92] J. Davies and H. Wang, "A numerical and experimental heat transfer study of grp panels subject to standard cellulosic and hydrocarbon fire tests," in *7th International Fire Science and Engineering Conference*, 1996, pp. 123–132.

[93] J. M. Davies, Y. C. Wang, and P. M. Wong, "Polymer composites in fire," *Composites Part A: Applied Science and Manufacturing*, vol. 37, pp. 1131–1141, 2006.

[94] D. Halm *et al.*, "Composite pressure vessels for hydrogen storage in fire conditions: Fire tests and burst simulation," *International Journal of Hydrogen Energy*, vol. 42, pp. 20 056–20 070, 2017.

[95] V. Birman *et al.*, "Response of a sandwich panel subject to fire or elevated temperature on one of the surfaces," *Composites Part A: Applied Science and Manufacturing*, vol. 37, pp. 981–988, 2006.

[96] A. P. Mouritz and A. G. Gibson, *Fire properties of polymer composite materials*. Springer Science & Business Media, 2007, vol. 143.

[97] A. P. Mouritz and Z. Mathys, "Post-fire mechanical properties of glass-reinforced polyester composites," *Composites Science and Technology*, vol. 61, pp. 475–490, 2001.

[98] A. P. Mouritz, "Simple models for determining the mechanical properties of burnt frp composites," *Materials Science and Engineering: A*, vol. 359, pp. 237–246, 2003.

[99] A. P. Mouritz and A. G. Gibson, *Fire properties of polymer composite materials*. Springer Science & Business Media, 2007, vol. 143.

[100] P. Tranchard, "Modelling the behaviour of a carbon / epoxy composite submitted to fire," Ph.D. dissertation, Université de Lille-I sciences et technologies, 2015.

[101] T. Chazelle *et al.*, "Fire Response of a Carbon Epoxy Composite : Comparison of the Degradation Provided with Kerosene or Propane Flames," *Proceedings of the Ninth International Seminar on Fire and Explosion Hazards (ISFEH9)*, pp. 950–958, 2019.

[102] W. Tabaka *et al.*, "Bench-scale fire stability testing – assessment of protective systems on carbon fibre reinforced polymer composites," *Polymer Testing*, vol. 102, p. 107340, 2021.

[103] A. Benelfellah *et al.*, "Residual mechanical properties of a carbon/epoxy wound composite exposed to fire," *S06 Mécanique des composites*, 2015.

[104] Y. I. Dimitrienko, "Thermomechanical behaviour of composite materials and structures under high temperatures: 1. materials," *Composites Part A: Applied Science and Manufacturing*, vol. 28, pp. 453–461, 1997.

[105] Y. I. Dimitrienko, "Thermomechanical behaviour of composite materials and structures under high temperatures: 2. structures," *Composites Part A: Applied Science and Manufacturing*, vol. 28, pp. 463–471, 1997.

[106] S. Feih and A. P. Mouritz, "Tensile properties of carbon fibres and carbon fibre–polymer composites in fire," *Composites Part A: Applied Science and Manufacturing*, vol. 43, pp. 765–772, 2012.

[107] C. Ulven and U. Vaidya, "Post-fire low velocity impact response of marine grade sandwich composites," *Composites Part A: Applied Science and Manufacturing*, vol. 37, pp. 997–1004, 2006.

[108] Y. Bai and T. Keller, "Modeling of post-fire stiffness of e-glass fiber-reinforced polyester composites," *Composites Part A: applied science and manufacturing*, vol. 38, pp. 2142–2153, 2007.

[109] A. P. Mouritz and Z. Mathys, "Post-fire mechanical properties of marine polymer composites," *Composite Structures*, vol. 47, pp. 643–653, 1999.

[110] C. Gardiner, Z. Mathys, and A. P. Mouritz, "Tensile and compressive properties of frp composites with localised fire damage," *Applied Composite Materials*, vol. 9, pp. 353–367, 2002.

[111] A. P. Mouritz and C. Gardiner, "Post-fire properties of sandwich polymer composites," *Composites A*, vol. 33, pp. 609–20, 2002.

[112] A. G. Gibson *et al.*, "Modeling composite high temperature behavior and fire response under load," *Journal of Composite Materials*, vol. 46, pp. 2005–2022, 2012.

[113] D. Swanson and J. Wolfrum, "Time to failure modeling of carbon fiber reinforced polymer composites subject to simultaneous tension and one-sided heat flux," *Journal of Composite Materials*, vol. 52, 2018.

[114] C. Luo, J. Lua, and P. E. DesJardin, "Thermo-mechanical damage modeling of polymer matrix sandwich composites in fire," *Composites Part A: Applied Science and Manufacturing*, vol. 43, no. 5, pp. 814–821, 2012.

[115] S. Feih *et al.*, "Modeling compressive skin failure of sandwich composites in fire," *Journal of Sandwich Structures & Materials*, vol. 10, no. 3, pp. 217–245, 2008.

[116] S. Sánchez-Carballido *et al.*, "A quantitative infrared imaging system for in situ characterization of composite materials in fire tests," *Fire Technology*, vol. 53, pp. 1309–1331, 2017.

[117] J. Meléndez *et al.*, "Infrared thermography of solid surfaces in a fire," *Measurement Science and Technology*, vol. 21, p. 105504, 2010.

[118] E. Schuhler *et al.*, "Fire behaviour of composite materials using kerosene burner tests at small-scales," *Fire Safety Journal*, p. 103290, 2021.

[119] M. Béland *et al.*, "Scaling methodology of the faa burner for pre-qualification fire tests of aircraft engine panels," in *Turbo Expo: Power for Land, Sea, and Air*. American Society of Mechanical Engineers, 2019, paper GT2019-91937, pp. 1–11.

[120] A. Moutet, "Etudes de pyrométrie pratique," *Eyrolles, France*, 1959.

[121] E. Schuhler, "Dégradation des matériaux composites sous l'effet d'une flamme , application à la réaction aux feux des composites utilisés pour les transports et l'énergie ." PhD dissertation, Normandie Université, 2020.

[122] P. G. B. Seggewiss, "Experimentelle und numerische Untersuchung des Verhaltens kohlenstofffaserverstärkter Epoxidmatrix-Systeme unter einseitiger thermischer und gleichzeitiger mechanischer Belastung," PhD dissertation, Universität der Bundeswehr München, 2011.

[123] S. I. Stoliarov *et al.*, "Prediction of the burning rates of charring polymers," *Combustion and Flame*, vol. 157, no. 11, pp. 2024–2034, 2010.

[124] G. Neuer, "Emissivity measurements on graphite and composite materials in the visible and infrared spectral range," in *Proceedings of the 1992 International Conference on Quantitative InfraRed Thermography*. QIRT Council, 1992.

[125] G. Neuer and G. Jaroma-Weiland, "Spectral and total emissivity of high-temperature materials," *International Journal of Thermophysics*, vol. 19, pp. 917–929, 1998.

[126] D. Guilhem *et al.*, "Absolute surface temperature measurement of low and varying emissivity tungsten (w) plasma facing components," 28th IEEE/NPSS Symposium on Fusion Engineering (SOFE2019) 2019, unpublished.

[127] Z. Acem *et al.*, "Surface temperature of carbon composite samples during thermal degradation," *International Journal of Thermal Sciences*, vol. 112, pp. 427–438, 2017.

[128] S. Sánchez-Carballido *et al.*, "Experimental determination of the thermal parameters of carbon fiber-composite materials exposed to fire by infrared imaging pulse thermography," *International Journal of Thermophysics*, vol. 34, pp. 1606–1616, 2013.

[129] A. Adibekyan *et al.*, "Emissivity, reflectivity and transmissivity of semitransparent fibre reinforced plastic composites," *Thermographie-Kolloquium*, pp. 3–9, 2017.

[130] J. M. Jones, P. E. Mason, and A. Williams, "A compilation of data on the radiant emissivity of some materials at high temperatures," *Journal of the Energy Institute*, vol. 92, pp. 523–534, 2019.

[131] M. Vollmer and K.-P. Möllmann, *Infrared Thermal Imaging*, 2nd ed. Wiley-VCH Verlag GmbH & Co. KGaA, 2017.

[132] S. A. Reggeti, A. K. Agrawal, and J. A. Bittle, "Two-color pyrometry system to eliminate optical errors for spatially resolved measurements in flames," *Applied Optics*, vol. 58, p. 8905, 2019.

[133] L. Savino *et al.*, "Free emissivity temperature investigations by dual color applied physics methodology in the mid- and long-infrared ranges," *International Journal of Thermal Sciences*, vol. 117, pp. 328–341, 2017.

[134] U. Wickström, "Heat transfer by radiation and convection in fire testing," *Fire and Materials*, vol. 28, pp. 411–415, 2004.

[135] T. Vega, B. Y. Lattimer, and T. E. Diller, "Fire thermal boundary condition measurement using a hybrid heat flux gage," *Fire Safety Journal*, vol. 61, pp. 127–137, 2013.

[136] H. Ingason and U. Wickström, "Measuring incident radiant heat flux using the plate thermometer," *Fire Safety Journal*, vol. 42, no. 2, pp. 161–166, 2007.

[137] S. Feih *et al.*, "Modelling the tension and compression strengths of polymer laminates in fire," *Composites Science and Technology*, vol. 67, pp. 551–564, 2007.

[138] R. Viskanta, "Heat transfer to impinging isothermal gas and flame jets," *Experimental thermal and fluid science*, vol. 6, pp. 111–134, 1993.

[139] C. E. Baukal and B. Gebhart, "Surface condition effects on flame impingement heat transfer," *Experimental thermal and fluid science*, vol. 15, pp. 323–335, 1997.

[140] S. Chander and A. Ray, "Flame impingement heat transfer: a review," *Energy Conversion and Management*, vol. 46, pp. 2803–2837, 2005.

[141] C. Baukal and B. Gebhart, "A review of flame impingement heat transfer studies part 2: Measurements," *Combustion science and technology*, vol. 104, pp. 359–385, 1995.

[142] Y.-H. Kao *et al.*, "Experimental study of the burner for FAA fire test: NexGen burner," *Fire and Materials*, vol. 41, pp. 898–907, 2017.

[143] C. A. Griffis *et al.*, "Degradation in Strength of Laminated Composites Subjected to Intense Heating and Mechanical Loading," *Journal of Composite Materials*, vol. 20, pp. 216–235, 1986.

[144] S. J. Ritchie *et al.*, "The effect of sample size on the heat release rate of charring materials," *Fire Safety Science*, vol. 5, pp. 177–188, 1997.

[145] B. Girardin *et al.*, "Fire tests at reduced scale as powerful tool to fasten the development of flame-retarded material: Application to cables," *Journal of Fire Sciences*, vol. 34, pp. 240–264, 2016.

[146] M. Béland, "Study and Design of a Small Kerosene Burner," Master's Thesis, Université Laval, 2018.

[147] P. C. Gómez *et al.*, "Evaluation of the fire resistance of protected carbon/epoxy laminates in small-scale experiments," *AIAA Scitech 2019 Forum*, pp. 1–12, 2019.

[148] C. A. Schneider, W. S. Rasband, and K. W. Eliceiri, "NIH Image to ImageJ: 25 years of image analysis," *Nature methods*, vol. 9, pp. 671–675, 2012.

[149] C. S. Lam and E. J. Weckman, "Steady-state heat flux measurements in radiative and mixed radiative-convective environments," *Fire and Materials*, vol. 33, pp. 303–321, 2009.

[150] Y. Ng, J. Tomblin, and E. Lian, "Medium temperature, out-of-autoclave, oven-vacuum-bag cure expoxy resin impregnated fiber reinforced composite materials, type 36, class 2, grade 193, style 3k-70-pw," National Center for Advanced Materials Performance, Wichita State University, Technical Report NMS 451/13 Rev. B, 2017.

[151] *Carlin "CRD" oil burners. Totally new in design and performance.*, Model 200 CRD and Model 201 CRD, The Carlin Company, Wethersfield, Conn. 06109, 1990, form No. 202.

[152] A. L. Brundage *et al.*, "Thermocouple response in fires, part 1: Considerations in flame temperature measurements by a thermocouple," *Journal of Fire Sciences*, vol. 29, pp. 195–211, 2011.

[153] I. L. Roberts, J. E. R. Coney, and B. M. Gibbs, "Estimation of radiation losses from sheathed thermocouples," *Applied Thermal Engineering*, vol. 31, pp. 2262–2270, 2011.

[154] V. Hindasageri, R. P. Vedula, and S. V. Prabhu, "Thermocouple error correction for measuring the flame temperature with determination of emissivity and heat transfer coefficient," *Review of Scientific Instruments*, vol. 84, 2013.

[155] R. A. Talib *et al.*, "Detailed investigation of heat flux measurements made in a standard propane-air fire-certification burner compared to levels derived from a low-temperature analog burner," *Journal of Engineering for Gas Turbines and Power*, vol. 127, pp. 249–256, 2005.

[156] A. Neely and P. Ireland, "Pilot study to investigate novel experimental and theoretical fire-event modelling techniques," in *37th Aerospace Sciences Meeting and Exhibit*. American Institute of Aeronautics and Astronautics, 1999.

[157] S. B. Tambe *et al.*, "Development of NexGen Burner Operations Setting for Fire Testing of Power Plant Components," FAA William J. Hughes Technical Center Aviation Research Division, Technical report DOT/FAA/TC-18/16, 2018.

[158] R. I. Ochs, "Development of a Next-Generation Burner for Testing Thermal Acoustic Insulation Burnthrough Resistance," Federal Aviation Administration, Technical report DOT/FAA/AR-TN09/23, 2009.

[159] M. M. Awad, *Fouling of Heat Transfer Surfaces*. InTech, 2011, vol. 1, ch. Heat Transfer - Theoretical Analysis, Experimental Investigations and Industrial Systems, pp. 505–542.

[160] J. G. Knudsen, *Power Condenser Heat Transfer Technology*. New York: Hemisphere Publishing, 1981, ch. Fouling of heat transfer surfaces, pp. 57–82.

[161] W. Y. Chang *et al.*, "Candle soot nanoparticles-polydimethylsiloxane composites for laser ultrasound transducers," *Applied Physics Letters*, vol. 107, pp. 1–5, 2015.

[162] J. R. Welker and C. M. Sliepcevich, "Heat transfer by direct flame contact in fire tests - phase 1," University Engineers, Inc., Technical report UE-122-FR, 1971.

[163] T. J. Fortin and A. Laesecke, "Viscosity measurements of aviation turbine fuels," *Energy and Fuels*, vol. 29, pp. 5495–5506, 2015.

[164] R. I. Ochs *et al.*, "The uncertainty of temperature and heat flux calibration for faa fire test background and scope of presentation," in *7th International Fire & Cabin Safety Research Technical Conference*, 2013, pp. 1–23.

[165] C. E. Baukal and B. Gebhart, "A review of empirical flame impingement heat transfer correlations," *International Journal of Heat and Fluid Flow*, vol. 17, p. 386–396, 1996.

[166] C. E. Baukal and B. Gebhart, "A review of flame impingement heat transfer studies part 1: Experimental conditions," *Combustion Science and Technology*, vol. 104, p. 339–357, 1995.

[167] G. Walter *et al.*, "Flame-object heat transfer using different burner types and orientations," *TMS Light Metals*, p. 741–746, 2006.

[168] N. Bal and G. Rein, "Relevant model complexity for non-charring polymer pyrolysis," *Fire Safety Journal*, vol. 61, p. 36–44, 2013.

[169] M. Försth and A. Roos, "Absorptivity and its dependence on heat source temperature and degree of thermal breakdown," *Fire and Materials*, vol. 35, p. 285–301, 2011.

[170] J. R. Hallman, J. R. Welker, and C. M. Sliepcevich, "Polymer surface reflectance-absorptance characteristics," *Polymer Engineering & Science*, vol. 14, no. 10, p. 717–723, 1974.

[171] J. D. Hood, "A method for the determination of the radiative properties of flames," PhD dissertation, The University of Oklahoma, 1966.

[172] P. Boulet *et al.*, "On the influence of the sample absorptivity when studying the thermal degradation of materials," *Materials*, vol. 8, pp. 5398–5413, 2015.

[173] K. Shannon and B. Butler, "A review of error associated with thermocouple temperature measurement in fire environments," *International Wildland Fire Ecology*, p. 7–9, 2003.

[174] S. Sánchez-Carballido *et al.*, "Measurement of the thermal parameters of composite materials during fire tests with quantitative infrared imaging," *Fire Technology*, vol. 54, p. 313–333, 2018.

[175] C. M. Rippe and B. Y. Lattimer, "Full-field surface heat flux measurement using non-intrusive infrared thermography," *Fire Safety Journal*, vol. 78, p. 238–250, 2015.

[176] E. D. Bearinger *et al.*, "Localized heat transfer from firebrands to surfaces," *Fire Safety Journal*, no. January, p. 103037, 2020.

[177] P. M. Reynolds, "A review of multicolour pyrometry for temperatures below 1500°c," *British Journal of Applied Physics*, vol. 15, no. 5, p. 579–589, 1964.

[178] J. Li, J. Gong, and S. I. Stoliarov, "Gasification experiments for pyrolysis model parameterization and validation," *International Journal of Heat and Mass Transfer*, p. 738–744, 2014.

[179] H. Zhao and N. Ladommatos, "Effects of temperature on the spectral emissivity of c/sic composites," *Progress in Energy and Combustion Science*, vol. 60, p. 221–255, 1998.

[180] T. Yu *et al.*, "4D temperature measurements using tomographic two-color pyrometry," *Optics Express*, vol. 29, p. 5304, 2021.

[181] A. Arakawa, K. Saito, and W. Gruver, "Automated infrared imaging temperature measurement with application to upward flame spread studies. part I," *Combustion and Flame*, vol. 92, pp. 222–IN2, 1993.

[182] Q. N. Chan *et al.*, "Color-ratio pyrometry methods for flame–wall impingement study," *Journal of the Energy Institute*, vol. 92, no. 6, p. 1968–1976, 2019.

[183] S. S. Aphale and P. E. DesJardin, "Development of a non-intrusive radiative heat flux measurement for upward flame spread using DSLR camera based two-color pyrometry," *Combustion and Flame*, vol. 210, p. 262–278, 2019.

[184] G. B. Hunter, C. D. Allemand, and T. W. Eagar, "Prototype device for multiwavelength pyrometry," *Optical Engineering*, vol. 25, 1986.

[185] B. Hunter, Gordon, C. D. Allemand, and T. W. Eagar, "An improved method of multiwavelength pyrometry," *SPIE Thermosense VII*, vol. 520, 1984.

[186] T. Inagaki, Y. Okamoto, and Z. Fan, "Temperature measurement and accuracy of bi—colored radiometer applying pseudo gray-body approximation," in *Proceedings Volume 2245, Thermosense XVI: An International Conference on Thermal Sensing and Imaging Diagnostic Applications*, J. R. Snell, Jr., Ed., vol. 2245, 1994, p. 274–285.

[187] A. Hörold *et al.*, "Structural integrity in fire: An intermediate-scale approach," *ECCM 2012 - Composites at Venice, Proceedings of the 15th European Conference on Composite Materials*, p. 24–28, 2012.

[188] A. Hijazi *et al.*, "A calibrated dual-wavelength infrared thermometry approach with non-greybody compensation for machining temperature measurements," *Measurement Science and Technology*, vol. 22, 2011.

[189] H. J. Jo *et al.*, "Spectral emissivity of oxidized and roughened metal surfaces," *International Journal of Heat and Mass Transfer*, vol. 115, pp. 1065–1071, 2017.

[190] J. Ballester and T. García-Armingol, "Diagnostic techniques for the monitoring and control of practical flames," *Progress in Energy and Combustion Science*, vol. 36, pp. 375–411, 2010.

[191] P. Saunders, "On the effects of temperature dependence of spectral emissivity in industrial radiation thermometry," *High Temperatures - High Pressures*, vol. 33, p. 599–610, 2001.

[192] J. M. Jones, P. E. Mason, and A. Williams, "A compilation of data on the radiant emissivity of some materials at high temperatures," *Journal of the Energy Institute*, vol. 92, p. 523–534, 2019.

[193] X. Li and W. Strieder, "Emissivity of high-temperature fiber composites," *Industrial and Engineering Chemistry Research*, vol. 48, no. 4, p. 2236–2244, 2009.

[194] N. Athanasopoulos *et al.*, "Numerical investigation and experimental verification of the joule heating effect of polyacrylonitrile-based carbon fiber tows under high vacuum conditions," *Journal of Composite Materials*, vol. 46, p. 2153–2165, 2012.

[195] E. Kim and N. Dembsey, "Parameter estimation for comprehensive pyrolysis modeling: Guidance and critical observations," *Fire Technology*, vol. 51, no. 2, 2015.

[196] U. Berardi and N. Dembsey, "Thermal and fire characteristics of frp composites for architectural applications," *Polymers*, vol. 7, no. 11, p. 2276–2289, 2015.

[197] F. Kreith *et al.*, "Heat and mass transfer," *The CRC Handbook of Mechanical Engineering, Second Edition*, pp. 4–1–4–357, 2004.

[198] A. J. Gordon *et al.*, "Hemispherical total emissivity of Hastelloy N with different surface conditions," *Journal of Nuclear Materials*, vol. 426, pp. 85–95, 2012.

[199] U. R. Evans, "The colours due to thin films on metals," *Proceedings of the Royal Society of London. Series A, Containing Papers of a Mathematical and Physical Character*, vol. 107, pp. 228–237, 1925.

[200] R. L. Higginson *et al.*, "Effect of thermally grown oxides on colour development of stainless steel," *Materials at High Temperatures*, vol. 32, pp. 113–117, 2015.

[201] B. Roebuck, G. Edwards, and M. G. Gee, "Characterisation of oxidising metal surfaces with a two colour pyrometer," *Materials Science and Technology*, vol. 21, pp. 831–840, 2013.

[202] S.-O. Gnessougou, A. Huot, and M. Larivière-Bastien, "Temperature Calculation of Non-Burning & Burning Materials Exposed to a Flame Using a Multispectral Infrared Camera," in *11th U. S. National Combustion Meeting Organized by the Western States Section of the Combustion Institute, Pasadena, California*, 2019, pp. 1–8.

[203] V. A. Petrov and V. Y. Reznik, "Measurement of the emissivity of quartz glass," *High Temperatures - High Pressures*, vol. 4, p. 687–693, 1972.

[204] B. T. Barnes, W. E. Forsythe, and E. Q. Adams, "The total emissivity of various materials at 100–500°C," *Journal of the Optical Society of America*, vol. 37, p. 804, 1947.

[205] V. Giurgiutiu, "Introduction," in *Structural Health Monitoring of Aerospace Composites*. Elsevier, 2016, pp. 1–23.

[206] "Boeing 787 dreamliner program fact sheet," https://www.boeing.com/commercial/787/, 2016, accessed: 2022-01-30.

[207] G. Hellard, "Composites in Airbus. a long story of innovations and experiences," https://www.airbusgroup.com/dam/assets/airbusgroup/int/en/investor-relations/documents/2008/presentations/GIF2008/gif2008_workshop_composites_hellard.pdf, 2008, accessed: 2022-01-30.

[208] S. Bourbigot *et al.*, "Latest developments in scale reduction for fire testing," in *27th BCC Conference (Flame 2017) - Recent Advances in Flame Retardancy of Polymeric Materials*, 2017, pp. 1–12.

[209] N. Grange *et al.*, "Numerical investigation of the heat transfer in an aeronautical composite material under fire stress," *Fire safety journal*, vol. 80, pp. 56–63, 2016.

[210] J. Bartlett and C. Stratford, "Fire resistance certification of aircraft composite materials," *Journal of Failure Analysis and Prevention*, vol. 1, pp. 37–43, 2001.

[211] T. T. Kim, "Thermo-mechanical characterization of silicon carbide-silicon carbide composites at elevated temperatures using a unique combustion facility," PhD dissertation, Air Force Institute of Technology, 2009.

[212] H. T. Akshatha, A. Rinku, and R. Gopalakrishnan, "Design, development and validation of fire protection scheme for the engine firewalls and cowling of a typical light transport aircraft," *ARPN Journal of Engineering and Applied Sciences*, vol. 9, no. 4, pp. 415–418, 2014.

[213] A. Gibson *et al.*, "Modeling composite high temperature behavior and fire response under load," *Journal of composite materials*, vol. 46, pp. 2005–2022, 2012.

[214] P. Tranchard *et al.*, "Fire behaviour of carbon fibre epoxy composite for aircraft: Novel test bench and experimental study," *Journal of Fire Sciences*, vol. 33, pp. 247–266, 2015.

[215] T. Marker, "A comparison of propane and kerosene burners for cargo compartment burnthrough testing ," Federal Aviation Administration, Technical report DOT/FAA/CT-TN87/45, 1987.

[216] L. Boulet *et al.*, *Modeling of convective and conductive conjugate heat transfer in a kerosene/air spray flame used for aeronautical fire resistance tests*. Springer International Publishing, 2019, vol. 25.

[217] N. Grange *et al.*, "Fire resistance of carbon-based composite materials under both ideal and realistic normative configurations," *Applied Thermal Engineering*, vol. 159, p. 113834, 2019.

[218] B. Vieille *et al.*, "Influence of kerosene flame on fire-behaviour and mechanical properties of hybrid carbon glass fibers reinforced peek composite laminates," *Composite Structures*, vol. 279, p. 114786, 2022.

[219] P. Chávez-Gómez *et al.*, "Carbon fiber oxidation in combustion environments—effect of flame chemistry and load on bundle failure," *Materials Today Communications*, vol. 31, p. 103560, 2022.

[220] J. Langot *et al.*, "Multi-physics modeling of the ignition of polymer matrix composites exposed to fire," *Fire Safety Journal*, vol. 122, p. 103312, 2021.

[221] F. Samyn *et al.*, "Preparation and flame retardancy of flax fabric/polybenzoxazine laminates," *Fire and Materials*, vol. 45, pp. 366–378, 2021.

[222] L. Durdina, J. Jedelsky, and M. Jicha, "Spray structure of a pressure-swirl atomizer for combustion applications," *EPJ Web of Conferences*, vol. 25, p. 01010, 2012.

[223] T. Pelzmann *et al.*, "Surface temperature and emissivity measurement for materials exposed to a flame through two-color IR-thermography," 2022, submitted for publication.

[224] *Standard Test Method for Tensile Properties of Polymer Matrix Composite Materials*, ASTM International Std. ASTM D3039/D3039M-08, 2014.

[225] S. Le Neve, "Fire tests on components used in fire zones. (AC 20-135 / ISO 2685). Fire Behaviour of structural composite materials," in *6th International aircraft fire and cabin safety research conference*, 2010.

[226] S. Chander and A. Ray, "Influence of Burner Geometry on Heat Transfer Characteristics of Methane / Air Flame Impinging on Flat Surface," *Experimental Heat Transfer*, vol. 19, no. 1, pp. 15–38, 2006.

[227] P. Chávez-Gómez *et al.*, "Carbon fiber damage evolution under flame attack and the role of impurities," 2022, submitted for publication.